Lattice Clock Experiments with Interacting Fermionic Quantum Gases

Dissertation

zur Erlangung des Doktorgrades

an der Fakultät für Mathematik, Informatik und
Naturwissenschaften

im Fachbereich Physik

der Universität Hamburg

vorgelegt von

Koen Cornelis Sponselee

Hamburg
2021

Gutachter der Dissertation:	Prof. Dr. Klaus Sengstock
	Prof. Dr. Henning Moritz
Gutachter der Disputation:	Prof. Dr. Klaus Sengstock
	Prof. Dr. Henning Moritz
	Prof. Dr. Peter Schmelcher
	Prof. Dr. Ludwig Mathey
	Prof. Dr. Markus Drescher
Vorsitzende/r der Prüfungskommission:	Prof. Dr. Peter Schmelcher
Datum der Disputation:	22.06.2021
Vorsitzender Fach-Promotionsausschusses PHYSIK:	Prof. Dr. Wolfgang Hansen
Leiter des Fachbereichs PHYSIK:	
	Prof. Dr. Günter H. W. Sigl
Dekan der Fakultät MIN:	
	Prof. Dr. Heinrich Graener

Abstract

Since the first creation of bosonic and fermionic quantum gases in the nineties, the field of ultracold atoms has expanded rapidly. Alkaline-earth(-like) atoms have been established as potent platforms for high-precision metrology and quantum simulations of strongly-interacting many-body physics. Due to their helium-like level structure, they feature a doubly-forbidden $^1S_0 \rightarrow {}^3P_0$ transition, making them ideal for high-precision clock applications with current relative uncertainties reaching about 10^{-18}. The ultra-narrow clock transition further enables measuring atomic interactions directly, and control of the clock state is expected to pave the way for the quantum simulation of many-body models with orbital degrees of freedom such as the Kondo lattice model and the Kugel-Khomskii model, going beyond the paradigm of the much-studied Bose- and Fermi-Hubbard models. Furthermore, the SU($\mathcal{N}$) symmetry of the ground and excited clock state, caused by the decoupling of the nuclear from the electronic spin, has enabled studying many exotic phenomena such as SU($\mathcal{N}$) quantum magnetism and Pomeranchuk cooling in SU($\mathcal{N}$) Mott insulators. Additionally, ytterbium, the element used in this work, has seven stable isotopes, of which two are fermionic, enabling the study of a large variety of mixtures.

In this work, measurements with fermionic ytterbium in optical lattices are presented. The spin-exchanging interaction between the $^1S_0$ ground and $^3P_0$ excited state of ^{171}Yb was measured spectroscopically, paving the way for the quantum simulation of the anti-ferromagnetic Kondo lattice model. Furthermore, high-resolution spectroscopic measurements on interorbital SU(2)⊗SU(6)-symmetric Fermi-Fermi mixtures of $^{171}_{e/g}$Yb -$^{173}_{g/e}$Yb are described, which provide, among others, a benchmark for accurate ground-excited state Yb$_2$ molecular models and a possible platform to study two-flavour symmetry-locking phases. Lastly, measurements on the 1D dissipative Fermi-Hubbard model are presented, where the two- and six-spin mixtures of ^{173}Yb show a dynamic inhibition of two-body losses. We attribute this to the formation of a highly-entangled Dicke state, which is protected from further decay by the continuous quantum Zeno effect, and which has optimal metrological properties enabling beating the standard quantum limit and reaching Heisenberg-limited spectroscopy.

Zusammenfassung

Seit der ersten Realisierung von bosonischen und fermionischen Quantengasen, erlebte das Feld der ultrakalten Atome eine schnelle Entwicklung. Erdalkali(-ähnliche) Atome etablierten sich als nützliche Systeme für hochpräzise Metrologie und die Quantensimulation von stark wechselwirkenden Vielteilchensystemen. Aufgrund ihrer Helium-ähnlichen Energieniveaustruktur haben diese einen zweifach verbotenen $^1S_0 \to {}^3P_0$ Übergang, was sie ideal macht für hochpräzise Uhrenanwendungen mit relativen Ungenauigkeiten bis zu ungefähr 10^{-18}. Der ultraschmale Uhrenübergang ermöglicht zusätzlich das direkte Messen von atomaren Wechselwirkungen und die Kontrolle über den Uhrenzustand eröffnet neue Möglichkeiten für die Quantensimulation von Vielteilchenmodellen mit orbitalen Freiheitsgraden wie dem Kondo Gitter Modell und dem Kugel Kugel-Khomskii Model, welche über das Paradigma der intensiv erforschten Bose- und Fermi-Hubbard Modelle hinausgehen. Darüber hinaus besitzen der Grund- und angeregte Uhrenzustand aufgrund der Entkopplung des nuklearen und elektronischen Spins eine SU($\mathcal{N}$)-Symmetrie, was die Erforschung von vielen exotischen Phänomenen zur Folge hat, wie etwa dem SU($\mathcal{N}$)-Quantenmagnetismus und der Pomeranchuk-Kühlung in SU($\mathcal{N}$) Mott-Isolatoren. Zusätzlich besitzt Ytterbium, das Element welches in dieser Arbeit verwendet wird, sieben stabile Isotope, wovon zwei fermionisch und fünf bosonisch sind und daher die Forschung einer großen Anzahl an Mischungen ermöglicht.

In diesem Werk werden Messungen mit fermionischem Ytterbium in optischen Gittern präsentiert. Die Spin-Austauschwechselwirkungen zwischen dem $^1S_0$ Grund und $^3P_0$ angeregten Zustand von ^{171}Yb werden spektroskopisch gemessen, welche wichtig für die Quantensimulation des antiferromagnetischen Kondo Gitter Modells sind. Außerdem werden hoch-präzise Spektroskopie-Messungen an interorbitalen SU(2)⊗SU(6) symmetrischen Fermi-Fermi Mischungen beschrieben, die unter anderem als Grundlage für zukünftige Yb_2 Molekülmodelle dienen können und eine mögliche Plattform für die Erforschung von zwei-flavour Symmetrie-fixierten Phasen darstellen. Abschließend werden Messungen an dem 1D dissipativen Fermi-Hubbard Modells präsentiert, bei dem die zwei und sechs Spin-Mischungen von ^{173}Yb eine dynamische Unterdrückung der Zweikörperverluste erfahren. Wir schreiben dies der Entstehung

eines hoch verschränkten Dicke-Zustandes zu, welcher vor weiterem Zerfall durch den kontinuierlichen Quanten-Zeno-Effekt geschützt wird. Diese Dicke-Zustände haben optimale metrologische Eigenschaften, die es ermöglichen das Standard-Quantenlimit zu brechen und das Heisenberg-Limit zu erreichen.

Publikationen

Im Rahmen der vorliegenden Arbeit sind die folgende wissenschaftliche Veröffentlichungen entstanden.

Publications

The following research articles have been published in the course of this thesis.

[1] K. Sponselee, L. Freystatzky, B. Abeln, M. Diem, B. Hundt, A. Kochanke, T. Ponath, B. Santra, L. Mathey, K. Sengstock and C. Becker, "Dynamics of ultracold quantum gases in the dissipative Fermi-Hubbard model", *Quantum Science and Technology* 4.1 (2018), p. 014002.

[2] B. Abeln, K. Sponselee, M. Diem, N. Pintul, K. Sengstock, and C. Becker, "Interorbital interactions in an SU(2)⊗SU(6)-symmetric Fermi-Fermi mixture", *Phys. Rev. A* 103 (2021), p. 033315.

Contents

List of Figures

List of Tables

Chapter 1

Introduction

After the first creation of Bose-Einstein condensates [3, 4] in 1995, and degenerate Fermi gases in 1999 [5], the field of ultracold quantum gases has grown steadily. Though the first quantum gas experiments were performed with rubidium, sodium and potassium atoms, quantum degeneracy has now been reached using several other alkali and alkaline-earth(-like) atoms, molecules, photons and other systems.

One of the main interests within the quantum gas community is the pursuit of quantum simulators. The idea, coined in 1981 by R.P. Feynman [6], is a way of countering the limitations classical computers have when calculating quantum behaviour. To this end, well-controlled quantum systems which obey model Hamiltonians are studied. Though quantum simulators have been realised using various systems, this thesis focusses on ultracold atoms, which exhibit a large degree of control and tunability. Of particular interest are quantum-degenerate atoms to study many-body physics [7] or atoms in optical lattices [8], where, among others, the Bose- and Fermi-Hubbard models [9–12] have been studied extensively.

The atom of our interest, the alkaline-earth-like atom ytterbium, has seven stable isotopes, five of which are bosonic and two of which are fermionic, and it was first cooled to quantum degeneracy by the group of Y. Takahashi in 2003 [13]. Due to the two electrons in the outer shell, alkaline-earth(-like) atoms have a helium-like level structure, which gives rise to several interesting properties. One of these is the existence of the doubly-forbidden $^1S_0 \rightarrow\,^3P_0$ clock transition, which is used to make some of the most accurate clocks with relative uncertainties of about 10^{-18} [14–19]. The clock transition further enables the direct measurement of atomic interactions through high-resolution spectroscopy [20–23], and the utilisation of a second long-lived quasi-ground state with a natural lifetime of $1/\Gamma > 16\,s$ [24]. Atomic interactions are no-

toriously difficult to calculate accurately, especially for heavy atoms such as ytterbium, making direct spectroscopic measurement desirable. Mixtures of ground- and $^3P_0$ excited-state atoms, referred to as interorbital mixtures, are expected to enable quantum simulating the Kugel-Khomskii model [25, 26], and the interorbital Feshbach resonance is expected to allow for the observation of interorbital superfluidity [27–30]. However, one of the main interests in alkaline-earth(-like) atoms comes from the prospect of studying the Kondo lattice model [25, 31–34], especially the exotic 1D case which is not realised in condensed-matter systems [25, 31], or the 2D and 3D cases which are not yet well understood [32].

Due to the closed-shell structure of ytterbium, the electronic angular momentum J is zero for both the spin-singlet $^1S_0$ ground state and for the spin-triplet $^3P_0$ excited state, resulting in a decoupling from the nuclear spin I, which for bosons is $I = 0$ and for fermions is $I = 1/2$ ($I = 5/2$) for ^{171}Yb (^{173}Yb). This decoupling leads to SU($\mathcal{N}$) symmetry, where $\mathcal{N} = 2I + 1$ [25, 26], or specifically SU(2) and SU(6) symmetry for ^{171}Yb and ^{173}Yb [35, 36], respectively, and SU(10) symmetry of the alkaline-earth atom ^{87}Sr [37, 38]. These highly-symmetric systems have enabled studying SU($\mathcal{N}$) quantum magnetism in 1D [39], contact interactions in an SU($\mathcal{N}$)-symmetric Fermi gas [40, 41] and Pomeranchuk cooling in SU($\mathcal{N}$) Mott insulators [42–47]. Furthermore, the nuclear-spin degree of freedom has been utilised to study topology in synthetic dimensions [48], similar to realisations with the interorbital degree of freedom [49] and lattice momentum states [50, 51].

Mixtures of quantum gases have enabled studying a large variety of exotic systems, such as weakly-bound heteronuclear molecules [52], dipolar molecules [53–55] and polaronic quasiparticles [56–59], exotic superfluidity [60], interaction-induced insulating phases [45, 52, 61–64] and quantum magnetism [65–67]. Such mixtures have been implemented using, for instance, hyperfine-state mixtures [68–71], isotope mixtures [38, 72–75], element mixtures [52, 76–81] and orbital-state mixtures [20–22]. Because of its large number of stable isotopes, ytterbium is a promising candidate for studying various Bose-Bose [82, 83], Bose-Fermi [84, 85] and Fermi-Fermi mixtures [60]. With these many available mixtures, all exhibiting different s-wave interactions in the ground state [86, 87], ytterbium offers an ideal candidate to study the interplay of intra- and interisotope interactions which is expected to lead to exotic quantum phases [87]. Fermi-Fermi mixtures have been of particular interest, among others, due to their analogy with fermionic pairing [5, 79, 88–91]. Furthermore, Fermi-Fermi mixtures of ^{171}Yb and ^{173}Yb exhibit SU(2)⊗SU(6) symmetry [36, 92], which is expected to display d-wave superfluidity [93] and two-flavour superfluid symmetry-locking phases [94, 95] due to the competition of different interactions. In this work, we go beyond ground-ground state interactions [36] and directly measure elastic and inelastic s-wave interactions in excited-ground state pairs of ^{171}Yb -^{173}Yb mixtures, as treated in Ref. [2] and

Ch. 5.

In real-world quantum simulators, dissipation, or coupling to the environment, is typically one of the main obstacles. However, dissipation has also been proposed for state engineering [96–100], entropy transfer [101], and correlation measurements [102]. The high degree of tunability of quantum gases enables controlled studying of dissipation by coupling to an external bath [103, 104]. Various types of dissipation have been studied experimentally, such as one-body losses [105–109], two-body losses [110–113], losses of polar fermionic molecules [114, 115], tunable inelastic losses due to photo-association [116], and in synthetic lattices of momentum states [117]. A suppression of losses was seen in a BEC of ^{87}Rb, which was attributed to the continuous quantum Zeno effect [105]. Dissipation has also been subject to continued theoretical work [118–123]. We have performed measurements [1] on the SU(2)-symmetric dissipative Fermi-Hubbard model in 1D, where it was predicted that a highly-entangled Dicke state [124] forms dynamically due to spin-conserving two-body losses [99]. Dicke states exhibit optimal metrological properties, which allow for beating the standard quantum limit and reaching the Heisenberg limit, which can drastically improve the accuracy of atomic clocks [99]. It was further shown that the magnetic correlations in this system undergo a dynamical sign-reversal [118].

This work is structures as follows.

- Chapter 2 gives a brief summary of the relevant properties of ytterbium, and gives an overview of the various elements of the experimental apparatus used to cool atoms to quantum degeneracy.

- Chapter 3 treats quantum two-level systems in the context of clock excitation. Two typical measurements, Rabi oscillations and clock spectroscopy, are shown for single atoms localised in a deep optical lattice.

- Chapter 4 expands on these spectroscopic measurements by studying a lattice filled with a mixture of two spin states of ^{171}Yb. As explained there, the Pauli exclusion principle gives rise to an interorbital spin-exchanging interaction after excitation, and this interaction is measured.

- Chapter 5 presents studies on interacting Fermi-Fermi mixtures of ^{171}Yb and ^{173}Yb, and both the elastic and inelastic part of the interorbital scattering lengths are measured. Though the elastic interactions turn out to be small and attractive for both possible interorbital interactions, the inelastic interactions are different by several orders of magnitude. Furthermore, the SU(2)⊗SU(6) symmetry of the elastic interorbital interactions is directly observed, and the p-wave scattering lengths are estimated.

- Chapter 6 discusses measurements on the dissipative 1D Fermi-Hubbard model, where the intrinsic two-body losses of excited ytterbium atoms are studied. After a transient time, the two-body losses cease, which we attribute to the dynamical build-up of a highly-entangled Dicke state, as predicted for this system [99].

Chapter 2

Experimental Setup

Before treating the measurements done for this work, this chapter gives an overview of both the relevant properties of ytterbium, and the experimental setup. Though modifications have been made to parts of the setup, the largest part of the apparatus was built up before the beginning of this work. For a more detailed treatment of the different iterations and parts of the setup, see the previous publications [1, 2, 125] and theses [126–142]. For additional information on the current setup, see Refs. [143, 144].

The work in this chapter was supervised by K. Sengstock & C. Becker. The data presented in this chapter was taken by B. Abeln, M. Diem and the author. The analysis was done by the author.

2.1   Properties of Ytterbium

The alkaline-earth-like atom ytterbium (Yb) is a lanthanide atom with atom number 70 and seven stable isotopes. Five of these, ^{168}Yb, ^{170}Yb, ^{172}Yb, ^{174}Yb and ^{176}Yb are bosonic and have nuclear spin $I = 0$. The two fermionic isotopes ^{171}Yb and ^{173}Yb have $I = 1/2$ and $I = 5/2$ and natural abundancies 14.1% and 16.1% [145], respectively.

Due to the two electrons in the outer shell, ytterbium has a helium-like level structure, as depicted schematically in Fig. 2.1. Here the term symbol $^{2S+1}L_J$ denotes the angular momentum eigenvalues of the electrons, with the spin multiplicity $2S + 1$, the orbital angular momentum L and the total electronic angular momentum J, which is the eigenvalue of the total electronic angular momentum operator $\hat{\mathbf{J}} = \hat{\mathbf{S}} + \hat{\mathbf{L}}$. The states and transitions relevant for this work are shown in Fig. 2.1, with the spin-singlet states (total spin $S = 0$) on the left and the triplet states ($S = 1$) on the right.
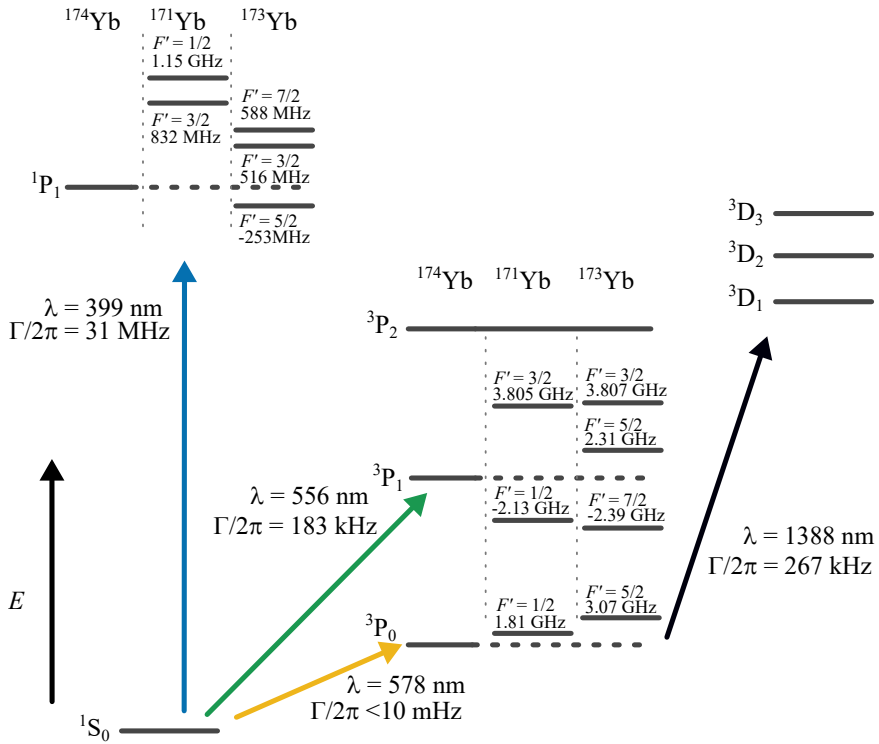
Figure 2.1: Energy level scheme of ytterbium (not to scale). The relevant transitions are shown as coloured arrows, with the wavelength λ and natural linewidth Γ. The horizontal grey lines indicate the energy levels of ^{174}Yb, ^{171}Yb ^{173}Yb (see text). The hyperfine F' manifold is denoted above or below the fermionic hyperfine states and the frequency denotes the detuning $\delta/2\pi$ with respect to the transition of ^{174}Yb. The literature values are taken from Refs. [24, 146–150], and the linewidth of the ^{3}P$_0$ → ^{3}D$_1$ transition was obtained by Refs. [129, 151].

Both the $^1S_0$ ground state and the long-lived $^3P_0$ excited clock state have $J = 0$, which leads to a decoupling of the total electronic spin and the nuclear spin I, such that the total atomic angular momentum $\hat{\mathbf{F}} = \hat{\mathbf{I}} + \hat{\mathbf{J}}$ is simply given by $F = I$, where F is the eigenvalue of the total atomic angular momentum operator $\hat{\mathbf{F}}$. For ^{171}Yb and ^{173}Yb, the total angular momenta of the ground and clock states are thus given by $F = I = 1/2$ and $F = I = 5/2$, respectively, and since the magnetic moment of the nucleus is about 2000 times smaller than that of an electron, these states are barely sensitive to magnetic fields. Crucially, for the ground and clock states the decoupling leads to SU($\mathcal{N} = 2I + 1$)-symmetric interactions, in other words, the interactions are invariant under rotation of angular momentum [25, 26, 152]. This symmetry is not exact, but is predicted to hold to a relative accuracy of $\Delta a_{gg}/a_{gg} \approx 10^{-9}$ for ground-ground-state interactions, and $\Delta a_{eg,ee}/a_{eg,ee} \approx 10^{-3}$ for excited-ground-state and excited-excited-state interactions [25], where $a_{o_1 o_2}$ is the s-wave scattering length of two atoms in orbitals o_1 and o_2. SU($\mathcal{N}$)-symmetric systems have been realised experimentally with ytterbium [21, 35, 36] and strontium* [20, 37, 38].

Figure 2.1 further shows the hyperfine splittings of the fermionic isotopes, caused by the different possible total angular momenta $F \in [|I - J|, \ldots, I + J]$ for states with $J \geq 1$. Since bosonic ytterbium has a nuclear spin of $I = 0$, the total atomic angular momentum is equal to the total electronic angular momentum J, and hence does not exhibit a hyperfine splitting. The fermionic hyperfine splittings† are denoted with respect to the energy of the boson ^{174}Yb which has the highest natural abundance.

One of the main research interests of ytterbium comes from the presence of a metastable excited state $^3P_0$, often simply referred to as the excited state, $|e\rangle$, or the clock state. It is connected to the ground state by a doubly-forbidden‡ ultranarrow transition, and thus has a natural lifetime of many seconds§, which is effectively stable for most measurements on the ms timescale. Therefore, exciting ground-state atoms to the $^3P_0$ state yields an additional degree of freedom, which is promising for the study of, among others, Kondo-like physics [25, 31–34], the Kugel-Khomskii model [25, 26] and synthetic topological systems [49]. Furthermore, the small natural linewidth makes it an excellent platform for so-called optical clock experiments [14–19], where a frequency-narrowed laser can perform spectroscopy on interacting systems. Since

---

* In the alkaline-earth atom ^{87}Sr, $\mathcal{N}$ can be as large as ten due to the nuclear spin of $I = 9/2$.

† The hyperfine splittings of the $^3P_2$ state and the ^3D states are omitted since these do not directly play a role in this work.

‡ That is, the transition is both electric and magnetic dipole forbidden. The transition is nonetheless possible due to a small admixing of the $^3P_1$ and $^1P_1$ state in the $^3P_0$ state [153].

§ Though it has not directly been measured, theoretical predictions have shown a natural linewidth of $\Gamma/2\pi < 10\,\text{mHz}$ [24]. Further note that the metastable $^3P_2$ state is similarly long-lived, though not utilised in this work.

Table 2.1: Summary of the elastic scattering lengths of $^1S_0$ ground and $^3P_0$ excited-state pairs of fermionic Yb. The interorbital spin-exchange interaction of ^{171}Yb and of the interorbital interisotope interactions of ^{171}Yb -^{173}Yb are measured in our work [2] and presented in Ch. 4 and 5. The interaction of $^{171}_e$Yb -$^{173}_e$Yb has not been measured yet. All values are in units of the Bohr radius $a_0 \approx 5.29 \times 10^{-11}$ m [156].

	$^{171}_g$Yb	$^{171}_e$Yb	$^{173}_g$Yb	$^{173}_e$Yb
$^{171}_g$Yb	$-3(4)$ [86]	$a_{eg^+} = 201(5)$ [2] $a_{eg^-} = 306(6)$	$-5.8(6) \times 10^2$ [86]	$-1.0(6) \times 10^2$ [2]
$^{171}_e$Yb		104(7) [155]	$-8(6) \times 10^1$ [2]	-
$^{173}_g$Yb			199(2) [86]	$a_{eg^+} = 1894(18)$ [21, 157] $a_{eg^-} = 220(2)$
$^{173}_e$Yb				306(11) [21]

interactions in ultracold systems are typically on the order of kHz, a narrow laser and transition are needed to measure these directly, for which the clock setup was built (see Sec. 2.5).

In the ultracold-temperature regime, only s-wave scattering plays a role, which, for $^1S_0$ ground and $^3P_0$ excited states of ytterbium, are described by a single scattering length a due to their SU($\mathcal{N}$) symmetry. Whereas in alkali atoms these interactions can be tuned by magnetic Feshbach resonances [154], these are not available due to the small total angular momentum of ytterbium. Though interorbital Feshbach resonances [27–30] exist at 1300 G for ^{171}Yb [155] and 55(8) G for ^{173}Yb [28], another opportunity the large number of abundant ytterbium isotopes offers is to study different pair interactions which naturally exhibit different scattering lengths. Table 2.1 gives an overview of all known s-wave scattering lengths of pairs of ground-state and excited-state fermionic ytterbium, which shows the availability of scattering lengths from large and attractive ($a < 0$) to large repulsive ($a > 0$). As explained in Ch. 4, intraisotope interorbital interactions are quantified by two scattering lengths $a_{eg^\pm}$ due to the Pauli exclusion principle. The intraisotope interorbital interactions of ^{171}Yb were measured by the Kyoto [23] ground, the Munich group [155], and in our group [2], which is explained in detail in Ch. 4. Additionally, we have measured the interisotope interorbital interactions in $^{171}_{e/g}$Yb -$^{173}_{g/e}$Yb mixtures [2], as treated at length in Ch. 5.

2.2 Atom Cooling

In our experiment, ytterbium is cooled down to quantum degeneracy in four steps. The experimental setup to achieve this is described in detail in previous publications [1, 2, 125] and theses [126–130, 132, 138, 143], here only a brief overview is given. The cooling relies on two principles, laser cooling in a magneto-optical trap (MOT) and evaporative cooling (see, for instance, Ref. [158]).

Figure 2.2 depicts the laser beam powers during a typical DFG-creation sequence. Gaseous atoms supplied by a dispenser are cooled down in the 2D MOT and transferred to the 3D MOT by gravity and the push beam ('MOT loading' in the figure), typically for about 18 s. The push beam is switched off and the 3D MOT is compressed (MC) in two steps of 200 ms by reducing the laser power and by shifting the laser frequency towards resonance. After switching off the blue and green MOTs, the atoms are held in the bi-colour crossed dipole traps consisting of a green 532 nm beam (see Sec. 2.2.3) and two crossed infrared 1064 nm beams (see Sec. 2.2.4). The green dipole trap is ramped down exponentially (GDT ramp) in 6 s and switched off. In experiments where a non-balanced spin preparation is required, optical pumping (OP) is performed (see Sec. 2.3). The IR beams (IR1 & IR2) are ramped down exponentially (IR ramp) in 3 s to cool the atoms down to quantum degeneracy. The final depths of the IR1 and IR2 beams can be tuned to vary the final atom number and temperature. The IR beams are switched off and after a time-of-flight (ToF), typically of 16 ms, the atoms are imaged ('im' and 'ref', see Sec. 2.6). In this way, degenerate Fermi gases are created and observed.

2.2.1 The 2D Magneto-Optical Trap

Gaseous Yb emitted by the dispenser is trapped in a 2D-MOT setup in the horizontal x-z plane, which runs at the $^1S_0 \rightarrow ^1P_1$ transition at wavelength $\lambda = 399$ nm. This reduces the motion of the atoms in that plane, and a push beam in the direction of gravity, defined as the y-direction, is used to optimise the atom transfer into the 3D MOT. The initial setup has been treated in detail in Refs. [125–129, 132], though the majority of the setup was rebuilt by B. Santra, B. Abeln and the author, and is described in the following.

Figure 2.3 shows a schematic of the 2D-MOT setup, consisting of the so-called laser board (left) and the upside-down experimental board (right)*. A commercial tapered-amplified diode laser with frequency doubling in a second-harmonic-generation

---

* Note that the optical elements on the experiment board are mounted upside-down, such that in reality this top-view direction cannot been seen. Hence, when looking from below, the scheme is mirrored top to bottom.
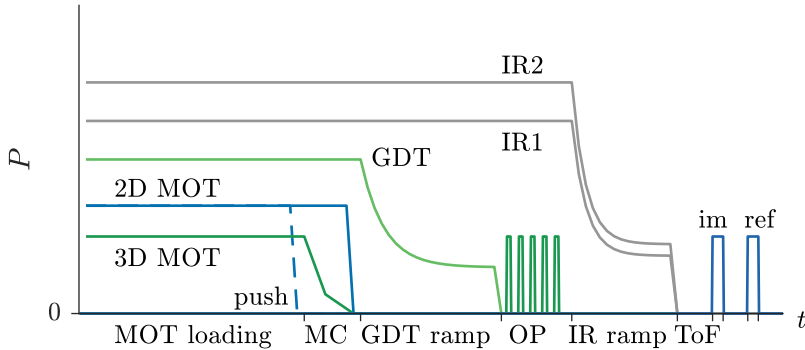
Figure 2.2: Schematic of a DFG creation sequence (not to scale), showing the laser beam powers P as a function of time t. The solid blue lines show the 2D MOT and imaging laser beams, the dashed blue lines shows the push beam, the dark green lines indicate the 3D MOT and optical pumping (OP) beams, the light green shows the green dipole trap (GDT) beam, and the grey lines show the infrared dipole trap beams (IR1 & IR2). The different time steps are indicated below the x-axis (see text).

(SHG) cavity is used* to create an approximately 1.5 W-power beam at a wavelength of 399 nm. Due to the higher laser power, the 2D-MOT loading rate is saturated and is therefore insensitive to small fluctuations in the laser output power. Using two mirrors, depicted by the blue-grey rectangles with a black back, the laser beam is aimed at a half-wave plate ($\lambda/2$) and is split by a polarising beamsplitter (PBS). The deflected beam passes through another $\lambda/2$ plate and PBS to further reduce the beam power, the remainder of which is deposited onto a beam dump (BD). About 2 mW of power remains and passes through a 50/50 beamsplitter (BS), which overlaps the beam with the so-called offset-lock laser beam from the imaging laser setup (see Sec. 2.6 and Ref. [143]). This offset-lock beam is coupled out of a fibre (upper left), polarisation-cleaned by a PBS and its beam size is changed by a telescope. The two overlapped beams are focussed on a photodiode (PD) by a lens to make the signal less sensitive to small misalignments. The offset-lock beam polarisation is set by variable stress loops on the fibre to optimise the signal on the PD. Using the photodiode, the 2D-MOT laser is locked to the imaging laser frequency with a variable frequency offset, which is called the offset lock. The offset frequency can be changed in-cycle to different isotopic resonances (see Sec. 2.2.5).

---

*Toptica TA SHG Pro.
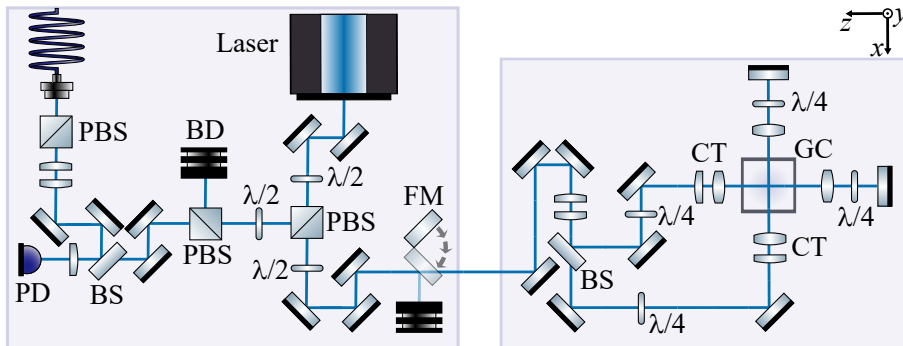
Figure 2.3: Top view schematic of the 2D-MOT setup (not to scale), with (left) the laser board and (right) the upside-down experiment board (see text). The coordinate system is shown in the upper right corner. [159]

The beam emitted by the first PBS is the main 2D-MOT beam, and passes through another $\lambda/2$ plate and is transferred to the experimental board. A flip mirror (FM) is switched to deflect the 2D-MOT beam onto a beam dump to prevent resonant stray light from the laser board reaching the atoms in following cooling stages[*]. The 2D-MOT beam passes through a telescope which increases the beam size to about 50 mm. This beam is split in a 50/50 beamsplitter, and both beams pass through a quarter-waveplate ($\lambda/4$) to create circularly-polarised light. The two beams pass through a cylindrical telescope[†] and fall onto the 2D-MOT glass cell (GC) approximately perpendicularly. Both beams pass through a lens which focusses the beam on a retro-reflecting mirror, forming a so-called *cat's eye* setup. A $\lambda/4$ waveplate is placed between the lens and mirror to ensure the retro-reflected beam polarisation is rotated correctly. Razor blades in front of the cylindrical telescope and in the cat's eye setup ensure that the counter-propagating beams are perfectly overlapped.

Using this setup, atoms are trapped in the 2D MOT and transferred continuously to the 3D MOT by gravity and the push beam. For further information, see Refs. [125–130].

---

[*] For the same reason the laser board and experiment board are both shielded by blackened aluminium. The laser board further has a lid and the beam between the boards passes through a pipe, both made out of blackened aluminium.

[†] The cylindrical telescope and the retro-reflecting mirrors were part of the original setup, for details see Refs. [125–129, 132].

2.2.2   The 3D Magneto-Optical Trap

The working principle of the 3D MOT is the same as for the 2D MOT, except in all three spatial dimensions, hence trapping the atoms in an approximately spherical cloud. It is set to the $^1S_0 \rightarrow \,^3P_1$ intercombination transition at $\lambda = 556$ nm, which with its narrow natural linewidth $\Gamma = 183$ kHz [146] allows for laser cooling to low temperatures. Various versions of the setup have been explained in detail in Refs. [125–130, 138], but for the most recent version see Ref. [143]. Here only a brief overview is given.

Similar to the 2D-MOT laser, a commercial tapered-amplified diode laser with frequency doubling in a SHG cavity is used[*] to create an approximately 250 mW-power beam at a wavelength of 556 nm. The laser beam is split into several beams. First, a part of the beam is split off and used to lock the laser to a high-finesse ultra-low-expansion (ULE) cavity using a Pound-Drever-Hall (PDH) method [143, 160]. The frequency stability of the cavity was observed over a few months, as shown in Fig. 2.4, where the detuning δ is shown with respect to the resonance on the first day. The drifts seem to be non-linear, and hence the resonance frequency is checked and optimised on a daily basis. Second, a part of the laser beam is split off to create an Optical-Stern-Gerlach (OSG) beam [161] (see Sec. 2.3.2) which is shifted by two double-pass 200 MHz acousto-optical modulators (AOMs) and one single-pass 200 MHz AOM. Third, a part of the beam is used to create the ^{173}Yb 3D-MOT light, which is transferred to the so-called *3D-MOT cluster* [138, 143]. Here the beam is split up into four power-balanced beams, which are coupled into optical fibres and make up the 3D-MOT beams. Two beams are counter-propagating and two beams are retro-reflected, such that atoms are illuminated from all six directions. Fourth, a part of the beam is split off as a reference frequency for a 1.5 W commercial TA-SHG laser[†] which is offset-locked to create the ^{171}Yb[‡] 3D-MOT light [143]. The light of this second 556 nm laser is also brought to the cluster using an optical fibre and overlapped with the ^{173}Yb laser beam to create a bi-colour 3D MOT (see Sec. 2.2.5 and Ref. [143]).

The 3D MOT thus traps ^{171}Yb, ^{173}Yb or both isotopes, and the frequency of the 3D MOT beams is broadened [143] to optimise the atom loading and enable capturing atoms from a larger velocity range. After a variable loading time, the 3D MOT is compressed in two steps by reducing the power linearly and by shifting the frequency to resonance. In this way, cold atomic clouds of ^{171}Yb and ^{173}Yb are made with loading rates typically of 4.7×10^6 s^{-1} and 2.5×10^6 s^{-1}, respectively. The minimal temperature that can be achieved in the MOT is the Doppler temperature $T_D = \hbar\Gamma/2k_B$ [158],

---

[*] Toptica BoosTA SHG.

[†] Toptica TA SHG Pro.

[‡] The frequency of this second laser can also be set to the ^{174}Yb intercombination resonance, enabling the creation of ytterbium Bose-Einstein condensates, but this is omitted from this work.
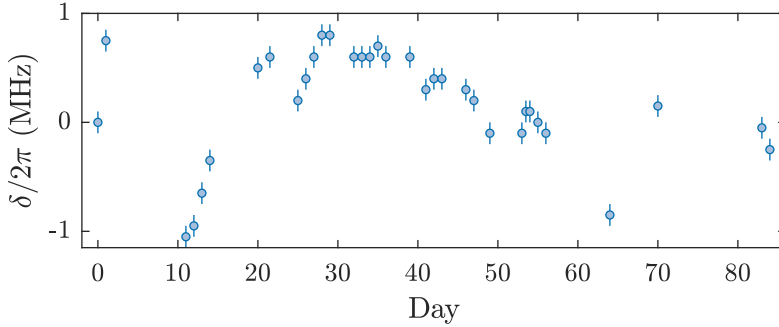
Figure 2.4: Green master laser resonance position drifts due to locking cavity drifts. The detuning is noted with respect to the frequency of day one. The data points are obtained through manual optimisation and error bars indicate the estimated uncertainty of 100 kHz.

where $\hbar$ is the reduced Planck's constant and k_B is the Boltzmann constant, yielding $T_D = 4.37\,\mu K$ for the intercombination transition. The temperatures reached in the experiment were typically $17(2)\,\mu K$ and $15(2)\,\mu K$ for ^{171}Yb and ^{173}Yb, respectively, shown in Fig. 2.5. While this is larger than the Doppler temperature, it is cold enough to efficiently load into the dipole traps. For this measurement, a MOT loading time of $0.5\,s$ was used to capture about 10^6 atoms to ensure the image was not saturated, and the atomic cloud radius is observed as a function of time-of-flight. To obtain the temperature of a ballistically-expanding gas, a fit was made using the expected cloud radius $r_c(t) = (r_{c,0}^2 + 2k_B T t^2/m)^{-1/2}$, where $r_{c,0}$ is the cloud radius at $t = 0$, T is the temperature and m is the atomic mass*. At the temperatures obtained here the gas is still thermal and further cooling is needed to reach quantum degeneracy.

2.2.3 The Green Dipole Trap

Since the magnetic moment of the ground state Yb depends on the nuclear spin while the electronic angular momentum is zero, the magnetic moment of fermionic Yb is about three orders of magnitude smaller than that of alkali atoms such as Rb, which renders magnetic trapping inadequate for our purposes. Hence, a full-optical setup is used, utilising the dipole force of far-off-resonant beams [162]. The optical dipole traps are used for evaporative cooling [158] by lowering the trap depths, initiating the loss of

---

* Here the average thermal velocity $\bar{v}^2 = 2k_B T/m$ was used.
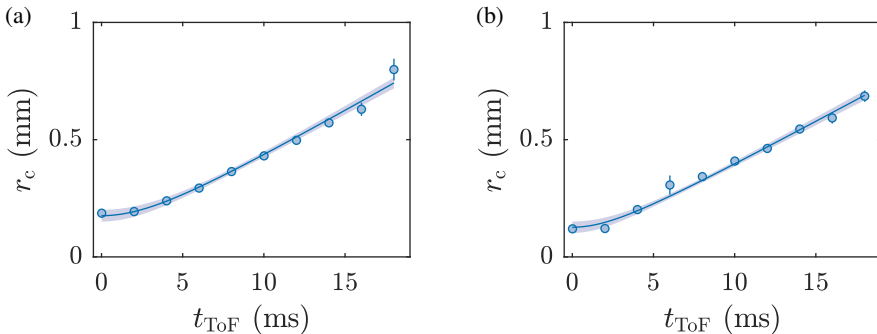
Figure 2.5: 3D MOT temperature measurement, the cloud radius r_c as a function of time-of-flight duration t_{ToF}. Data points are obtained from fits to the atomic cloud and are averaged twice, and error bars denote the standard deviation. The solid lines show the best fit (see text) and the shaded area its 95% confidence interval. (a) and (b) show measurements for ^{171}Yb and ^{173}Yb, with temperatures of 17(2) μK and 15(2) μK, respectively.

atoms with the highest kinetic energies. The remaining atoms rethermalise via elastic scattering and are thus cooled. In this way ^{173}Yb and ^{174}Yb, with s-wave scattering lengths of 199(2)a_0 and 104.9(1.5)a_0 [86], respectively, can be cooled to quantum degeneracy efficiently. Evaporative cooling, however, does not work for ^{171}Yb since its elastic scattering length is $a_{gg} = -3(4)a_0$ [86], preventing it from rethermalising. For this reason, we use *sympathetic cooling* with ^{173}Yb atoms, exhibiting an interisotope ground-ground state scattering length of $-5.8(6) \times 10^2 a_0$ [86], to create degenerate Fermi gases of ^{171}Yb. The interactions between two different isotopes enable the thermalisation of both gases.

As explained in previous theses [126–129], the bi-colour optical trap is chosen to both directly trap atoms from the 3D MOT and to load the quantum gases into the lowest band of an optical lattice. A green dipole trap (GDT) provides the first functionality. A commercial Nd:YAG laser[*] at $\lambda = 532$ nm passes through an AOM, used for power controlling and switching, and passes through a telescope to create a 14 W beam with a waist of 18 μm by 29 μm propagating in the z-direction [129]. At this wavelength, the real part of the polarisability α is negative, such that the dipole force $F_{dip} = \mathrm{Re}(\alpha)\nabla I(\mathbf{r})/2\epsilon_0 c$ is attractive, where $I(\mathbf{r})$ is the Gaussian laser-beam intensity dependent on the position $\mathbf{r}$, ϵ_0 is the permittivity of vacuum and c is the speed of light

---

[*] Coherent VERDI V18.

[162].

After compressing and switching off the 3D MOT, the atoms are held in the dipole traps. The first evaporative cooling stage consists of ramping down the GDT exponentially in 6 s and switching the beam off using an AOM. Sympathetic cooling is done in the same way, except with an isotope mixture (see Sec. 2.2.5).

2.2.4 The Crossed Infrared Dipole Trap

The green dipole trap is overlapped with a crossed dipole trap at $\lambda = 1064$ nm. A commercial laser* at $\lambda = 1064$ nm is split in two beams, each of which passes through an AOM for power controlling and switching. The two beams are coupled into a fibre and transferred to the main experimental table. One beam, referred to as 'IR1', with waists 52.2(1) μm by 51.3(1) μm at 1.5 W [129] on the atoms, is overlapped in the z direction with the GDT. A second beam, 'IR2', with waists 67(4) μm by 192(1) μm at 11.5 W [129] illuminates the atoms along the x-axis. The waist in the direction of gravity was smaller by design to counteract gravitational sag [129].

The second evaporative or sympathetic cooling stage is performed by simultaneously ramping down the power in the IR1 and IR2 beams exponentially in 3 s to about 50% and 75% of the initial power, respectively. The exact final powers were adjusted per experiment to optimise final atom number and temperature. The final trap depths $\omega_{x,y,z}$ in the different directions are typically about $\omega_x = 2\pi\times26.6(5)$ Hz, $\omega_y = 2\pi\times70.5(3)$ Hz and $\omega_z = 2\pi\times24.0(1)$ Hz [129]. In this way, ^{173}Yb DFGs with typically 1.5×10^5 atoms at temperature $T \approx 20\%T_F$ are made, or ^{171}Yb DFGs with about 10^5 atoms at $T \approx 25\%T_F$ [†].

For more details on the design considerations of the dipole traps, see Refs. [125–129].

2.2.5 Creating Fermi-Fermi Mixtures

The setup used to create isotope mixtures was planned by A. Kochanke, B. Hundt and B. Abeln and described in detail in Ref. [138]. Changes after the initial planning were made by B. Abeln and described in Ref. [143]. Here only a brief overview is given.

In order to create pure ^{171}Yb Fermi gases or ^{171}Yb -^{173}Yb mixtures[‡], the following procedure is used. Though the 3D MOT continuously traps ^{171}Yb and ^{173}Yb (see

---

* Coherent Mephisto.

† Over the course of this work, BECs of ^{174}Yb were also made, though not described here since our research focus lies on fermionic ytterbium.

‡ Though the setup was used to create fermionic mixtures, it can also be used to create Bose-Fermi mixtures.

Sec. 2.2.2), the 2D MOT operates at a single frequency. Therefore, the 2D MOT offset frequency starts red-detuned with respect to the $^1S_0 \rightarrow {}^1P_1$ transition of ^{171}Yb and is swept to the ^{173}Yb frequency in 500 ms. In this way we consecutively load ^{171}Yb and ^{173}Yb into the 3D MOT*. We typically load the first isotope for about 4 s to 6 s and the latter for 10 s to 12 s, though the exact timing was varied to obtain the desired isotope ratios in the final mixture[†]. Furthermore, when creating a pure ^{171}Yb DFG, the residual ^{173}Yb atoms used for sympathetic cooling are blasted away on the $^1S_0 \rightarrow {}^3P_1(F' = 7/2)$ transition using a 10 ms pulse.

In this way, we typically create spin-polarised Fermi-Fermi mixtures of 10 to 30 thousand atoms per isotope at temperatures of 25% to 55% T_F. Isotope mixtures created with two spin-polarised isotopes were larger and colder than those with multiple m_F states. Though the cause is as yet unknown, we think this could be because of three-body recombination in non-polarised mixtures, driven by the large attractive interisotope interaction of $-5.8(6) \times 10^2 a_0$ [86].

2.3   Spin Preparation

The nuclear spin of $I = 1/2$ ($I = 5/2$) of fermionic ^{171}Yb (^{173}Yb) atoms allows for the study of interacting spin mixtures with up to two (six) spin states. The nuclear spin of each atom after evaporative cooling is approximately random, resulting in a roughly balanced spin-mixture. To utilise the spin degree of freedom, optical pumping is used to create samples with a tunable atom number in the different spin states, and to image the spin occupations, an optical Stern-Gerlach method is applied, both explained in the following.

2.3.1   Optical Pumping

To enable m_F-state-specific addressing of the atoms, a homogeneous magnetic field of about 18 G is applied. The different nuclear spin states can be addressed separately because the differential Zeeman shift of the $^1S_0 \rightarrow {}^3P_1(F' = 3/2)$ transition is 1.4 MHz/G for ^{171}Yb, whereas it is 597 kHz/G for the $^1S_0 \rightarrow {}^3P_1(F' = 7/2)$ transition of ^{173}Yb[‡]. Then, on-resonant optical pumping [158] on the intercombination transition[§] is used to

---

     * In this way, ^{171}Yb spends more time in the 3D MOT. This order was preferred because of the small scattering length of ^{171}Yb, which is therefore expected to be less sensitive to losses.

     [†] The large difference in loading times is in part caused by the larger MOT loading rate of ^{171}Yb, see Sec. 2.2.1.

     [‡] These were calculated using the Land'e factors, see for instance Ref. [126].

     [§] Note that the hyperfine and isotope splittings of both fermionic isotopes is such that the ^{171}Yb $F' = 3/2$ line is only 2.7 MHz removed from the ^{173}Yb $F' = 3/2$ line (see Fig. 2.1). Hence, optical pumping of ^{171}Yb

excite atoms to the rapidly decaying $^3P_1$ state ($1/\Gamma \approx 870\,$ns [146]), using the circularly-polarised 3D-MOT beams on the z-axis. In this way, the relative number of atoms in each spin can be changed.

Though previously* optical pumping was done before evaporative cooling in the GDT, the spin preparation improved when applying it after the first evaporation stage (as depicted in Fig. 2.2). Throughout this work, spin-polarised gases are typically created in the $m_F = -1/2$ and $m_F = +5/2$ state for ^{171}Yb and ^{173}Yb, respectively. For a more detailed treatment, see Ref. [143].

2.3.2 Optical Stern-Gerlach

For alkali atoms, a Stern-Gerlach method using a magnetic field gradient is typically implemented to spatially separate atoms in different spin states. Due to the small magnetic moment of fermionic ytterbium, experimentally feasible magnetic fields are not large enough for this purpose. Hence, optical Stern-Gerlach [161] is used to split atoms in different nuclear-spin states , relying on the different polarisabilities of m_F states close to resonance†. For a detailed treatment of the theoretical principles, see Refs. [127, 129, 138, 141], and for explanations of the setup see Ref. [127, 129, 138], here only a brief overview is given.

A circularly-polarised laser beam is blue detuned by 1.4 GHz with respect to the $^1S_0 \rightarrow\,^3P_1(F' = 7/2)$ transition of ^{173}Yb [129]. The power is set to about 30 mW, and the beam illuminates the atoms typically for 550 µs. Because the beam comes in under an angle of about 11° with respect to the z-axis, the quantisation axis is turned accordingly. By shining in the beam at the beginning of time-of-flight, the atoms in different m_F states are subject to an m_F-dependent force and are detected separately (see Sec. 2.6 for a typical absorption image).

2.4 The Optical Lattices

After creating a degenerate Fermi gas with the desired number of nuclear spin states, the atoms are loaded into an optical lattice. Optical lattices allow one to study, among others, localised interacting particles, high-resolution clock spectroscopy, and tight-binding models such as the Fermi-Hubbard model [8]. An optical lattice is made using

---

also affects ^{173}Yb. We therefore first perform optical pumping on the former, and then apply optical pumping on the ^{173}Yb $F' = 7/2$ line which is far-detuned from the ^{171}Yb intercombination transition.

  * Such as in the dissipation measurements treated in Ref. [1] and Sec. 6. For more information on the formerly-used optical pumping scheme, see Refs. [128, 129].

  † The difference in polarisabilities is mostly due to the different Clebsch-Gordan coefficients.

interfering laser beams, which create a $\sin^2$-shaped standing wave, and which attract or repel atoms with a dipole force. Due to the Gaussian shape of the individual laser beams, the resulting lattice has the same envelope, though this effect is negligible for our purposes (see App. A).

The polarisabilities α of the orbital states of interest are crucial to the functioning of the optical lattice. The polarisability of a state depends on the transition strengths and wavelengths to all other states, which are thus typically different for different orbital states.

The experimental setup features a *state-dependent lattice* at 660 nm, where the ratio of excited-ground state polarisability is $\alpha_e/\alpha_g \approx 5.5$. Since the excited-state has a much larger polarisability than the ground-state, this enables studying Kondo-like systems [25, 31–34, 163]. Measurements on such systems have been done with ^{171}Yb and are presented in Ref. [143], though are not further discussed here.

Of crucial interest in this work, however, is the existence of a so-called *'magic' wavelength*[*] [14] at 759 nm [164], where the polarisabilities of the ^{1}S$_0$ ground and ^{3}P$_0$ excited states are equal $\alpha_e/\alpha_g = 1$. Because of this, both orbital states are subject to the same dipole potential, preventing site-dependent frequency shifts in high-resolution clock spectroscopy.

2.4.1   The 'Magic' Lattice

The essential information on the experimental realisation of our 'magic' lattice is discussed in the following, though for a detailed treatment, see the theses of A. Thobe [127], B. Hundt [128], N. Petersen [135] and A. Kochanke [129] who have set up the lattice. More recent modifications to the lattice are described in Ref. [143, 144].

A commercial Ti:Saphh laser[†] is used to create a 4.5 W power beam at the 'magic' wavelength. The beam is split up in 5 beams, one for the 1D lattice, three for the 2D lattice and one for the wavelength monitoring with a wavelength meter. Each lattice beam passes through an AOM[‡] and is coupled into an optical fibre. There, the 1D lattice beam (83 μm waist) is focussed on the atoms along the z axis and is retroreflected by a concave mirror to focus the beam back on the atoms. The 2D lattice in the x-y plane is formed by three beams which illuminate the atoms from three sides, such that the incident angles are 120° in between. This creates a traingular, hexagonal or variable AB lattice, depending on the polarisation of the beams [165, 166]. Here, the polarisation

---

[*] A *state-independent wavelength* would be more accurate, though for historic reasons we are stuck with the other name.

[†] Coherent VERDI V18 & MBR 110.

[‡] The AOMs run at -80 kHz and 80 kHz for the 1D and 2D lattices, respectively, to prevent the 1D and 2D lattice from interfering with each other.
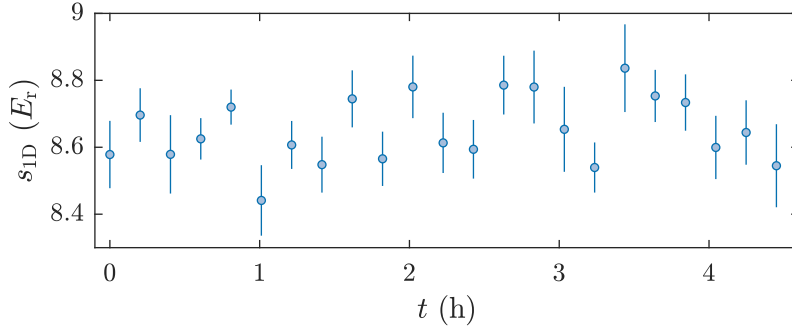
Figure 2.6: Stability measurement of the 1D 'magic' lattice. Data points are the measured 1D lattice depths as obtained from lattice-modulation spectroscopy measurements and error bars indicate the uncertainty in the determination.

is set to create a triangular lattice. This enables us to create lattices of typical depths $s_{1D} \approx 50E_r$ and $s_{2D} \approx 25E_r$, where $E_r = \hbar^2 k^2/2m \approx h \times 2 \, \text{kHz}$ is the recoil energy and $k = 2\pi/\lambda$ is the lattice laser wavenumber.

The calibration of the lattice depth is done by *lattice-modulation spectroscopy* [167]. Here, atoms are loaded into a lattice and the laser power is modulated by a variable frequency. At the interband resonance, atoms are excited from the first lattice band into the third lattice band, enabling the determination of the depth. Calibrations are done prior to each measurement, and typically also after each measurement to check the stability. Additionally, the mid-term stability is further characterised in the following measurement. To this end, 32(1) thousand ^{173}Yb atoms are loaded into a 1D lattice*. The atoms are spin-polarised to prevent interactions of atomic pairs in the lattice. Figure 2.6 shows the resulting 1D lattice depth s_{1D} over the course of about 4.5 hours. Each calibration sequence consists of a series of 23 images, resulting in a single measured 1D lattice depth. Though there are some fluctuations over time, the uncertainty in the determination of each s_{1D} is approximately the same as the spread of the data, implying that systematic effects are small on this timescale.

The lifetime of atoms in a deep lattice is further characterised by loading a spin-polarised ^{173}Yb into a lattice of depths $s_{1D} = 30E_r$ and $s_{2D} = 17E_r$. Figure 2.7 shows the results, where the atom number is observed over various hold times t_h in the lattice, and fitted with an exponential $N(t_h) = N_0 \exp(-t_h/\tau)$, where the initial atom number

---

* During calibrations, only beams that are to be calibrated are switched on. The 2D lattice beams are likewise calibrated pair-wise.
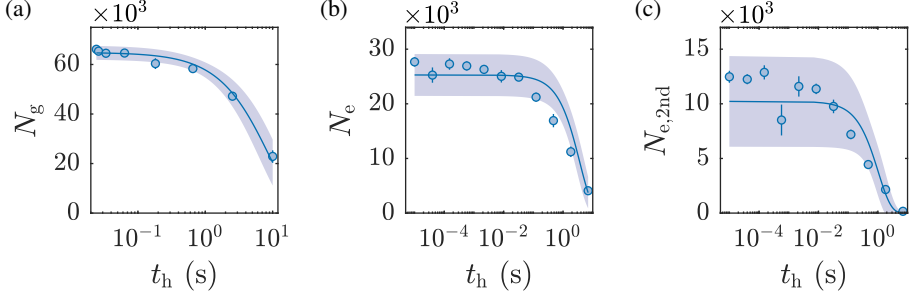
Figure 2.7: Lifetime measurements showing (a) the ground-state atom number N_g, (b) the number of excited-state atoms in the first lattice band N_e and (c) the number of excited-state atoms in the second lattice band $N_{e,2nd}$, as a function of hold time. Data points show the measured atom numbers which are typically averaged 18 times, and the error bars represent the propagated uncertainties. The solid lines show the best fit using an exponential and the shaded areas show the 95% confidence interval. The fits yield lifetimes of $\tau_g = 8.7(9)$ s, $\tau_e = 3.7(4)$ s and $\tau_{e,2nd} = 1.0(2)$ s. Note the log scale of the x axis.

N_0 and lifetime τ are free parameters. Ground state atoms, shown in Fig. 2.7a, have a lifetime of $\tau_g = 8.7(9)$ s. Using a rapid-adiabatic passage (RAP, see Sec. 6.1.1) over the $^1S_0 \rightarrow ^3P_0$ transition, the atoms are brought into the excited state and the same experiment is repeated, yielding a lifetime of $\tau_e = 3.7(4)$ s. Note that a narrow 10 kHz RAP was used to only excite atoms on the carrier transition. The second lattice band lies about 30 kHz higher for this 1D lattice depth, and can thus be addressed separately. Figure 2.7c shows a lifetime measurement of excited-state atoms in the second band of the lattice, where the atoms have a lifetime of $\tau_{e,2nd} = 1.0(2)$ s. Though the cause is unknown, the lifetime of excited-state atoms in the second band could be shorter than those in the first band because the atoms in the first band are subject to a deeper trap.

Since the atoms are spin-polarised, the Pauli exclusion principle prevents double occupation, and thus the various lifetimes quantify the single-body losses. Single atom losses are caused by collisions of residual vacuum atoms* and light scattering due to the lattice-laser light. Excited-state atoms are also lost by spontaneous decay to the ground state, but due to the long natural lifetime $1/\Gamma > 16$ s [24], these are expected to play a minor role. Since the lifetimes are several orders of magnitude larger than the timescale of typical experiments, single-atom losses can often be neglected.

---

* The pressure in the experimental glass cell is below 10^{-11} mbar.

2.5 Exciting Atoms to the $^3P_0$ State

To transfer atoms from the ground state to the long-lived $^3P_0$ excited state, a laser is used, referred to as the clock laser. The setup was designed and built up initially by S. Dörscher [126], A. Thobe [127], T. Rützel [131], J.H. Carstens [133] and R. Le Targat. Later improvements are described by B. Hundt [128], A. Kochanke [129] and T. Ponath [130], and the most recent changes were done by B. Abeln [143]. Here, the setup and functionality is summarised.

A 300 mW power commercial laser* at 578 nm is split up in several beams. A part of the beam is transferred to the experimental table with an optical fibre, where fibre-noise-cancellation [130, 168] is implemented to reduce phase fluctuations caused by mechanical vibrations and temperature fluctuations of the fibre. Using a Pound-Drever-Hall scheme [130, 160], another part of the beam is locked to a high-finesse cavity with a finesse of $\mathcal{F} = 216.9(4) \times 10^3$ and free-spectral range of 1.934(3) GHz [130]. The cavity spacer is made out of ultra-low-expansion (ULE) glass, which has a zero crossing of the expansion coefficient at a temperature of 32.3(1) °C [130]. Since the crucial working principle of all clocks is counting oscillations, it is essential that the light oscillates in the cavity regularly. Using a ULE cavity stabilised to its zero-crossing temperature provides an ultrastable platform for locking the clock laser. A linear-drift compensation is further applied to counteract linear drifts due to small long-term expansion of the ULE spacer [130]. This drift compensation is optimised prior to each spectroscopy measurement, but is typically $-0.11(1)$ Hz/s.

In this way, a short-time laser stability of about 1 Hz within 2 s was found [130]. The full-width-half-maximum of the narrowest single-atom feature measured in spectroscopy was found to be 25 Hz over about 30 minutes (see Sec. 3.2.1). This provides a more than sufficient resolution to spectroscopically measure atomic interactions, which are typically on the order of kHz (see Ch. 4 and 5).

2.6 Imaging

Absorption imaging on the $^1S_0 \rightarrow {}^1P_1$ transition is performed to observe ground-state atoms. Here atoms absorb the resonant laser light and soon after emit it in a random direction, in this way casting a shadow on an EMCCD camera[†] in the beam path. Atomic clouds can be imaged along the x or z axis, though due to the better resolution

---

* Toptica SHG Pro.
† Andor iXon 3A-DU888-DC-QBB.

of the x-axis imaging setup, this axis is predominantly used[*]. The imaging setup was described in detail in Ref. [136] and improvements to the laser setup providing the imaging light are described in Ref. [143].

For each run, four images are taken, the last two of which are without imaging light. The first image is taken after typically 16 ms of time-of-flight (ToF) and images ground-state atoms. Briefly after the first image, the atoms are illuminated with 399 nm light by the perpendicular imaging beam for another 1 ms, which further heats the atoms and blasts them out of focus. The second image after typically 19 ms ToF is therefore empty. By subtracting the second from the first, all inhomogeneities of the beam are accounted for and only ground-state atoms are observed. The third and fourth image are taken after an additional 2 s and 2.05 s but without the imaging light, to measure the background illumination due to ambient light. Illumination times of 20 μs and 50 μs are typically used for the first two and last two images, respectively.

This scheme is adapted to perform double imaging of two isotopes in a mixture. As described in Ref. [143], the two beams are overlapped before being transmitted to the experimental table. These two beams are set to the ^{171}Yb and ^{173}Yb resonance using AOMs[†]. The AOMs further enable fast switching, such that both isotopes are imaged separately in the first two images. Figure 2.8a shows a typical absorption image of a DFG Fermi-Fermi mixture, where ^{171}Yb and ^{173}Yb are imaged consecutively. Note that due to the subtraction, atoms in the second image show up as having a negative optical density (OD), which is accounted for in the image analysis [143].

Alternatively, the ground and excited state can be measured by using a so-called repumper technique. The first image again measures the ground-state atoms, and a 1 ms blast pulse over the other axis removes these atoms. This light is far off-resonant with respect to the excited-state atoms, so these are unaffected. A 1 ms pulse on the $^3P_0 \rightarrow {}^3D_1$ line at $\lambda = 1388$ nm transfers all excited-state atoms to the $^3D_1$ state, which rapidly decays into the ground state via the $^3P_1$ state (compare Fig. 2.1). The illumination time is chosen such that atoms decaying back into the clock state are excited again, until about 97.5% of the excited-state atoms end up in the $^3P_1$ state [129]. The remaining 2.5% of the atoms decay into the long-lived $^3P_2$ state, which is accounted for in the atom-number analysis. After another 0.9 ms ToF, the formerly-excited-state atoms are imaged on the $^1S_0 \rightarrow {}^1P_1$ transition. In this way, both orbital states are observed[‡].

---

[*] Imaging along the z axis is done to calibrate the 2D lattice, which is in the x-y plane. For all other measurements in this work, imaging is done along the x axis.

[†] Though generally the frequencies can also be set to the $^1S_0 \rightarrow {}^1P_1$ resonance of ^{174}Yb to investigate other mixtures.

[‡] Though for mixtures this technique can be used to observe ground-state atoms in one isotope and excited-state atom in the other isotope, it is typically more useful for us to image both orbital states of the same isotope. This enables us to normalise the excited-state atoms to the total atom number, which accounts
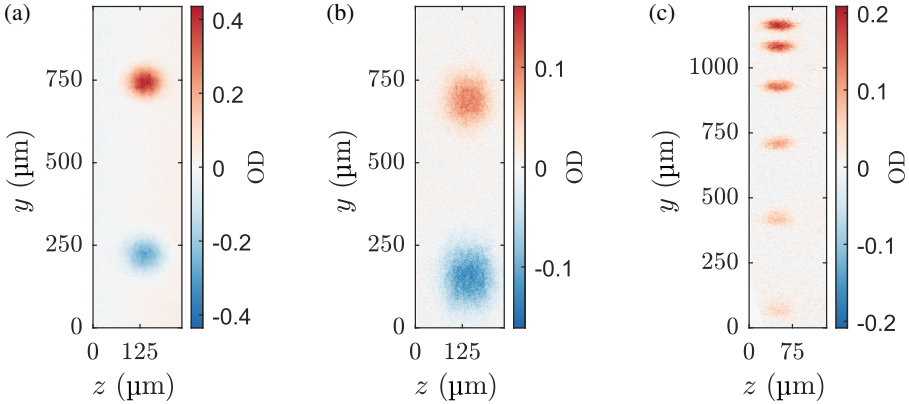
Figure 2.8: Typical absorption images of various atomic clouds, showing $I_1 - I_2 - I_{bg}$. Atoms in the first and second image show up as positive and negative OD, respectively. (a) Double imaging of a spin-polarised ^{171}Yb (red) and ^{173}Yb (blue) ground state mixture. (b) Double imaging of $^1S_0$ ground (red) and $^3P_0$ excited state (blue) atoms of a spin-polarised ^{173}Yb gas in a magic lattice. (c) OSG imaging of ground state ^{173}Yb. The six clouds have nuclear spins $m_F = -5/2$ to $m_F = 5/2$ from top to bottom.

The repumper scheme explained here does not conserve the spin of the excited state, due to the two decay channels from the $^3D_1$ state. Since this information is important for certain measurements, several upgrades for the repumper scheme have been conceived, and are explained in Ref. [142].

Figure 2.8b shows a typical absorption image with the repumping scheme, where about half of the atoms is in the ground state (red) and the other half in excited state (blue). Additionally, a typical OSG image of ^{173}Yb is shown in Fig. 2.8c, where the six different nuclear spin states are clearly separated spatially. Using fits to the linesums over the z axis, the relative occupation per spin state can be found [143].

2.7 Conclusion

With the brief overview of the interesting features of ytterbium and the experimental apparatus, we continue to experiments performed on interacting fermionic ytterbium in optical lattices excited on the clock transition. In the following chapters, high-

---

for atom number fluctuations and thus greatly reduces noise.

resolution clock spectroscopy is explained and performed to measure interorbital spin-exchanging interactions of ^{171}Yb and to measure interorbital interisotope interactions in highly-symmetric $^{171}_{e/g}$Yb -$^{173}_{g/e}$Yb Fermi-Fermi mixtures. Lastly, clock excitation will be used to study dynamics in the dissipative Fermi Hubbard model, showing the build-up of strong spin-correlations compatible with the creation of a highly-entangled Dicke state.

Chapter 3

Clock Spectroscopy of Polarised Gases

One of the largest appeals of using ultracold ytterbium atoms for lattice experiments is the existence of a long-lived excited state. As discussed before, the $^3P_0$ excited states is connected to the $^1S_0$ ground state by a very narrow clock transition, which can be addressed with a narrow-frequency laser to directly measure small energy shifts caused by interactions between atoms in a lattice.

In this chapter the basic principles of clock excitation are discussed in the context of the well-known quantum two-level systems, where two orbital atomic states are coupled by a light field which is far off-resonant from all other transitions. A two-level system is used to describe single atoms, realised by spin-polarised Fermi gases in a 'magic' lattice, which are non-interacting due to the Pauli exclusion principle. Two-atom interactions are introduced in the next chapter.

This chapter is built up as follows. After a theoretical treatment of two-level systems and the resulting Rabi oscillations and spectra, the effect of linear drifts and the effect of different decay mechanisms is discussed. In the second half, measurements of Rabi oscillations and spectra are shown, which are described well by the two-level description.

The work in this chapter was supervised by K. Sengstock & C. Becker. The theory plots in this chapter were made by the author. The measurements were taken by B. Abeln, M. Diem and the author, and the analysis was done by B. Abeln and the author.

3.1   Two-Level Systems

The physics of two-level systems is well-established and has been treated in many textbooks [158, 169]. Here, only a brief overview is given.

The main assumption for a two-level system treatment is that a light field couples only two atomic states. To satisfy this condition, both the atomic linewidth and the light field frequency need to be narrow compared to other atomic transitions. With an atomic linewidth of less than $10\,\text{mHz}$ [24] (see Fig. 2.1) and a short-term laser linewidth of as little as $1\,\text{Hz}$ in $2\,\text{s}$ [130], this criterion is easily satisfied, since the nearest transition is $20\,\text{THz}$ removed. Using the rotating wave approximation and the electric dipole approximation [158], the probability of measuring an atom in the excited state n_e is given by [158]

$$n_\text{e}(\delta, t_\text{p}) = |c_\text{e}(\delta, t_\text{p})|^2 = \frac{\Omega_0^2}{\Omega_0^2 + \delta^2}\sin^2\left(\sqrt{\Omega_0^2 + \delta^2}\,t_\text{p}2\right), \qquad (3.1)$$

where c_e is the excited-state occupation coefficient, Ω_0 is the bare Rabi frequency, and $\delta = \omega_\text{c} - \omega_0$ is the detuning, where ω_c and ω_0 are the clock laser and resonance frequencies, respectively. Here illumination with a square pulse of duration t_p is assumed. Further note that Ω_0 and δ are given as angular frequencies.

To get an intuition of the excitation probability, the excitation probability is plotted n_e for several circumstances. Figure 3.1a shows the excitation probability as a function of pulse time t_p for four fixed detunings δ, assuming the atom starts in the ground state prior to illumination. The resulting oscillations of n_e as a function of pulse time are called *Rabi oscillations*. On resonance $\delta = 0$ (the solid line in Fig. 3.1a) the probability of measuring the atom in the excited state increases and reaches unity at $t_\text{p} = \pi/\Omega_0$. This is referred to as a π-pulse, which is one way of transferring atoms from the ground to the excited state[*]. When illuminating the atom for longer than a π pulse, the excitation probability decreases as the atom oscillates between the ground and excited state.

Away from resonance $\delta \neq 0$, shown as the dotted, dash-dotted and dashed lines in Fig. 3.1a, the maximum excitation probability does not reach unity, since the maximum n_e is given by $\Omega_0^2/(\Omega_0^2 + \delta^2)$. Furthermore, the frequency of the oscillation increases for increasing δ. Because of this change in frequency, a new quantity is often defined: the *effective Rabi frequency* $\Omega_\text{eff} = \sqrt{\Omega_0^2 + \delta^2}$.

Figure 3.1b shows the excitation probability n_e as a function of detuning δ for four different fixed pulse times t_p, referred to as *spectra*, since they can be used to measure energy differences in multi-component systems. In spectra made with π-pulse

---

[*] Another method is to use a rapid-adiabatic passage, as explained in Sec. 6.1.1.

(a)

(b)
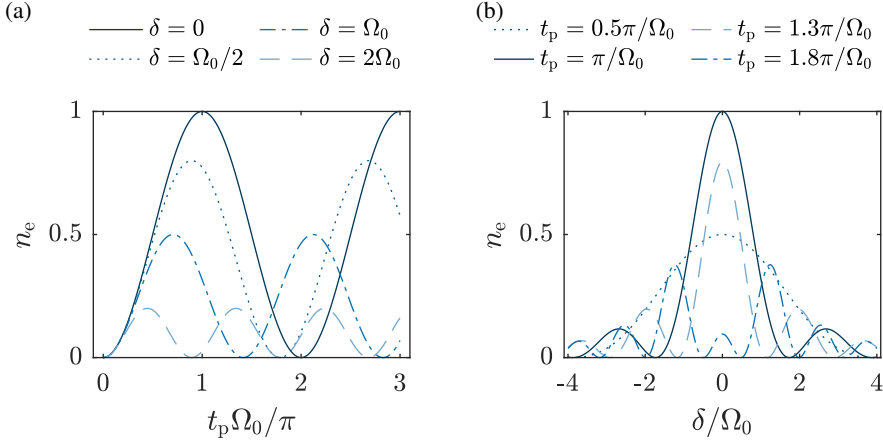
Figure 3.1: (a) Rabi oscillations: the excitation probability as a function of pulse time, here plotted as a dimensionless quantity $t_p\Omega_0/\pi$. The different lines indicate various detunings (see legend). (b) Spectra: the excitation probability as a function of detuning, here plotted as a dimensionless quantity δ/Ω_0. The different lines indicate various pulse times (see legend).

illumination (solid line), the excitation probability reaches $n_e = 1$ on resonance, and away from resonance, it goes down to zero and has secondary peaks. These secondary peaks are referred to as *sinc lobes* throughout this work, and these are a characteristic sign of a sinc^2 function[*]. For a $\pi/2$-pulse (dotted line) the shape of the spectrum remains the same, but the maximum peak height becomes 1/2. At a larger pulse time of $t_p = 1.3\pi/\Omega_0$ (dashed line) the spectrum still looks distinctively like a sinc^2, though the maximum peak height is smaller than one, even on resonance. However, here the height of the sinc lobes compared to the central peak is larger than it is for a π-pulse, both absolutely and relatively to the peak height. For a pulse time of $t_p = 1.8\pi/\Omega_0$ (dash-dotted line) the spectrum consists of two equally-high peaks, and a small peak on resonance (which disappears completely for $t_p\Omega_0/\pi = 2$). Spectra exhibit this two-peak feature between $1.63 \lesssim t_p\Omega_0/\pi < 3$[†].

Further note that spectra are symmetric, which can also be seen by evaluating

---

[*] Recall that the definition of a sinc is $\text{sinc}(ax) = \sin(ax)/(ax)$ for any $a \neq 0$, and note that n_e is a sinc^2 as a function of δ.

[†] For longer times below $(3 + 2k)\pi/\Omega_0$ for $k \in \mathbb{N}$ there are further spectra with two main peaks, but no exact function exists for the lower boundary due to the nature of sinc^2 functions.
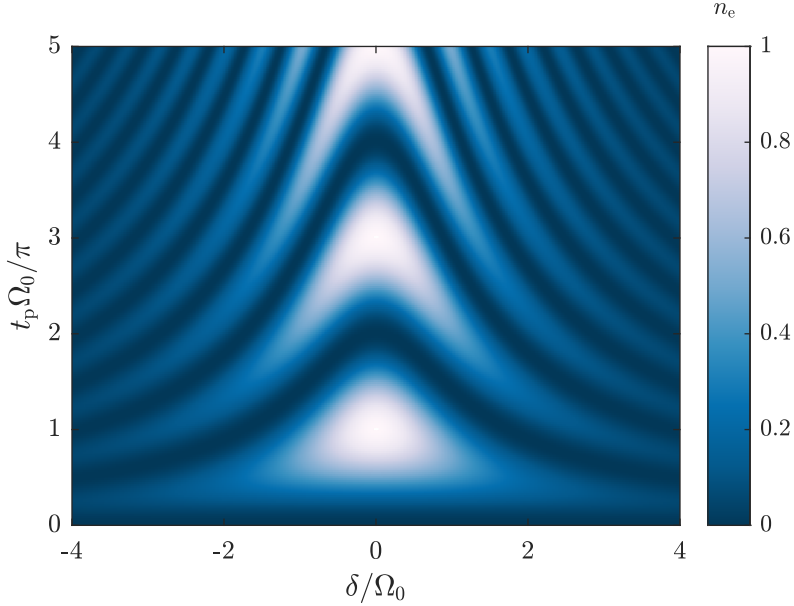
Figure 3.2: Excitation probability as a function of both the dimensionless detuning δ/Ω_0 and the dimensionless pulse time $t_\mathrm{p}\Omega_0/\pi$. The colour (z-axis) shows the excitation probability.

Eq. 3.1, since $n_\mathrm{e}(\delta, t_\mathrm{p}) = n_\mathrm{e}(-\delta, t_\mathrm{p})$. The width of the peak on resonance is inversely proportional to the pulse time, since the sinc^2 in the frequency domain is the Fourier transform of the square pulse in the time domain. A Fourier-limited spectrum is one where the peak width is the minimum it can be due to Fourier broadening.

Having considered Rabi oscillations and spectra separately, now consider the excitation probability as function of both detuning and pulse time simultaneously. Figure 3.2 shows the excitation probability n_e as a function of dimensionless detuning δ/Ω_0 and pulse time $t_\mathrm{p}\Omega_0/\pi$, where the colour indicates the excitation probability. In this representation, Rabi oscillations are vertical cuts, and spectra are horizontal cuts. Over the whole plotted area, the excitation probability goes through multiple maxima and minima for various combinations of (δ, t_p).

3.1.1 The Effect of Linear Frequency Drifts

Real experiments are often prone to drifts of the laser frequency, which are to first order linear in time[*]. Consider the effective detuning δ_{eff} under the effect of a linear drift $\Delta\delta_{\text{drift}}$

$$\delta_{\text{eff}}(t) = \delta + \Delta\delta_{\text{drift}}t, \tag{3.2}$$

where t is the time after the beginning of the experiment. In this definition, δ is the set value of the detuning in the experiment and δ_{eff} is the real detuning of the light illuminating the atom. Further note that $\Delta\delta_{\text{drift}}$ has units of $1/s^2$.

Figure 3.3a shows the effect of linear frequency drifts on Rabi oscillations, where the excitation probability is $n_{\text{e}}(\delta_{\text{eff}}, t_{\text{p}})$ is plotted as a function of dimensionless time, such that the timescale is given by π/Ω_0. Three cases are plotted. Rabi oscillations on resonance and without drifts are shown as the solid line for comparison. The dashed line shows Rabi oscillations with $\delta_{\text{eff}}(t_{\text{p}})/\Omega_0 = -1/3 + t_{\text{p}}\Omega_0/(9\pi)$, which is a Rabi oscillation which starts off-resonance, consecutively drifts to and then away from resonance. The first Rabi peak at $t_{\text{p}}\Omega_0/\pi = 1$ does not reach unity because it is not on resonance, but at $t_{\text{p}}\Omega_0/\pi = 3$, the interrogation frequency has drifted on resonance such that $n_{\text{e}} = 1$. For larger times, however, the peak heights decrease and the oscillation frequency increases. The dash-dotted line shows oscillations which start on resonance and drift away as $\delta_{\text{eff}}(t_{\text{p}})/\Omega_0 = t_{\text{p}}\Omega_0/(9\pi)$. The first peak reaches an excitation probability close to unity, whereas later peaks decrease in height steadily, and the effective Rabi frequency increases. Lastly, note that the minima go to zero, regardless of which drift is chosen.

The effect of linear frequency drifts on spectra is markedly different. Consider the excitation probability $n_{\text{e}}(\delta_{\text{eff}}, \pi/\Omega_0)$ as a function of the detuning δ, not of the effective or real detuning. This is a similar situation to what one has in experiments, where the set detuning is known, while an unknown drift changes the real detuning that affects the atoms. This thus gives an intuition about the effect of different drifts on spectra.

Figure 3.3b shows three spectra with different drifts. The solid line shows a spectrum without any drifts, whereas the dashed and dash-dotted lines show drifts of $\Omega_0^2/4$ and $-\Omega_0^2/4$[†], respectively. In other words, over the duration of whole spectrum, the former exhibits a drift of $+2/\Omega_0$ and the latter a drift of $-2/\Omega_0$. First of all note that the peak height does not change, whereas the position does. This can be understood by considering δ_{eff}. The peak of the spectrum is at $\delta_{\text{eff}} = 0$, so for $\delta = -\Delta\delta_{\text{drift}}t$ (see Eq. 3.2). The 'resonance' peak therefore artificially shows up below (above) resonance

---

[*] Though in our experiments a linear drift compensation is applied to counteract this effect (see Sec. 2.5), one can never perfectly compensate for this. The residual, uncompensated linear drifts during measurements are typically orders of magnitude smaller than those used here.

[†] The zero-point of time is $\delta/\Omega_0 = -4$, such that the spectrum is scanned from left to right.
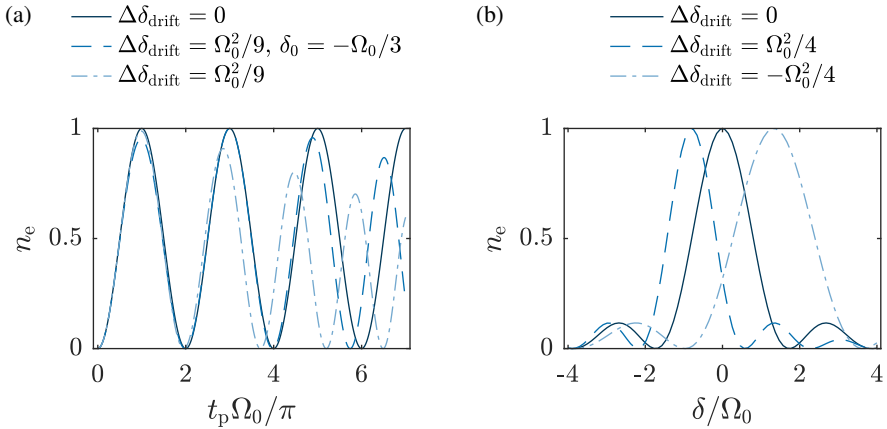
Figure 3.3: (a) Rabi oscillations under the influence of linear frequency drifts. The solid line shows Rabi oscillations for $\delta(t_\mathrm{p}) = 0$, the dashed line has a detuning of the form $\delta_\mathrm{eff}(t_\mathrm{p})/\Omega_0 = -1/3 + t_\mathrm{p}\Omega_0/(9\pi)$, and the dash-dotted line has a detuning of $\delta_\mathrm{eff}(t_\mathrm{p})/\Omega_0 = t_\mathrm{p}\Omega_0/(9\pi)$. (b) Excitation spectra under the influence of linear frequency drifts. The solid line has no drifts, the dashed line shows a drift of $\Delta\delta_\mathrm{drift} = \Omega_0^2/4$ and the dash-dotted line shows a drift of $\Delta\delta_\mathrm{drift} = -\Omega_0^2/4$. Here time is in units of $1/\Omega_0$ and the zero-point of time is chosen to be $\delta/\Omega_0 = -4$.

for positive (negative) drifts. Drifts furthermore change the width of the peak. For positive drifts, the peak becomes narrower, whereas it becomes broader for negative drifts. The peaks however remain symmetric around the peak.

3.1.2 The Effect of Spontaneous Decay & Decoherence

In the following the effect of two decay mechanisms are considered: spontaneous decay from the excited to the ground state, and decoherence. To do so, the description of the previous section is extended by studying the time evolution of the density matrix ρ [158]

$$\rho = \begin{pmatrix} \rho_\mathrm{ee} & \rho_\mathrm{eg} \\ \rho_\mathrm{ge} & \rho_\mathrm{gg} \end{pmatrix}, \tag{3.3}$$

where the matrix elements are given by $\rho_\mathrm{ab} = c_\mathrm{a}c_\mathrm{b}^*$, where the subscripts 'a' and 'b' indicate the orbital state. Note that previously only $n_\mathrm{e} = |c_\mathrm{e}|^2$ was considered.

The differential equations governing the time evolution of the density matrix are the well-known optical Bloch equations. In the rotating frame where $\tilde{\rho}_{ab} = \rho_{ab}e^{i\omega_c t}$ these are given by [158, 169]

$$\frac{d\rho_{ee}}{dt} = i\frac{\Omega_0}{2}\left(\tilde{\rho}_{eg} - \tilde{\rho}_{ge}\right) - \Gamma_s\rho_{ee}$$

$$\frac{d\rho_{gg}}{dt} = -i\frac{\Omega_0}{2}\left(\tilde{\rho}_{eg} - \tilde{\rho}_{ge}\right) + \Gamma_s\rho_{ee}$$

$$\frac{d\tilde{\rho}_{ge}}{dt} = -(\Gamma_\perp + i\delta)\tilde{\rho}_{ge} - i\frac{\Omega_0}{2}(\rho_{ee} - \rho_{gg})$$

$$\frac{d\tilde{\rho}_{eg}}{dt} = -(\Gamma_\perp - i\delta)\tilde{\rho}_{ge} + i\frac{\Omega_0}{2}(\rho_{ee} - \rho_{gg}),$$

(3.4)

where Γ_s is the rate of spontaneous decay from the excited to the ground state and $\Gamma_\perp$ is the damping rate of the coherence, or the decoherence rate.[*] The decoherence is given by $\Gamma_\perp = \Gamma_s/2 + \Gamma_c$, where Γ_c accounts for additional decoherence effects which do not change the excitation probability, such as dephasing collisions and finite laser linewidth [169, 170]. Because spontaneous decay also affects the total decoherence rate $\Gamma_\perp$, in the following the effect of spontaneous decay Γ_s and the additional decoherence Γ_c is studied separately.

In general, Eqs. 3.4 cannot be solved analytically and the differential equations are therefore solved numerically[†]. To unambiguously determine the effect of the two decay mechanisms, the calculations are performed on resonance and without frequency drifts.

Figure 3.4 shows Rabi oscillations under the effect of the two decay mechanisms (dashed and dash-dotted lines) in comparison to unperturbed Rabi oscillations (solid line). Both decay mechanisms result in a damping of the Rabi oscillations, i.e. the amplitude of the oscillation decreases over time. Therefore, particles subject to significant spontaneous decay or decoherence neither fully reach $|g\rangle$ nor $|e\rangle$ for non-zero illumination times[‡]. Since off-resonant Rabi oscillations (see Fig. 3.1a) and Rabi oscillations with drifts (see Fig. 3.3a) do reach $n_e = 0$ for non-zero times, this can be used to distinguish which processes play a significant role in experiments. Finally, note that the same decay rates Γ_s and Γ_c yield different dampings, which can be understood by considering Eqs. 3.4, where Γ_s and Γ_c enter differently.

The effect of spontaneous decay and additional decoherence on spectra is shown in Fig. 3.5 (dashed and dash-dotted lines) in comparison to a spectrum without de-

---

[*] Furthermore, $\tilde{\rho}_{ee} = \rho_{ee}$ and $\tilde{\rho}_{gg} = \rho_{gg}$ was used.[169]

[†] The code used to numerically solve the optical Bloch equations for Rabi oscillations was made by B. Abeln and extended by the author to enable studying the effect of the decay mechanisms on spectra.

[‡] In fact, for these calculations on resonance the excitation probability approaches $n_e = 1/2$ for times large compared to the decoherence time $1/\Gamma_c$.
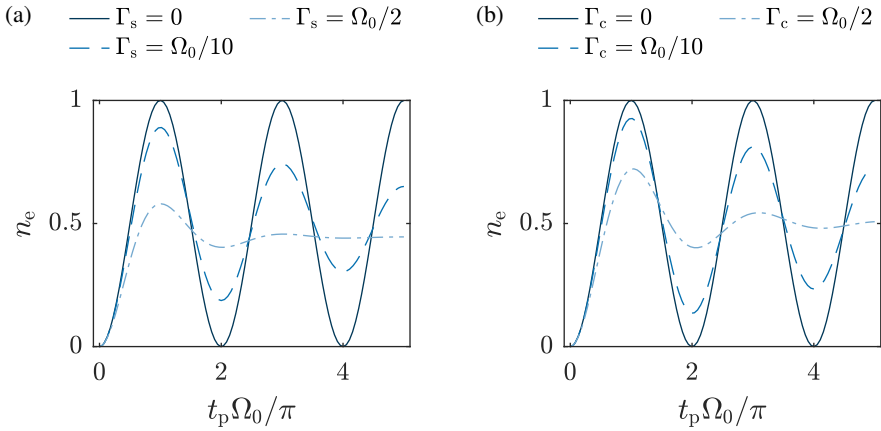
Figure 3.4: Rabi oscillations under the effect of spontaneous decay and decoherence. All calculations are done on resonance and no drifts are assumed. (a) Rabi oscillations for various spontaneous decay rates, without decoherence. The solid line shows a Rabi oscillation without spontaneous decay, the dashed line has a spontaneous decay of $\Gamma_s = \Omega_0/10$ and the dash-dotted line has a spontaneous decay of $\Gamma_s = \Omega_0/2$. (b) Rabi oscillations for various additional decoherence rates, without spontaneous decay. The solid line has no decoherence, the dashed line has an additional decoherence of $\Gamma_c = \Omega_0/10$ and the dash-dotted line has an additional decoherence of $\Gamma_c = \Omega_0/2$.

cay (solid line). There are two important features for both decay mechanisms. For increasing decays Γ_s and Γ_c, the central peak height decreases, even though π-pulses are considered. Furthermore, the sinc lobes become less distinct as decay strengths increase. Without any decay, the spectrum is exactly zero at $\delta/\Omega_0 = \pm \sqrt{3}^*$, but for finite decay rates this becomes non-zero. This effect is especially pronounced for additional decoherences Γ_c, whereas for spontaneous decay this effect becomes noticeable at large decay rates.

The influence of different effects of Rabi oscillations and spectra have now been studied. These basic examples will serve as a reference to evaluate which effects (off-resonance, non π-pulses, frequency drifts and decay) significantly affect our experiments, described in the following.

---

* In general for π-pulses, spectra without decay are zero for $\delta/\Omega_0 = \pm \sqrt{4k^2 - 1}$ where $k \in \mathbb{N}$.
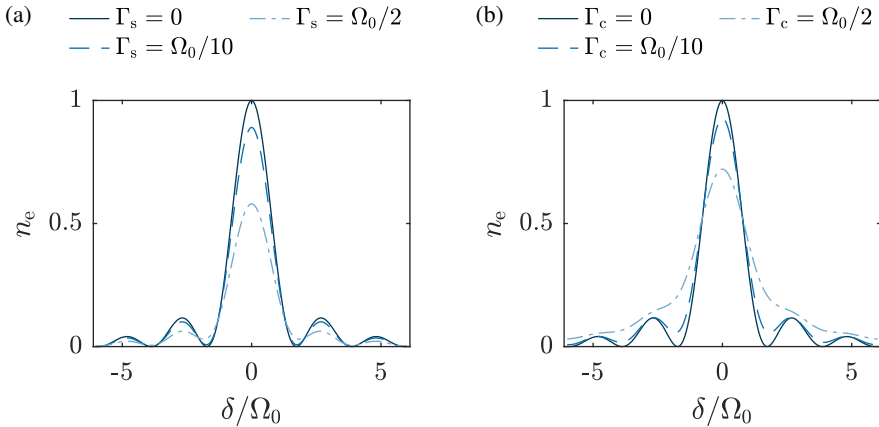
Figure 3.5: Excitation spectra under the effect of spontaneous decay and decoherence. All calculations are done for π-pulses and no drifts are assumed. (a) Spectra for various spontaneous decay rates, without decoherence. The solid line shows a spectrum without spontaneous decay, the dashed line has a spontaneous decay of $\Gamma_s = \Omega_0/10$ and the dash-dotted line shows a spontaneous decay of $\Gamma_s = \Omega_0/2$. (b) Spectra for various additional decoherence rates, without spontaneous decay. The solid line has no decoherence, the dashed line shows an additional decoherence of $\Gamma_c = \Omega_0/10$ and the dash-dotted line shows an additional decoherence of $\Gamma_c = \Omega_0/2$.

3.2 Measuring Rabi Oscillations & Spectra

In order to experimentally study clock excitation of spin-polarised gases, a Fermi gas of either [171]Yb or [173]Yb is created and optical pumping is applied to transfer all atoms to a single m_F state (see Sec. 2.3.1). The Pauli exclusion principle prevents the identical particles from occupying the same lattice site, thus yielding an simple system to study single-body effects.

When performing clock spectroscopy or driving Rabi oscillations on a sample of many atoms in a deep lattice, n_e will be referred to as the *excitation fraction* or *excitation ratio* instead of probability. The excitation fraction is given by

$$n_e = N_e/(N_e + N_g), \tag{3.5}$$

where N_e and N_g are the number of atoms in the excited and ground state, respectively. In a deep lattice, tunnelling times are large compared to clock interrogation times and
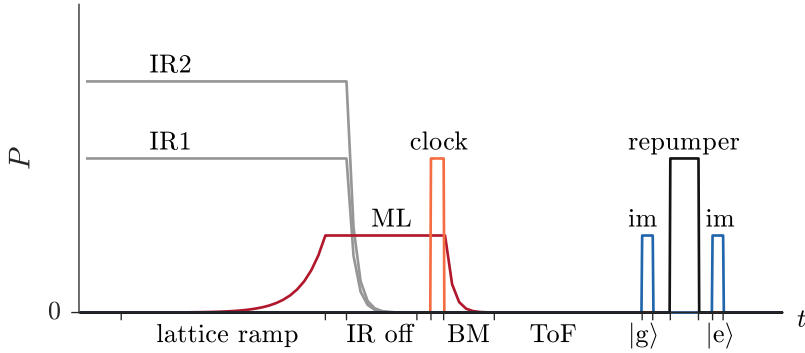
Figure 3.6: Schematic of a spectroscopy sequence (not to scale), showing the laser beam powers P as a function of time t. The grey lines show the 1064 nm dipole trap beams (IR1 & IR2), the red line shows the 'magic' lattice (ML) beams, the yellow line shows the clock pulse, the blue line shows the imaging pulses (im) and the black line shows the repumper pulse. The different time steps are indicated below the x-axis (see text).

other timescales, and therefore each lattice site can be regarded as an isolated single-atom system. Furthermore, the resonance frequency is equal over the whole sample, since atoms in the $|g\rangle$ and $|e\rangle$ state are subject to the same potential regardless of depth because of the 'magicness' of the lattice (see Sec. 2.4.1). Measuring the fraction of atoms in the excited state therefore corresponds to measuring the excitation probability.

Before one can drive controlled Rabi oscillations with reasonable excitation fractions, the resonance frequency must be known, and this can be found by performing spectroscopy. Therefore, measurements of spectra are first considered, before moving on to Rabi oscillations, and closing the chapter with the excitation fraction as a function of both detuning and pulse time.

3.2.1 Spectroscopy Measurements

Figure 3.6 shows a schematic of the experimental sequence used to perform clock spectroscopy. After creating a degenerate Fermi gas as described in Sec. 2.2.4 with a single spin component (see Sec. 2.3.1), the 'magic' lattice is ramped up exponentially (see Sec. 2.4.1) to load the atoms into the lowest band of the lattice, typically using a total ramp time of 200 ms.

After a short time the 1064 nm dipole traps are ramped down in 3 ms and switched off (IR off). The atoms are now trapped solely by the 'magic' lattice to prevent light shifts during clock excitation, and after a hold time of about 10 ms, all atoms are illuminated in the lattice with a rectangular clock pulse. Subsequently, band mapping (BM) is performed by exponentially ramping down the lattice in 500 μs to map the lattice momenta onto free momenta [167]. After a time-of-flight (ToF) of typically 16 ms the $|g\rangle$ ground state atoms are imaged on the $^1S_0 \rightarrow {}^1P_1$ transition (see Sec. 2.6). Since the $|e\rangle$ excited clock state atoms are dark to this transition, a 1 ms repumper pulse is applied on the $^3P_0 \rightarrow {}^3D_1$ transition to transfer the atoms to the ground state via the intermediate short-lived $^3P_1$ state (see Sec. 2.6 and Ref. [129]). After the repumper pulse, the former excited-state atoms are imaged, yielding the number of excited- and ground-state atoms N_e and N_g, respectively. By varying the clock-laser frequency, the detuning is changed and a spectroscopy measurement is performed.

This scheme provides a starting point for a variety of further research. As discussed in the following chapters, different parts of the scheme are varied to measure different physical quantities. One can, for instance, load a spin-mixture and observe inter-orbital spin-exchanging interactions (see Chap. 4), load interacting Fermi-Fermi mixtures into the lattice and measure elastic and inelastic interaction (see Chap. 5), or observe inhibition of losses in excited-state spin mixtures (see Chap. 6).

High-Resolution Clock Spectroscopy

Following the scheme described in Sec. 3.2.1, high-resolution clock spectroscopy is performed in a deep lattice with depths $s_{1D} = 60E_r$ and $s_{2D} = 25E_r$. A linear-drift compensation of -0.104 Hz/s was applied to counteract linear frequency drifts of the clock cavity (see Sec. 2.5). A magnetic field of 1.5 G in the y-direction was used to set the quantisation axis.

Figure 3.7 shows typical clock spectroscopy of spin-polarised gases, where the clock beam intensity I_c and pulse time t_p are changed for each spectrum. First, consider Fig. 3.7b, where the clock beam intensity is set to about 1.6 mW/cm^2 and a spectroscopy measurement is done with a pulse time of 15 ms. The expected sinc^2 shape of the excitation peak is clearly observed, with the first sinc lobes at around ±90 Hz. However, the maximum excitation does not reach $n_e = 1$, which one expects for a π-pulse without additional effects (see Fig. 3.1b).

The spectrum is fitted using Eq. 3.1 where Ω_0 and the resonance frequency ω_0 are free parameters and a small offset is added to improve the fit. The fit describes the data well and yields a Rabi frequency of $\Omega_0 = 2\pi \times 21.4(3)$ Hz, and the resolution of the peak, or full-width-half-maximum (FWHM), is 57 Hz. Here the resonance position ω_0 was used to centre the detuning around zero.
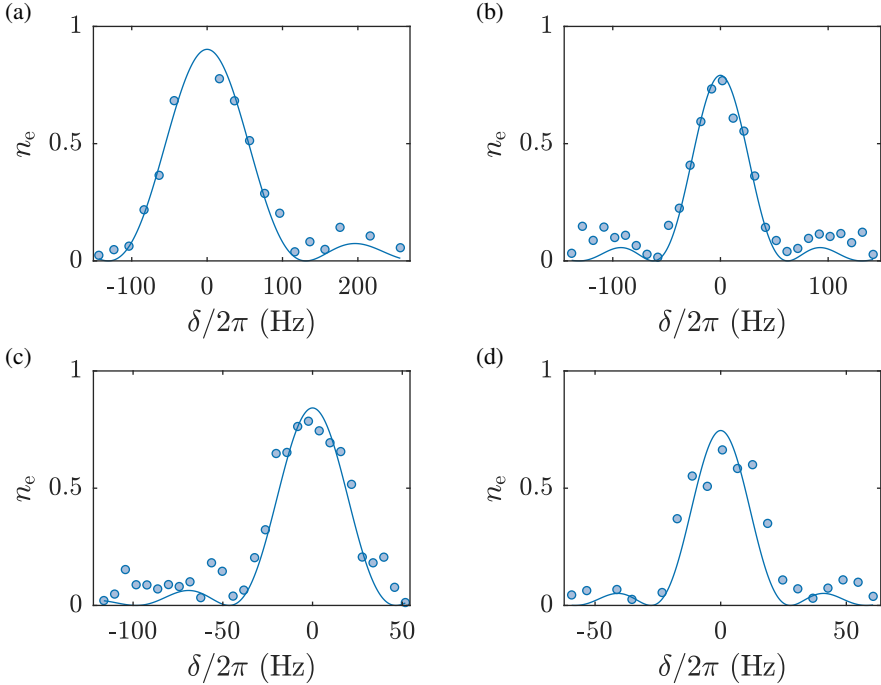
Figure 3.7: High-resolution spectroscopy of spin-polarised samples in a deep lattice ($s_{1D} = 60E_r$, $s_{2D} = 25E_r$) for various clock beam intensities I_c and pulse times t_p. The points indicate the measured excitation fraction and the solid line indicates a fit (see text). (a) shows a spectrum using $I_c = 1.6\,\text{W/cm}^2$ and $t_p = 7\,\text{ms}$, where the fit yields $\Omega_0 = 2\pi \times 57(3)\,\text{Hz}$ and a FWHM of 119 Hz. (b) shows a spectrum using $I_c = 1.6\,\text{mW/cm}^2$ and $t_p = 15\,\text{ms}$, where the fit yields $\Omega_0 = 2\pi \times 21.4(3)\,\text{Hz}$ and a FWHM of 56 Hz. (c) shows a spectrum using $I_c = 0.7\,\text{mW/cm}^2$ and $t_p = 20\,\text{ms}$, where the fit yields $\Omega_0 = 2\pi \times 18.5(6)\,\text{Hz}$ and a FWHM of 42 Hz. (d) shows a spectrum using $I_c < 0.3\,\text{mW/cm}^2$ and $t_p = 34\,\text{ms}$, where the fit yields $\Omega_0 = 2\pi \times 8.5(7)\,\text{Hz}$ and a FWHM of 25 Hz.

To understand the non-unity peak height, the effects discussed in Sec. 3.1 are considered. These are spontaneous decay and decoherence, and deviations from the desired π-pulse area. In experiments, however, an additional effect enters: the spin preparation. Imperfections in optical pumping (see Sec. 2.3) can cause a small fraction of

the atoms to remain in unwanted m_F states. These are imaged and therefore show up in the denominator of $n_e = N_e/(N_e + N_g)$, yet cannot be excited because the differential Zeeman splitting between the $|e\rangle$ and $|g\rangle$ states causes a shift in resonance position of about $\Delta m_F \times 170$ Hz at the magnetic field used here. Therefore, the maximum excitation fraction is reduced by the fraction of other m_F states. To account for this, a factor is added in front of n_e and the fit is repeated. The factor, characterising the fraction of atoms in the desired m_F state, was not significantly different from one and importantly did not improve the fit, therefore suggesting that residual unwanted spin states are not the predominant explanation for the non-unity peak height.

The two decay mechanisms considered also cannot explain the peak height. As measured before (see Sec. 2.4.1), one-body losses in the deep lattice are characterised by a decay rate of about 0.3 Hz, which is more than 50 times smaller than Ω_0, indicating that this has a negligibly small effect. Furthermore, decoherence due to collisions is expected to play no role in this experiment, since atoms are prevented from tunnelling by the Pauli principle. Decoherence washes out the characteristic sinc^2 shape of the spectrum (see Fig. 3.5b), so the fact that excitation ratios close to zero are observed at the nodes of the sinc^2 function suggests that this effect plays a minor role. Therefore, the decay mechanisms cannot explain the reduced peak height. This also justifies the fit using Eq. 3.1, which does not include any decay.

The non-unity peak height can be explained in another way. For the Rabi frequency of $\Omega_0 = 2\pi \times 21.4(3)$ Hz here found, the π-pulse duration is 23 ms. However, in the experiment a pulse duration of 15 ms was used. As seen in Fig. 3.1b, a pulse duration smaller than π/Ω_0 indeed has a non-unity peak height.

The measurement is performed several times with different clock beam intensities and pulse times, as shown in Figs. 3.7a through 3.7d. For decreasing intensity and increasing pulse time, the linewidth of the main peak decreases, as expected. Figure 3.7d shows the spectrum for an intensity of less than 0.3 mW/cm^2 and a clock pulse time of 34 ms. The maximum excitation reaches $n_e \approx 0.7$, again lower than expected for a π-pulse without other effects. The excitation fraction is fitted in the same way as before, and yields $\Omega_0 = 2\pi \times 8.5(7)$ Hz and a FWHM of 25 Hz.

Similar to before, the peak height does not reach one, and this is analogously explained by noting that the π-pulse duration for this Rabi frequency would be 59 ms, as opposed to the used 34 ms.

However, here the fit does not describe the data as well as for the higher intensity. The spin preparation did not change between these measurements, so cannot explain this effect. Spontaneous decay is still more than 20 times smaller than Ω_0, and decoherence still seems negligible, since the excitation fractions are close to zero between the peak and sinc lobes. Rather, the large fluctuations of n_e on the peak between detunings of -20 and 20 Hz suggest a different effect, namely non-linear drifts. For this high

resolution, the non-linear drifts only need to be a few Hz between two data points to give rise to large fluctuations. Non-linear drifts of a few Hz are realistic for our setup, which has been described in more detail in Refs. [129, 130]. This result is nonetheless significant, as the resolution of 25 Hz is the smallest that has ever been observed in a spectroscopy measurement with our system.

By comparing the resonance positions f_0 to the time between the two measurements (one hour), a residual linear drift of $\Delta\delta_{\text{drift}} = 0.028$ Hz/s is found. This is about $\Omega_0^2/(4\times 10^4)$ for the second measurement (and even smaller for the first). Comparing this to Fig. 3.3b, where drifts 10^4 times larger are plotted, this suggests that residual linear drifts do not significantly affect the spectra measured here.

Lastly, the measurements described here were done in a deep lattice, where the theory describes the excitation features well. Though at large s_{1D} the energy bands of the lattice are flat compared to the clock linewidth, for low 1D lattice depths this does not hold and the clock can excite momentum-selectively. This can be used to create synthetic dimensions and spin-orbit coupling [49]. Measurements similar to Ref. [49] were done with ^{171}Yb and described in Refs. [144, 171], but omitted here for brevity.

3.2.2   Rabi Oscillation Measurements

After having found the transition frequency, Rabi oscillations are performed. These are performed in much the same way as spectroscopy measurements as described in Sec. 3.2.1. The only difference is that the detuning is now fixed (ideally to resonance) and the clock pulse duration is varied.

This measurement starts with a Fermi gas of ^{173}Yb in the $m_F = 5/2$ state. A magnetic field of 8.8 G in the y-direction sets the quantisation axis as atoms are loaded into a lattice of depth $s_{\text{1D}} = 45E_{\text{r}}$ and $s_{\text{2D}} = 17E_{\text{r}}$.

Figure 3.8a shows the measured Rabi oscillations. These do not reach unity, though do not decay either, which can be caused by a non-zero detuning (see Fig. 3.1a) or by imperfect spin preparation, as discussed previously. Because these two effects cannot be distinguished in a Rabi oscillation measurement, a spectroscopy measurement was done directly afterwards, which is shown in Fig. 3.8b. Since here only the resonance position in comparison to the set frequency during the Rabi oscillation measurement matters, the data is fitted with the phenomenological function $p_1 \operatorname{sinc}^2(p_2(f - f_0))$, where p_1, p_2 and f_0 are free parameters. The resonance frequency f_0 is compared with the set frequency of the Rabi oscillation measurement and yields a difference of 92(6) Hz, which is used as the detuning during the Rabi oscillation measurement.

The Rabi oscillation is fitted with Eq. 3.1 and multiplied by a factor $n_{5/2}$ to account for the quality of the spin preparation, while keeping the detuning fixed to $\delta =$
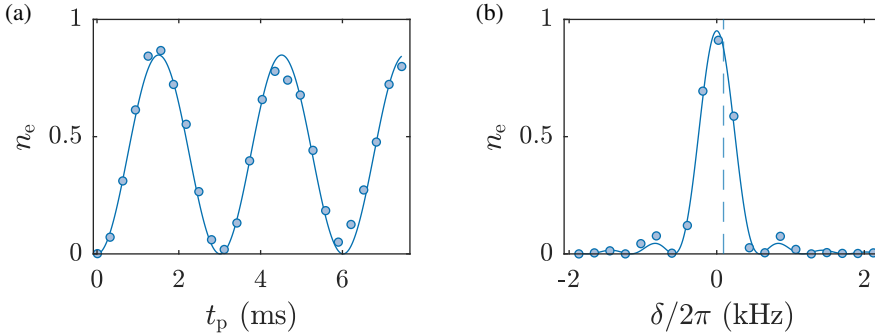
Figure 3.8: Rabi oscillations between the $|g\rangle$ and $|e\rangle$ state of a spin-polarised gas in a deep lattice ($s_{1D} = 45E_r$, $s_{2D} = 17E_r$). (a) Rabi oscillations where the points show the measured data and the solid line shows a fit (see text). The fit yields $\Omega_0 = 2\pi\times319(1)$ Hz and $n_{5/2} = 0.92(2)$ for $\delta = 2\pi\times92$ Hz (as obtained in the following spectrum). (b) Spectrum to measure the detuning at which the Rabi oscillations were done. A clock pulse duration of 1.55 ms was used. The points show the measured data, the solid line shows a fit (see text) and the dashed line shows the detuning at which the Rabi oscillation in (a) was measured, 92(6) Hz away from resonance.

$2\pi\times92$ Hz. The fit, shown in Fig. 3.8a, yields $\Omega_0 = 2\pi\times319(1)$ Hz and $n_{5/2} = 0.92(2)^*$, which is typical for our spin preparation of spin-polarised gases. The relative detuning $\delta \approx 0.3\Omega_0$ causes a maximum excitation of 0.93, which is similar to the effect of imperfect spin preparation. Therefore, both effects together explain why the Rabi oscillations do not reach unity in this measurement.

Further note that the fit describes the data well, especially for $t_p \lesssim 4$ ms. Deviations between the fit and the measured data slightly increase for larger times. For this data quality and these times, one cannot distinguish whether this is caused by a small residual linear drift, or by small decoherences, possibly due to the finite linewidth of the laser. However, the effect of spontaneous decay is ruled out, since the time scales in this measurement are about three orders of magnitude smaller than the lifetime of $|e\rangle$ atoms in a deep lattice (see Sec. 2.4.1). The spectrum confirms that decoherence does not play a large role in this measurement, since the excitation fraction comes to within a few percent of zero between the sinc lobes and the resonance peak. We further note

---

* An OSG measurement done directly after the Rabi oscillations and spectrum found that at least 89% of the atoms are in the $m_F = 5/2$ state, in good agreement with the fitted $n_{5/2}$. For general information on OSG, see Sec. 2.3.2, and for the analysis of OSG images, see Ref. [143].

that the clock pulse time of 1.55 ms that was used for the spectrum is within 1% of the ideal π-pulse time for the bare Rabi frequency found.

Lastly, these measurements were repeated for different m_F states of ^{173}Yb and yielded different bare Rabi frequencies since the different Clebsch-Gordan coefficients of the ^{1}S$_0(m_F) \rightarrow$ ^{3}P$_0(m_{F'})$ transitions lead to different coupling strengths. The data is presented in Ref. [143].

3.2.3   Measuring the Excitation Ratio

Finally, a measurement is done where the excitation fraction is observed as a function of both the clock pulse duration and the detuning, much like Fig. 3.2. A magnetic field of 2.7 G in the y-direction sets the quantisation axis and ^{173}Yb in the $m_F = 5/2$ state is loaded into a 'magic' lattice of depth $s_{1D} = 45E_r$ and $s_{2D} = 17E_r$ as described in Sec. 3.2.1. Here both the detuning δ and the pulse time t_p are varied, while keeping the bare Rabi frequency Ω_0 fixed. Figure 3.9a shows the measurement, where the colour shows the measured excitation fraction $n_{e,m}$, where the subscript 'm' indicates this is a measured quantity (as opposed to the fitted quantity later, denoted by 'f').

On resonance the excitation fraction goes through two maxima and two minima as a function of pulse time, as expected from Eq. 3.1. Further away from resonance, the excitation fraction oscillates faster as a function of pulse time, which is expected as the effective Rabi frequency increases, as discussed in Sec. 3.1.

Furthermore, around -900 Hz for $t \gtrsim 3.5$ ms the excitation ratio is larger than expected. This is attributed to a small remaining fraction of $m_F = -1/2$ state atoms. The differential Zeeman shift of ^{173}Yb is $\Delta m_F \times 113$ Hz/G [24, 172], so for the magnetic field of 2.7 G here used, $m_F = -1/2$ state atoms show up at approximately -900 Hz below the $m_F = 5/2$ resonance. Note that the $m_F = -1/2$ oscillations are not visible on these time scales, because the Clebsch-Gordan coefficient of this transition are smaller, resulting in smaller Rabi frequencies. We have performed a measurement with three different m_F states of ^{173}Yb where we observed these different Rabi frequencies, as described in Ref. [143].

As discussed for the Rabi oscillations in Sec. 3.2.2, a small remaining fraction of atoms in different m_F states reduces the maximum excitation on the $m_F = 5/2$ resonance, which is one of the reasons why the excitation fraction is never exactly one*. In addition, on this chosen detuning resolution we never precisely measure on

---

* To solve this, further blast pulses on the ^{1}S$_0 \rightarrow$^{3}P$_1$ transition after the DFG creation can remove unwanted m_F states, though this causes additional heating. These blast pulses are similar to the optical pumping pulses, except that at the lower trapping depths, atoms are removed from the system and do not decay back into the ground state.
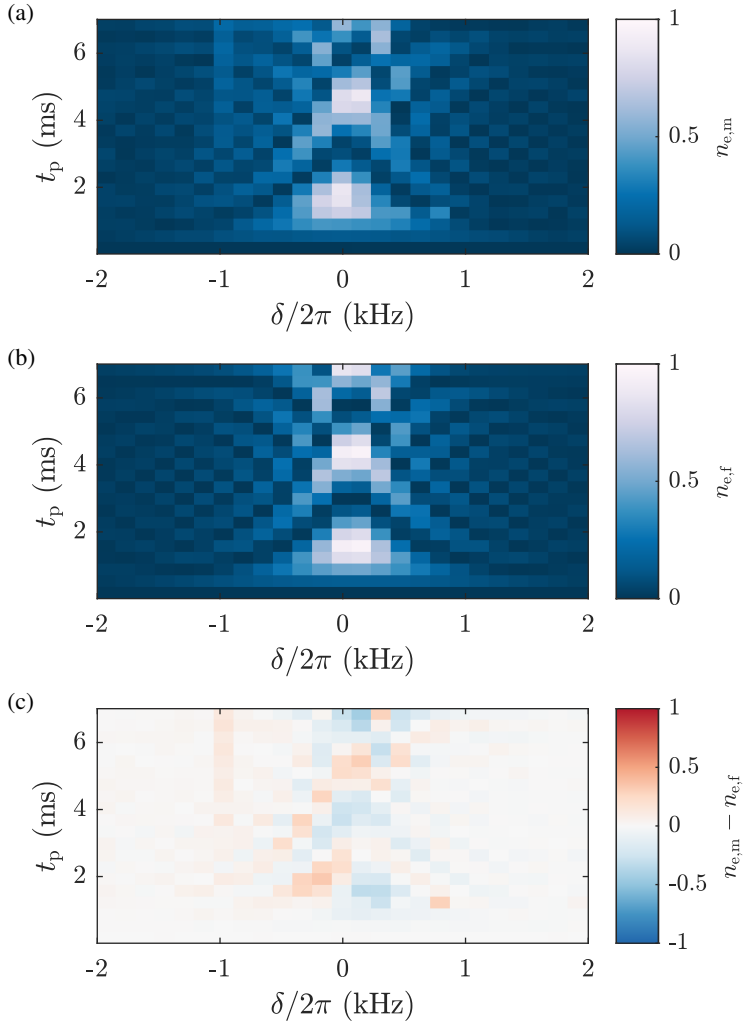
Figure 3.9: (a) Measurement of the excitation ratio $n_{e,m}$ of a spin-polarised sample of ^{173}Yb while varying the clock detuning δ and pulse time t_p. The data for $t_p \leq 1.06$ ms is taken twice and averaged, the data $t_p > 1.06$ ms is taken once. (b) Fit of the excitation ratio measurement in (a), where the fitted excitation fraction $n_{e,f}$ is plotted. The fit yields $\Omega_0 = 2\pi \times 328.0(8)$ Hz and the resonance position is used to centre all figures around $\delta = 0$. (c) Residuals of the fit $n_{e,m} - n_{e,f}$.

the resonance frequency. These effects, however, are only on the order of a few percent and do not prevent us from making a good fit to describe the data.

This two-dimensional fit is done using Eq. 3.1, where only the bare Rabi frequency Ω_0 and the resonance position f_0 are kept as free parameters. The fit is plotted in Fig. 3.9b and yields $\Omega_0 = 2\pi \times 328.0(8)$ Hz, indicating this is an accurate, albeit laborious, way of measuring the bare Rabi frequency. The fit also yields the resonance position, which is used to centre all three figures around $\delta = 0$. The checker-board-like pattern away from resonance is reproduced by the fit, which is also seen in the measurement, suggesting that this surprising effect is solely due to the chosen resolution of the pulse time and detuning.

The fit describes the measured data well as can be seen from comparing Fig. 3.9a and 3.9b. For a more accurate comparison, the residuals are calculated, which are the measured excitation ratio $n_{e,m}$ minus the fitted excitation ratio $n_{e,f}$ for each (δ, t_p), shown in Fig. 3.9c. Again, the extra excitation around $\delta \approx -900$ Hz is observed, as discussed previously. Additionally, the peak heights are slightly smaller than expected (light blue), which we attribute to a small remaining fraction of different m_F states. However, these are small effects and the two-level model describes our data well.

3.3   Conclusion

To conclude, the measurements of spin-polarised quantum gases can be explained well by a two-level description. The basic principles of Rabi oscillation measurements and spectra were explained, and the influence of linear frequency drifts and spontaneous decay and additional decoherence was studied. Since each effect has its characteristic features, this will prove useful in interpreting further Rabi oscillations and spectra.

This chapter forms the foundation of the following two chapters and the lessons learned will be used to interpret the upcoming measurements. In the following chapter this two-level description is applied to a two-body problem of ^{171}Yb which exhibits spin-exchanging interactions.

Chapter 4

Clock Spectroscopy of Spin-Exchanging Interactions

In the previous chapter, clock excitation of non-interacting spin-polarised gases was discussed within a two-level description. Here, this description is applied to interacting two-spin mixtures, giving rise to interorbital spin-exchanging interactions [2, 20–23, 155, 163, 173]. Due to the Pauli principle, the anti-symmetry of the two-atom wave function is either realised by the orbital part of the wave function or by the spin part of the wave function, characterised by two different s-wave scattering lengths $a_{eg^{\pm}}$ at ultracold temperatures, as described in detail in the following.

Measurements of interorbital spin-exchanging interactions with fermions in optical lattices started with ^{87}Sr [20] and ^{173}Yb [21, 22]. For both ^{87}Sr and ^{173}Yb the resulting spin-exchange interaction $V_{ex} \propto (a_{eg^+} - a_{eg^-})$ turned out to be ferromagnetic, i.e. $V_{ex} > 0$. Recent measurements of interorbital interactions on ^{171}Yb in the Kyoto group [23], the Munich group [155] and our group [2] showed an anti-ferromagnetic spin-exchange interaction. This makes ^{171}Yb a promising candidate for the quantum simulation of the anti-ferromagnetic Kondo-lattice model (KLM) [25, 31–34]. In this chapter, measurements on a two-spin gas of ^{171}Yb are presented. By measuring Rabi oscillations and high-resolution spectroscopy, we determine the s-wave scattering lengths and find a qualitative agreement with other recent measurements [23, 155].

This chapter is built up as follows. First, the theory of interorbital interactions in two-spin Fermi gases is described in terms of our observables. After that, the measurements of Rabi oscillations on these two-body systems are shown, followed by a spectroscopy measurement, yielding the s-wave scattering lengths. The chapter closes

with a conclusion and discussion on the relevance of these measurements.

The work in this chapter was supervised by K. Sengstock & C. Becker. The theory plots were made by the author. A first version of the measurement was performed and analysed by M. Diem, B. Abeln and the author. The final measurements presented in this chapter were taken by B. Abeln, M. Diem, N. Pintul and the author, and were analysed by B. Abeln and the author. The measurements presented in this chapter have been published in Ref. [2].

4.1   Interorbital Interactions in Fermi Gases

As described in Ch. 2, elastic on-site interactions of two fermions at low temperatures are characterised by a single s-wave scattering length a_{gg}. This changes for interorbital interactions since two scattering lengths are needed to describe the elastic on-site interactions, as described in the following. These two different scattering lengths give rise to a spin-exchange between atoms in the two orbitals.

Let us consider two ground-state atoms in a deep potential well. Due to the Pauli exclusion principle, the ground state atoms must have different spins. For ^{171}Yb, the two m_F states are the two spins, such that spin up $|\uparrow\rangle$ and down $|\downarrow\rangle$ denote $m_F = +1/2$ and $m_F = -1/2$, respectively. Since s-wave scattering interactions are symmetric, the states have a symmetric spatial wave function. The orbital part of the ground-ground state wave function can only be symmetric. Therefore, the anti-symmetry of the total wave function is provided by the spin wave function, such that the total state is given by $|gg\rangle \otimes (|\uparrow\downarrow\rangle - |\downarrow\uparrow\rangle) / \sqrt{2}$ (from here on, the spin part of this wave function will usually be omitted for brevity).

Now consider the single-photon $^1S_0 \rightarrow {}^3P_0$ transition with π^0-polarised light as in Ch. 3, at zero magnetic field. There are two possible resulting states that satisfy the fermionic anti-symmetrisation requirement: $|eg^+\rangle$ with a symmetric orbital wave function and anti-symmetric spin wave function, and $|eg^-\rangle$ with an anti-symmetric orbital wave function and symmetric spin wave function. In other words [2]

$$|eg^\pm\rangle = \frac{1}{\sqrt{2}} (|eg\rangle \pm |ge\rangle) \otimes \frac{1}{\sqrt{2}} (|\uparrow\downarrow\rangle \mp |\downarrow\uparrow\rangle), \tag{4.1}$$

which form the so-called interaction basis. These two states have Hubbard on-site energies $U_{eg^\pm} \propto a_{eg^\pm}$ (see Sec. 4.1.1), such that the interaction Hamiltonian $\hat{\mathcal{H}}$ can be rewritten as [127]

$$\hat{\mathcal{H}}(B = 0) = \begin{pmatrix} U_{eg^+} & 0 \\ 0 & U_{eg^-} \end{pmatrix}. \tag{4.2}$$

At non-zero magnetic field, the Zeeman interaction mixes the $|eg^+\rangle$ and $|eg^-\rangle$ states. The two eigenstates $|eg_{Z,1,2}\rangle$ of the Zeeman interaction are [127]

$$|eg_{Z,1}\rangle = \frac{1}{\sqrt{2}} (|e\uparrow, g\downarrow\rangle - |g\downarrow, e\uparrow\rangle) \tag{4.3}$$

$$|eg_{Z,2}\rangle = \frac{1}{\sqrt{2}} (|g\uparrow, e\downarrow\rangle - |e\downarrow, g\uparrow\rangle). \tag{4.4}$$

Note here that in this basis, each atom has a well-defined spin state, different from the eigenstates at zero magnetic field in Eq. 4.1. The Zeeman interaction therefore does not commute with the zero magnetic field Hamiltonian in Eq. 4.2 and mixes the $|eg^+\rangle$ and $|eg^-\rangle$ states at $B \neq 0$. The Zeeman basis can be rewritten in terms of the interaction basis by noting that $|eg_{Z,1,2}\rangle = (|eg^-\rangle \pm |eg^+\rangle)/\sqrt{2}^*$. Using this, the Zeeman interaction is included to obtain the Hamiltonian for all magnetic fields [127]

$$\hat{\mathcal{H}}(B) = \begin{pmatrix} U_{eg^+} & \alpha B \\ \alpha B & U_{eg^-} \end{pmatrix}, \tag{4.5}$$

where αB is the Zeeman energy and α is the differential Zeeman shift. This Hamiltonian has eigenenergies E_+ and E_- [2]

$$E_{\pm} = V_0 \pm V_{ex} \sqrt{1 + \left(\frac{\alpha B}{V_{ex}}\right)^2}, \tag{4.6}$$

where $V_0 = (U_{eg^+} + U_{eg^-})/2$ is the direct energy and $V_{ex} = (U_{eg^+} - U_{eg^-})/2$ is the spin-exchange energy. The eigenstates of the Hamiltonian are given by the $|+\rangle$ and $|-\rangle$ states [2]

$$|+\rangle = c_1(B)|eg^+\rangle + c_2(B)|eg^-\rangle \tag{4.7}$$

$$|-\rangle = -c_2(B)|eg^+\rangle + c_1(B)|eg^-\rangle, \tag{4.8}$$

---

* Comparing the interaction and Zeeman basis, we can now understand why the resulting interaction is called *spin-exchanging*. If one prepares a system in, for instance, the Zeeman basis at large $|\alpha B/V_{ex}| \gg 1$ and quenches the magnetic field to small $|\alpha B/V_{ex}| \ll 1$, the Zeeman basis is projected on the interaction basis. Due to the energy difference of the states, an oscillation in magnetisation starts with a frequency related to $|V_{ex}|$. This is exactly what the Florence group has done, where they observed oscillations in the magnetisation of ground state ^{173}Yb after a quench of the magnetic field [22].
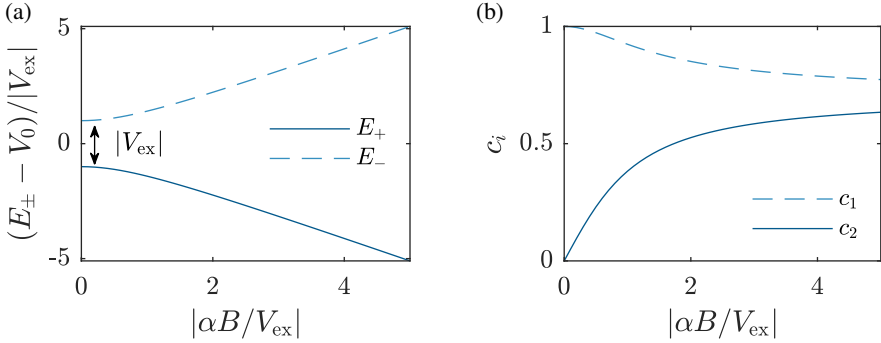
Figure 4.1: Energy of the $|+\rangle$ and $|-\rangle$ states and mixing coefficients. (a) shows the dimensionless energy as a function of dimensionless magnetic field, assuming a negative V_{ex}. For a positive V_{ex} the role of the E_+ and E_- branches is reversed. The solid and dashed lines indicate the energy of the $|+\rangle$ and $|-\rangle$ states, respectively. (b) shows the mixing coefficients $c_{1,2}$ as a function of dimensionless magnetic field. The dashed and solid lines indicate the c_1 and c_2 coefficients, respectively.

where c_1 and c_2 are the mixing coefficients [2]

$$c_1(B) \quad = \quad \frac{|V_{ex}| + \sqrt{V_{ex}^2 + (\alpha B)^2}}{\sqrt{2V_{ex}^2 + 2(\alpha B)^2 + 2|V_{ex}|\sqrt{V_{ex}^2 + (\alpha B)^2}}} \qquad (4.9)$$

$$c_2(B) \quad = \quad \frac{|\alpha B|}{\sqrt{2V_{ex}^2 + 2(\alpha B)^2 + 2|V_{ex}|\sqrt{V_{ex}^2 + (\alpha B)^2}}}. \qquad (4.10)$$

Figure. 4.1a shows the energies in terms of the dimensionless magnetic field. At $B = 0$, the $|+\rangle$ and $|-\rangle$ states are separated by an energy of V_{ex}. For increasing magnetic field, the $|+\rangle$ and $|-\rangle$ states become indistinguishable from the Zeeman states (see Eqs. 4.3 and 4.4), and the energy correspondingly becomes linear in B as the Zeeman interaction becomes the dominant energy scale of the Hamiltonian. In Fig. 4.1a, V_{ex} was assumed to be negative. For a positive V_{ex} the role of the E_+ and E_- branches is reversed. Further note that $E_\pm$ are centred around the direct interaction V_0.

Light which is π^0-polarised only couples the $|gg\rangle$ state with the $|eg^-\rangle$ state, because the Clebsch-Gordan coefficients of the $|gg\rangle \to |eg^+\rangle$ transition cancel each other out, preventing this transition [127]. Since the Zeeman interaction admixes both $|eg^\pm\rangle$ states, the coupling of $|+\rangle$ and $|-\rangle$ to the initial $|gg\rangle$ state depends on the mixing coef-

ficients c_2 and c_1, respectively, which are shown in Fig. 4.1b*. In other words, the $|+\rangle$ and $|-\rangle$ states can only be exited in so far as they include the $|eg^-\rangle$ state. The coupling is given by [127]

$$\hat{\mathcal{H}} = \sqrt{2}c_2(B)\frac{\hbar\Omega_0}{2}|+\rangle\langle gg| + \sqrt{2}c_1(B)\frac{\hbar\Omega_0}{2}|-\rangle\langle gg| \tag{4.11}$$

$$= \frac{\hbar\Omega_+}{2}|+\rangle\langle gg| + \frac{\hbar\Omega_-}{2}|-\rangle\langle gg|, \tag{4.12}$$

where the Rabi frequencies of the $|\pm\rangle$ states $\Omega_\pm$ are rewritten as [2]

$$\Omega_\pm(B) = \sqrt{2}\,c_{2,1}(B)\,\Omega_0, \tag{4.13}$$

where Ω_0 is the bare Rabi frequency of the one-body transition.

Two limiting cases are insightful to consider. At $B = 0$, the Rabi frequency Ω_+ connecting $|gg\rangle$ to $|+\rangle$ is zero, since here $|+\rangle = |eg^+\rangle$, which is not coupled to $|gg\rangle$ for π^0-polarised light. At the same time, the Rabi frequency of the $|-\rangle$ state is $\sqrt{2}\Omega_0$. For $|\alpha B| \gg |V_{\text{ex}}|$ both mixing coefficients approach $1/\sqrt{2}$ and the coupling becomes equal to the one-body coupling $\Omega_\pm \rightarrow \Omega_0$. This can be understood as follows. In the Zeeman regime, the $|+\rangle$ and $|-\rangle$ states approach the Zeeman basis (see Eqs. 4.3 and 4.4), where both atoms have a well-defined spin and only one of the two atoms is excited with the normal one-body coupling.

Lastly, note that c_1 and c_2 do not depend on the sign of the spin-exchange interaction, as opposed to the energies $E_\pm$. Measuring the Rabi frequencies thus enables identifying the $|+\rangle$ and $|-\rangle$ states.

4.1.1 Elastic Two-Body Interactions

In the previous section, the energies and the eigenstates of the system were explained. The quantities of interest are the Hubbard on-site interactions U_{eg^+} and U_{eg^-}. In general, the elastic on-site interaction of atoms 1 and 2 is related to the scattering length a_{12} as [2]

$$U_{12}(s_{1D}, s_{2D}) = \frac{4\pi\hbar^2}{2\mu}a_{12}\int d\mathbf{r}\,|w_0(\mathbf{r}, s_{1D}, s_{2D})|^4, \tag{4.14}$$

where μ is the reduced mass of the interacting pair, w_0 is the single-particle Wannier function, $\mathbf{r}$ is the position vector and s_{1D} and s_{2D} are the 1D and 2D lattice depths. Here the assumptions are that both atoms are subject to the same Wannier function, and that the interaction shift is small in comparison to the spacing to the second lattice band

---

* Note that at zero magnetic field $c_1 = 1$ and $c_2 = 0$, such that there $|\pm\rangle = |eg^\pm\rangle$.
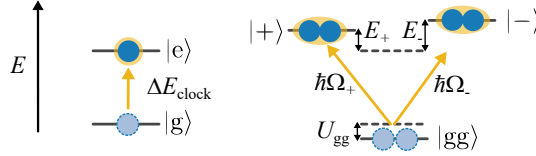
Figure 4.2: Energy scheme of (left) the clock excitation of single atoms in comparison to (right) clock excitation of two atoms, excited to the interorbital states $|+\rangle$ and $|-\rangle$ (not to scale). Atoms are depicted as blue disks and single-photon transitions are depicted by the yellow arrows. The solid horizontal lines show the energies of each state, which are denoted by the kets. The dashed horizontal lines show the energy of the single-atom ground and excited states, from bottom to top.

(the blue sideband). Applied to interorbital interactions in ^{171}Yb, these assumptions are justified since $|e\rangle$ and $|g\rangle$ atoms are subject to the same potential at the 'magic' wavelength, and since the interaction shifts are about ten times smaller than those of the blue sideband (see Sec. 4.2.2). Measuring the lattice depths and interaction energies thus yields the scattering lengths $a_{eg^{\pm}}$ and this will be done in the following.

4.2 Measuring Interorbital Interactions of ^{171}Yb

In clock-spectroscopy experiments, one can only measure energy differences. In the case of spin-exchanging interorbital interactions, the energy of the $|+\rangle$ and $|-\rangle$ states are measured with respect to the $|gg\rangle$ state. The $|gg\rangle$ state has an s-wave scattering length of $a_{gg} = -3(4)a_0$ [86]. Compared to a single $|g\rangle$ atom in the lattice, the $|gg\rangle$ state thus has an energy of U_{gg}. Similarly, the $|\pm\rangle$ states have an energy of $E_{\pm}(B)$ with respect to the single $|e\rangle$ atom energy. Hence, in a spectroscopy measurement the $|\pm\rangle$ states are measured at energy shifts $\Delta E_{\pm} = E_{\pm} - U_{gg}$ with respect to the single-body $^1S_0 \rightarrow {}^3P_0$ resonance, where Δ denotes the quantity is measured with respect to the ground-ground state interaction. The relevant energy levels[*] are depicted in Fig. 4.2.

In order to measure the scattering lengths, we perform spectroscopy measurements on a two-spin ^{171}Yb gas in a lattice with some fraction of the atoms on doubly-occupied sites. For high-precision spectroscopic measurements, one needs to set the clock pulse time close to a π-pulse, so that the excitation fraction is maximum. However, as seen

---

[*] Atoms in the $|\pm\rangle$ states can also be excited to the $|ee\rangle \otimes (|\uparrow\downarrow\rangle - |\downarrow\uparrow\rangle)/\sqrt{2}$ state since the π^0-polarised clock light couples $|eg^-\rangle$ to $|ee\rangle$, which was done by Ref. [155]. The $|ee\rangle$ state is ommited from the figure and our measurements.

the Rabi couplings of the $|+\rangle$ and $|-\rangle$ states depend on the magnetic field and the un-known spin-exchange energy (see Fig. 4.1b and Eq. 4.13). To overcome this, we do the following.

1. We perform a spectroscopy measurement at several magnetic fields using the π-pulse time of the single-atom transition Ω_0. In this way we find the resonance positions of the single-atom transitions and of the $|+\rangle$ and $|-\rangle$ states, since using a non-π-pulse for spectroscopy changes the width and height, but not the resonance position (see Sec. 3.1).

2. Using the resonance positions at the used magnetic fields, we perform Rabi os-cillations to find the π-pulse times of the $|+\rangle$ and $|-\rangle$ states, as described in the following.

3. Using the appropriate pulse time per peak, we repeat the spectroscopy measure-ment at six magnetic fields and identify the peaks, as presented in Sec. 4.2.2.

4.2.1 Measuring Rabi Oscillations of ^{171}Yb

Using the resonance positions of the $|+\rangle$ and $|-\rangle$ states found in a spectroscopic mea-surement using the single-atom pulse time, we measure the Rabi oscillations on the interorbital interaction resonances. In this way, we determine the correct pulse time and identify the spectroscopic peaks. To do this, a gas of about 3×10^4 atoms is loaded into a lattice of depths $s_{1D} = 50(2)E_r$ and $s_{2D} = 25.0(3)E_r$ and Rabi oscillations are performed as described in Sec. 3.2.1. We repeat the Rabi oscillation measurement for magnetic fields of 1.8 G, 3.5 G, 8.8 G and 17.5 G.

Figure 4.3 shows the Rabi oscillations for the two interaction resonances at different magnetic fields, where (a) through (d) are taken at one resonance and (e) through (g) at the other resonance. The former has a larger oscillation frequency, which we therefore identify as the $|-\rangle$ state (compare Eq. 4.13 and Fig. 4.1b). The states are indicated in the upper left corner.

The Rabi oscillations in Fig. 4.3 are fitted to verify the magnetic-field dependence of the Rabi frequencies (compare Eq. 4.13). However, Eq. 3.1 cannot be used due to the significant decay observed. The excitation fraction does not reach zero for $t_p > 0$ and the second peak is lower than the first, which linear frequency drifts (see Sec. 3.1.1) or off-resonant probe frequencies (see Sec. 3.1) cannot explain. Therefore, a description with the optical Bloch equations is needed (see Sec. 3.1.2), which can explain these dampings (compare Fig. 3.4). To this end, a fit was made using the numeric solutions of the optical Bloch equations, using δ, Ω_0 and Γ_c as free parameters. Spontaneous decay of the excited state is neglected because of the short timescales of the Rabi oscillations
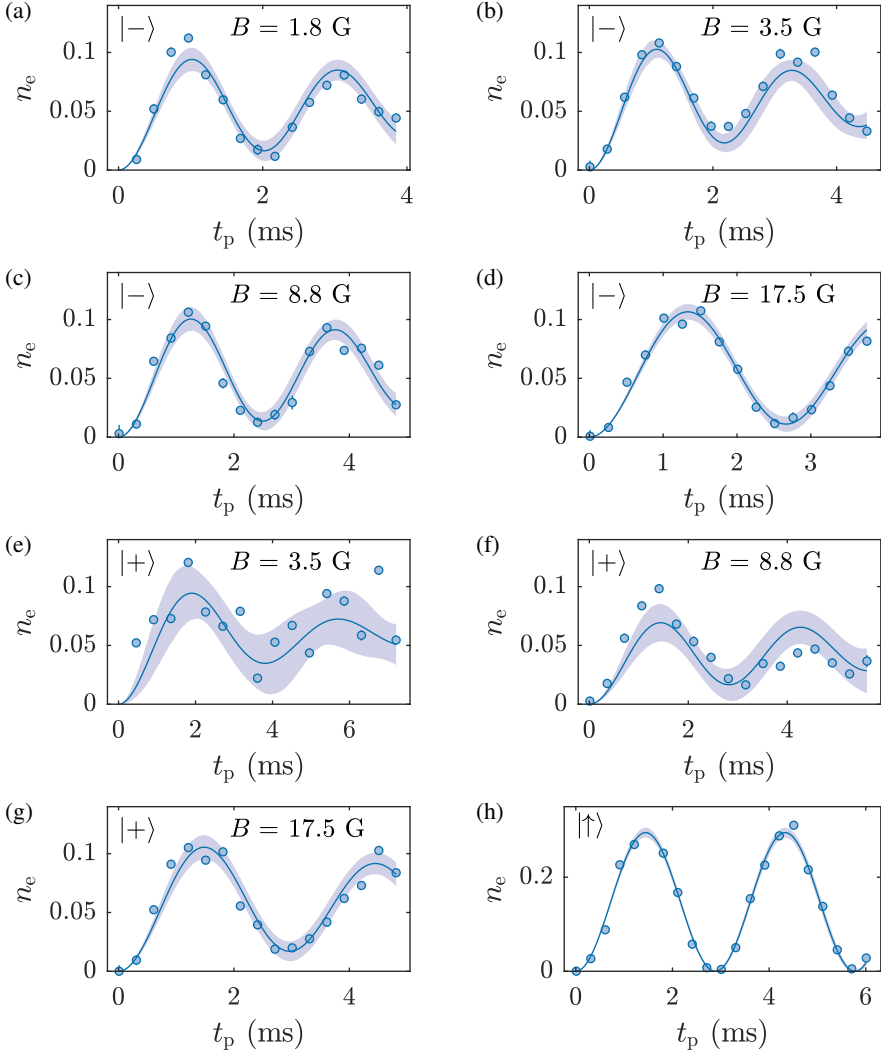
Figure 4.3: Rabi oscillations of the $|+\rangle$ and $|-\rangle$ states of ^{171}Yb. The data is two to three times averaged per pulse time and the error bars denote one standard deviation. The solid line shows a fit using the optical Bloch equations (see text) and the shaded area shows its 95% confidence interval. (a) - (d) show Rabi oscillations at the $|-\rangle$ state transition and (e) - (g) show Rabi oscillations at the $|+\rangle$ state transition for different magnetic fields. (h) shows Rabi oscillations of the $|\uparrow\rangle$ single-atom state at $B = 17.5$ G.

in comparison to the lifetimes of several seconds of the $|\pm\rangle$ states in a $35E_r$ lattice measured by Ref. [155]. Since the maximum excitation ratio is limited by the ratio of doubly-occupied sites in the lattice, the maximum excitation ratio of the fit is limited to $n_e = 0.115(4)$, which was found in the spectroscopy measurement as described in Sec. 4.2.2*. The data of Fig. 4.3e and 4.3f show a larger scatter, which we attribute to fluctuations in the atom number and non-linear drifts. In all other measurements presented in Fig. 4.3, the fits describe the data well.

Further, Rabi oscillations of the $|\uparrow\rangle$ single atom peak were measured to accurately determine Ω_0 and enable comparison with $\Omega_{\pm}$. A ^{171}Yb spin-mixture was used at $B = 17.5$ G to ensure no peaks overlap with the single-atom $^1S_0(m_F = 1/2) \rightarrow ^3P_0(m_{F'} = 1/2)$ resonance. The resulting Rabi oscillations are shown in Fig. 4.3h. The fit is made using Eq. 3.1 and a maximum excitation of 0.297(6) as obtained from the spectroscopy measurement (see Sec. 4.2.2). This fit yields a bare Rabi frequency of $\Omega_0 = 345(3)$ Hz and a detuning of $\delta < \Omega_0/10$. Note that, analogously to the single-atom Rabi oscillations in Sec. 3.2.2, the fit function without decays describes the data well.

Figure 4.4 shows the bare Rabi frequencies for the two interacting states per magnetic field $\Omega_{\pm}(B)$. The solid lines show the expected $\Omega_{\pm}$ based on Eq. 4.13, the value of ΔV_{ex} as measured in the following spectroscopy measurement (see Sec. 4.2.2 and 4.2.3) and the Rabi frequency of the single-atom transition. The measured Rabi frequencies of the $|+\rangle$ and $|-\rangle$ states agree well with the expectation and the general functionallity is reproduced.

From Fig. 4.3 we further determined the additional decoherence rate Γ_c (see Sec. 3.1.2) per state and per magnetic field. The decoherence rates found in this way seem to be independent of magnetic field, and for the $|+\rangle$ and $|-\rangle$ states we find average values of $\Gamma_{c+} = 2\pi \times 34(5)$ Hz and $\Gamma_{c-} = 2\pi \times 32(8)$ Hz, respectively. This suggests that the decoherence is independent of the state, within the experimental accuracy. The decay rates correspond to coherence lifetimes of about 30 ms. The source of this decoherence is currently not established, but it is expected to be caused by interactions which do not change the excitation fraction. This statement is supported by the observation that single-atom Rabi oscillations (see Fig. 4.3h) are not affected by decoherence on experimentally relevant time scales.

---

*The fraction of atoms on doubly-occupied sites is of course twice as large, since only one atom of the pair is excited on this interorbital interaction measurement.
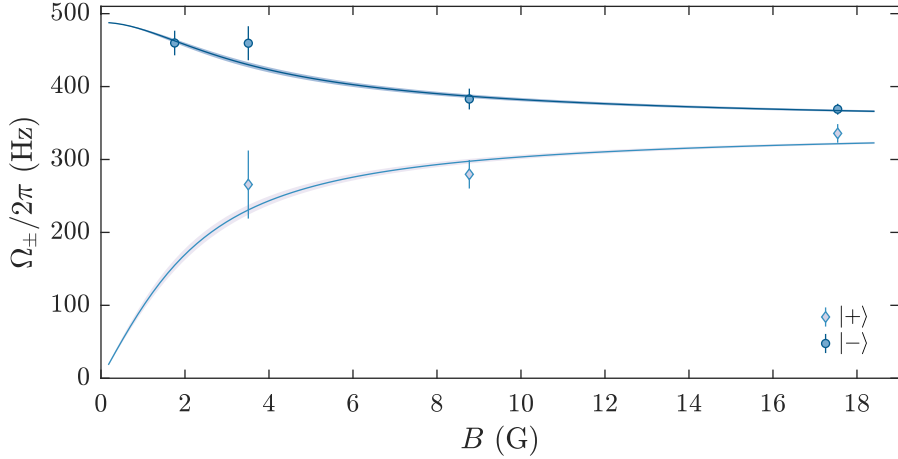
Figure 4.4: Measured Rabi frequencies $\Omega_\pm$ of the $|\pm\rangle$ states as a function of magnetic field. The data points show the Rabi frequencies and the error bars show the error of the fits. The solid lines are the expected curves using Eq. 4.13, the single-atom Rabi frequency $\Omega_0 = 2\pi \times 345(3)$ Hz, and ΔV_{ex} as measured in the spectroscopy measurement (see Sec. 4.2.2), and the shaded area shows the 95% confidence interval of the expected curve. The figure is adapted from the published version [2]. © 2021 American Physical Society.

4.2.2 Spectroscopy Measurement of ^{171}Yb

Having found the Rabi frequencies, we perform spectroscopy at six magnetic fields to measure the interaction shifts $\Delta E_\pm$. To this end, a spin-balanced ^{171}Yb gas of 1.5×10^4 to 3.5×10^4 atoms is loaded into a 'magic' lattice of depth $s_{1D} = 50(2)E_r$, $s_{2D} = 25.0(3)E_r$. From the peak resonances found in the first spectroscopy measurement, we choose detuning intervals with 15 data points per peak. Using a constant clock beam intensity like in Sec. 4.2.1, we set the illumination time to be a π-pulse for each specific peak, using either the single-atom Rabi frequency or the Rabi frequencies of the $|+\rangle$ and $|-\rangle$ states as obtained in the previous section*. This enables us to get the best-achievable peak heights with our setup, increasing the signal-to-noise.

Figure 4.5 shows the resulting spectra, where several peaks are observed. In Fig. 4.5b through 4.5f, the two highest peaks are the single atom resonances, which overlap at

---

* The Fourier-limited widths of the single-atom and interaction peaks are therefore different and the interaction peak widths further vary per spectrum.
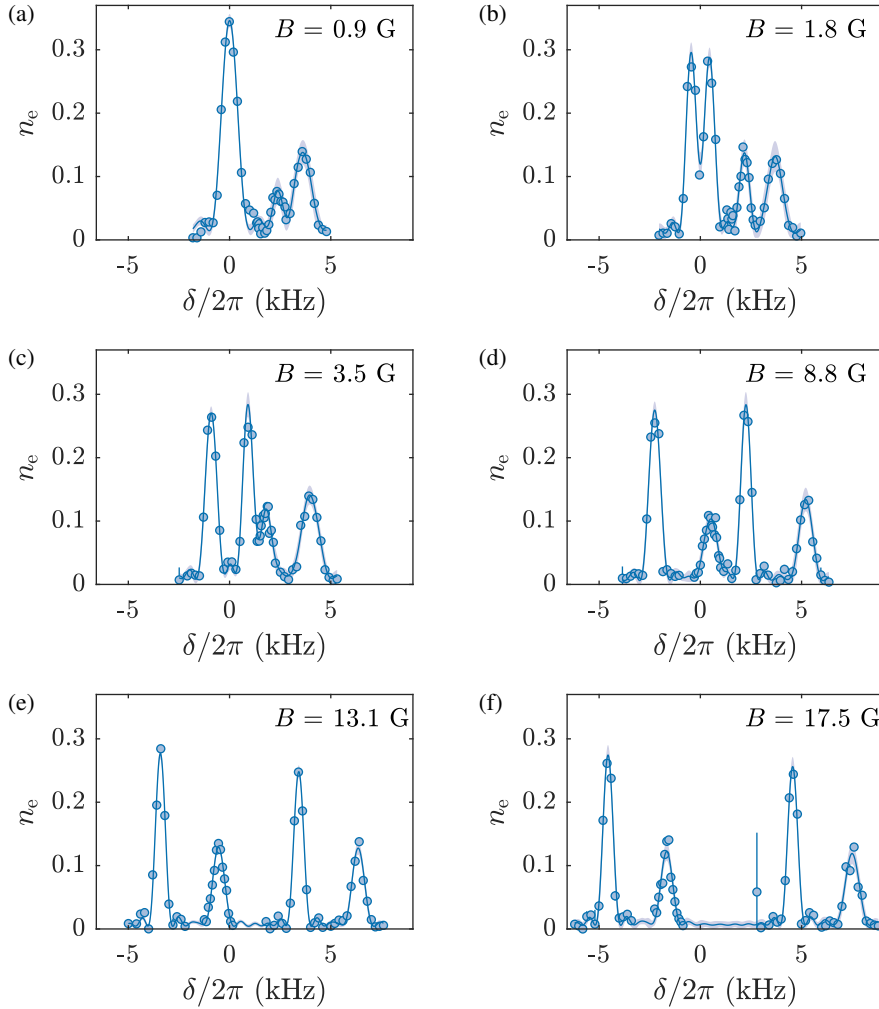
Figure 4.5: Spectra of the interorbital interaction measurement in ^{171}Yb for six different magnetic fields. The data points are the measured excitation fractions and are three times averaged. The error bars represent the propagated errors in the atom number estimation. The solid lines show a multi-sinc^2 fit (see text) and the shaded areas show the 95% confidence interval. (a) through (f) show the spectra at magnetic fields of 0.9 G, 1.8 G, 3.5 G, 8.8 G, 13.1 G and 17.5 G, respectively. For the identification of the peaks, see text and Fig. 4.6. The figure is adapted from the published version [2]. © 2021 American Physical Society.

$B = 0.9\,\text{G}$ in Fig. 4.5a. Due to the negative differential Zeeman shift $\alpha = -399.1\,m_F\,\text{Hz/G}$ [155], the left and right peaks are identified as $|\uparrow\rangle$ and $|\downarrow\rangle$, respectively. The fact that the amplitude of the two single-atom peaks is essentially the same, confirms that the initial sample is spin-balanced to within a few percent. The two peaks with the lowest amplitude are the interorbital interaction resonances, which were identified in the Rabi oscillation measurement. Considering these two low-amplitude peaks, the peaks on the left and right are identified as the $|+\rangle$ and $|-\rangle$ states, respectively. Similar to the singles peaks, the height of the interorbital interaction peaks is almost constant, suggesting that we reliably excite all interacting atoms. The cause of the remaining small deviations in heights is unknown, but could be due to fluctuations in the atom number or temperature. Considering all the peak heights, we conclude that the lattice is mostly filled with single atoms, with approximately 25% of the atoms on doubly occupied sites (see
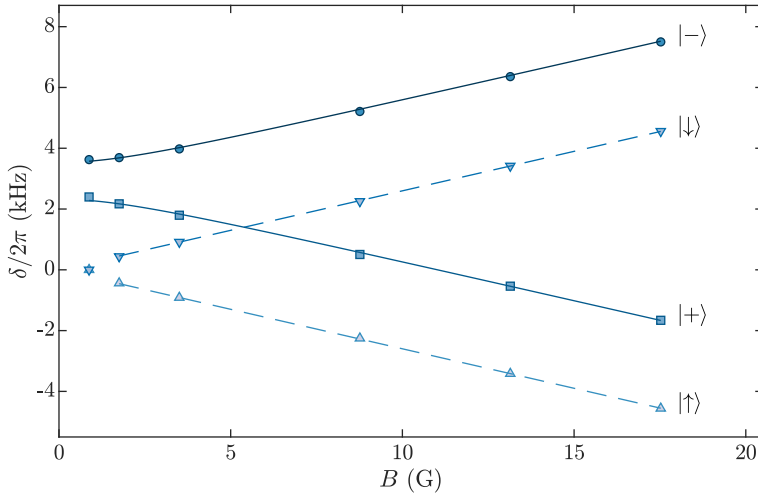
Figure 4.6: Frequency of the peaks as function of magnetic field. The data points show the peak positions as obtained from fits to the spectra in Fig. 4.5 and are identified on the right. The error bars are smaller than the marker size. The dashed lines show the energies of the $|\uparrow\rangle$ and $|\downarrow\rangle$ states based on the Zeeman energy αB with $\alpha = -399.1\,m_F\,\text{Hz/G}$ [155]. The solid lines show the energies of the $|\pm\rangle$ states based on Eq. 4.6 and the ΔV_0 and ΔV_{eg} we found (see text). The figure is adapted from the published version [2]. © 2021 American Physical Society.

Sec. 4.2.3).

Next, the spectra are fitted with four sinc^2 functions (three for $B = 0.9$ G since the two single atom peaks overlap). In this way, the resonance positions are obtained accurately for all peaks. The middle of the single atom peaks is used to centre the detuning. Hence, $\delta = 0$ indicates the degenerate $B = 0$ resonance of the single atoms. Furthermore, the splitting of the $|\uparrow\rangle$ and $|\downarrow\rangle$ states is used to calibrate the magnetic field, using the accurate determination of the differential Zeeman splitting by Ref. [155].

Figure 4.6 shows the peak frequencies as obtained from the sinc^2 fits as a function of the magnetic field. The single atom peaks show the expected linear dependence on B (dashed lines), whereas the interorbital interaction peaks show the expected square-root dependence on B (solid lines, compare Fig. 4.1a). The curves are obtained by analysing the peak positions and obtaining the quantities of interest, yielding $a_{\text{eg}^+} = 201(5)a_0$ and $a_{\text{eg}^-} = 306(6)a_0$ and $\Delta V_{\text{ex}}/h = -0.60(2)$ kHz, as explained in the following.

4.2.3 Determination of $a_{\text{eg}^\pm}$

In principle, the $|+\rangle$ and $|-\rangle$ peak data as presented in Fig. 4.6 can simply be fitted using Eq. 4.6 to find the scattering lengths. However, several problems surface in this approach. First, the zero-point detuning, in other words the centre of the $|\uparrow\rangle$ and $|\downarrow\rangle$ peaks, has some uncertainty, which differs per magnetic field, which must be included in fitting the energies $\Delta E_\pm$ *. Second, all peak positions are correlated, since all come from a single multi-sinc^2 fit. If one fits the $|+\rangle$ peaks with the ΔE_+ function and the $|-\rangle$ peaks with the ΔE_- function, the resulting ΔV_0 and ΔV_{ex} are correlated. It is not trivial to include these correlations in the subsequent error calculation. To avoid these issues, another method is used. For this, let us take a step back and reconsider what was measured.

In our experiments, we measure frequencies of the clock laser. We call the different resonant clock laser frequencies f_i where $i \in [1, 4]$, which consecutively represent the $|+\rangle$, $|-\rangle$, $|\uparrow\rangle$ and $|\downarrow\rangle$ states. Using Eq. 4.6 and the Zeeman energy, these frequencies can be related to the energies as

$$hf_1(B) = \Delta E_+(B) + A = \Delta V_0 - \sqrt{(\Delta V_{\text{ex}})^2 + (\alpha B)^2} + A \quad (4.15)$$

$$hf_2(B) = \Delta E_-(B) + A = \Delta V_0 + \sqrt{(\Delta V_{\text{ex}})^2 + (\alpha B)^2} + A \quad (4.16)$$

$$hf_3(B) = E_\uparrow(B) + A = -|\alpha|B + A \quad (4.17)$$

$$hf_4(B) = E_\downarrow(B) + A = |\alpha|B + A, \quad (4.18)$$

---

* Recall that all energies are measured with respect to the ground-ground state energy, which is denoted by Δ. See also Sec. 4.2.

where h is Planck's constant and A is some unknown offset energy. Here we have extracted the sign out of the Zeeman energy of the $|\uparrow\rangle$ and $|\downarrow\rangle$ states*, and we used the fact that ΔV_{ex} is negative (compare Eq. 4.6).

Now, to avoid the problems mentioned previously, these equations are rewritten such that each quantity of interest is given in terms of the measured quantities f_i, and the error propagation is performed including the correlations between all f_i. In this way, the offset frequency per magnetic field is found using $A/h = (f_3 + f_4)/2$. Similarly, the magnetic field calibration is found by considering $(f_4 - f_3)/2$. The spin-exchange energy ΔV_{ex} and direct interaction energy ΔV_0 can then be found using

$$\Delta V_{\mathrm{ex}}/h = -\sqrt{(f_1 - f_2)^2 - (f_4 - f_3)^2}/2 \tag{4.19}$$
$$\Delta V_0/h = (f_1 + f_2 - f_3 - f_4)/2. \tag{4.20}$$

As seen, all f_i are dependent on the magnetic field. In this treatment, the dependence on B cancels out, and yields the quantities ΔV_{ex} and ΔV_0 independent of magnetic field. Hence a simple weighted mean over all magnetic fields is used to find the best estimates of the quantities of interest.

Figure 4.7 shows the spin-exchange and direct-interaction energies found with this method. As expected, ΔV_{ex} fluctuates around a mean value and does not depend on the magnetic field. Notably, the error bars of ΔV_{ex} increase for increasing magnetic field. This is not because the peak positions are less accurate at higher magnetic fields, but because of the form of ΔV_{ex} in terms of all f_i. At large magnetic fields $\alpha B/\Delta V_{\mathrm{ex}} \gg 1$ we note that $\Delta E_\pm$ is barely affected by the spin-exchange interaction and in the limit becomes $\Delta E_\pm(B \to \infty) = \Delta V_0 \mp |\alpha B|$ (see Eq. 4.6). This also explains why the error bars of ΔV_0 do not increase for increasing magnetic field. The origin of the residual deviations is unknown, but might be explained by non-linear drifts in the clock laser cavity.

The best estimates of the spin-exchange and direct interactions are found simply using a weighted mean, yielding $\Delta V_{\mathrm{ex}}/h = -0.60(2)$ kHz and $\Delta V_0/h = 2.896(11)$ kHz, which are specific for our geometry and lattice depths. Using Eq. 4.14 with the lattice depths $s_{\mathrm{1D}} = 50(2)E_{\mathrm{r}}$ and $s_{\mathrm{2D}} = 25.0(3)E_{\mathrm{r}}$, and $a_{\mathrm{gg}} = -3(4)a_0$ [86], this yields the scattering length of the direct interaction $a_{\mathrm{eg0}} = 253(5)a_0$.

Similar to ΔV_{ex} and ΔV_0, the $\Delta U_{\mathrm{eg}\pm}$ are found in terms of the measured quantities

$$\Delta U_{\mathrm{eg}\pm}/h = \left(f_1 + f_2 - f_3 - f_4 \mp \sqrt{(f_1 - f_2)^2 - (f_4 - f_3)^2}\right)/2. \tag{4.21}$$

Figure 4.8a shows $\Delta U_{\mathrm{eg}\pm}$ as a function of magnetic field. Some fluctuations are observed, but the weighted means generally describe the data well. The averages over the

---

* Note that in this representation, as before, α still includes the m_F dependency.
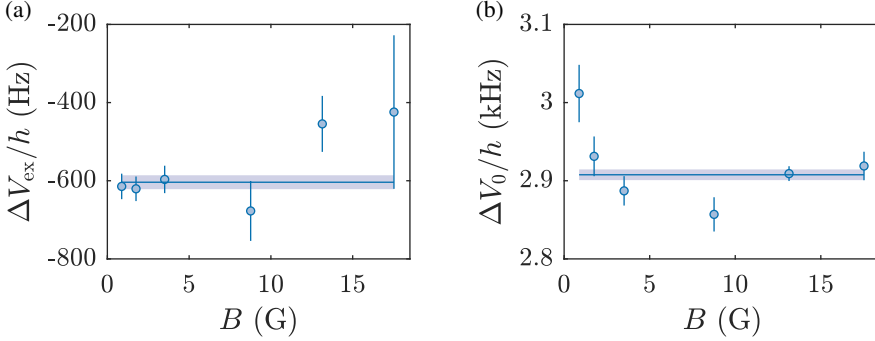
Figure 4.7: Measured interaction frequencies of the ^{171}Yb spin-exchange interaction. The data points show the interaction frequencies and the error bars show the propagated errors. The solid lines show the weighted mean of the fit and the shaded areas show the 95% confidence intervals. For the determination strategy, see text. (a) shows spin-exchange interaction as a function of magnetic field and (b) shows the direct interaction as a function of magnetic field. The fits yields $\Delta V_{ex}/h = -0.60(2)$ kHz and $\Delta V_0/h = 2.896(11)$ kHz, respectively.

magnetic fields yield $\Delta U_{eg^+}/h = 2.30(3)$ kHz and $\Delta U_{eg^-}/h = 3.50(3)$ kHz. In the same way as for the direct interaction, the scattering lengths are found using Eq. 4.14 with the lattice depths $s_{1D} = 50(2)E_r$ and $s_{2D} = 25.0(3)E_r$, and $a_{gg} = -3(4)a_0$ [86]. We thus find $a_{eg^+} = 201(5)a_0$ and $a_{eg^-} = 306(6)a_0$.

Lastly, by analysing the interaction-peak amplitudes $n_\pm$ of the $|\pm\rangle$ states we find the fraction of atoms on doubly-occupied sites (doublons). Since only one of both interacting atoms is excited, the doublon fraction is twice as large as the peak amplitude. Furthermore, the initial $|gg\rangle$ state is independent of the final state, so the doublon fraction is $2n_+ = 2n_- = n_+ + n_-$. Figure 4.8b shows interaction-peak amplitudes per magnetic field, denoted by n_+ and n_-. Except for $B = 0.9$ G, we observe a fairly constant double occupancy. We find an average doublon fraction of $n_+ + n_- = 0.230(8)$, which was used in Sec. 4.2.1 to set the maximum excitation fraction.

However, note that this is a lower limit of the doublon fraction, since decoherence causes the peak height to decrease (see Sec. 3.1.2 and Fig. 3.5b). Furthermore, one can now understand why the $|+\rangle$ peak is typically smaller than the $|-\rangle$ peak for $B < 10$ G. As described in Sec. 4.2.1 the decoherence rate is approximately the same for all magnetic fields and both states. However, the Rabi frequency changes as a function of B (see Fig. 4.4). For smaller magnetic fields, the Rabi frequency of the $|+\rangle$ state is com-
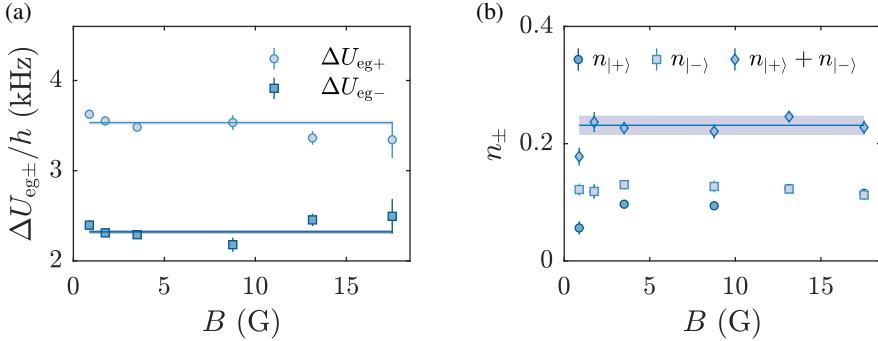
Figure 4.8: Measured interaction shifts of the $|eg^\pm\rangle$ states and fraction of doubly-occupied sites. The points show the measured data with the error bars the propagated standard errors. The solid lines show the weighted mean and the shaded area shows the 95% confidence interval. For the determination strategy, see text. (a) shows $\Delta U_{eg^\pm}/h$ as a function of magnetic field and (b) shows the fraction of doubly-occupied sites for the $|\pm\rangle$ states and its sum (see legend). We find an average double occupancy of 0.230(8).

paretively small, and since $\Gamma_{c^\pm}$ is independent of B (see Sec. 4.2.1), the relative decoherence Γ_c/Ω_+ is comparatively large. Therefore, decoherence decreases n_+ especially for smaller magnetic fields. In other words, at small B the $|+\rangle$ state requires relatively long π-pulse times and therefore decoherence reduces the maximum excitation more than it does for shorter π-pulse times.

4.3   Conclusion & Outlook

To conclude, we have spectroscopically measured the energy shifts of the interorbital interaction as a function of magnetic field. We have identified the peaks by measuring the Rabi frequencies per interaction peak and reproduced the expected functional dependence. From the spectroscopy measurement we found the scattering lengths of the interorbital interaction $a_{eg^+} = 201(5)a_0$ and $a_{eg^-} = 306(6)a_0$ and the scattering length of the direct interaction $a_{eg0} = 253(5)a_0$. The spin-exchange frequency for our experimental parameters was $\Delta V_{ex}/h = -0.60(2)$ kHz.

The interorbital interactions of ^{171}Yb have also recently been measured by the Kyoto group who found $a_{eg^+} = 225(13)a_0$ and $a_{eg^-} = 355(6)a_0$ [23], and the Munich group who found $a_{eg^+} = 240(4)a_0$ and $a_{eg^-} = 389(4)a_0$ [155]. The a_{eg^+} we have measured agrees with the measurement of the Kyoto group, yet not with the measurement of the

Munich group, whereas our a_{eg^-} is significantly different from both. One difference between our experiment and the Kyoto and Munich groups, is that we use a triangular lattice in the 2D direction, whereas those groups use cubic lattices. However, since our calculation of the Wannier functions takes this geometry into account, this should not lead to any deviations. We nevertheless point out that the difference of a_{eg^-} between the Kyoto and Munich group is approximately the same as the difference between the Kyoto group measurement and ours.

However, our measurements do, like the other measurements [23, 155], show the anti-ferromagnetic nature of the spin-exchange interaction in ^{171}Yb, since $V_{\text{ex}} < 0$. This is in stark contrast with the interorbital interactions in ^{87}Sr and ^{173}Yb, which are ferromagnetic. The group in Boulder measured $a_{\text{eg}^+} = 169(8)a_0$ and $a_{\text{eg}^-} = 68(22)a_0$ for ^{87}Sr [20]. For ^{173}Yb the Munich group found $a_{\text{eg}^+} \approx 4 \times 10^3 a_0$ and $a_{\text{eg}^-} = 220(2)a_0$ [21], whereas the Florence group found $a_{\text{eg}^+} = 3.3(3) \times 10^3 a_0$ [22] and later $a_{\text{eg}^+} = 1894(18)a_0$ [157]. Further note that the remarkably large value of a_{eg^+} for ^{173}Yb results in a large direct interaction, which suggests the presence of a very weakly bound molecular state close to the continuum, as will be discussed in the next chapter.

The anti-ferromagnetic nature of the spin-exchange interaction in ^{171}Yb makes it a particularly interesting candidate for the quantum simulation of the anti-ferromagnetic KLM [25, 31–34]. Several theoretical proposals were done over the last decade. The simulation of the 1D KLM is expected to serve as a benchmark, since the phase diagram is well-understood [31], whereas in 2D and 3D the simulation has the potential to answer some of the outstanding questions [32].

The key feature of the KLM is the presence of a localised spin and a mobile spin, in combination with a spin-exchanging on-site interaction. As the mobile spin tunnels in the lattice, it can exchange its spin with the localised spin, leading to rich physics such as heavy Fermi liquid behaviour. Essential in the experimental realisation is the implementation of a state-dependent lattice (SDL) to enable trapping the $^1S_0$ and $^3P_0$ states at different lattice depths. The Munich group has studied dynamics of ground and excited state ^{173}Yb atoms in an SDL at 670 nm and found a tunable confinement-induced resonance, which they attributed to a coupling between an interorbital scattering channel and centre-of-mass excited bound states [163]. Furthermore, the Kyoto group performed loss measurements with ^{171}Yb in a SDL at a wavelength of 650.7 nm, where spin-exchanging interactions were observed [173].

In our experiment a 1D SDL at 660 nm is implemented, trapping the excited state approximately 5.5 times stronger than the ground state. The excited-state atom is chosen as the localised particle to prevent strong excited-excited state atom losses. Over the course of this work, the SDL has been characterised and dynamic measurements similar to those of the Kyoto group [173] were done, as described in detail in Ref. [143].

Chapter 5

Clock Spectroscopy of Fermi-Fermi Mixtures

In this chapter, measurements on the s-wave interactions in interorbital ^{171}Yb-^{173}Yb Fermi-Fermi mixtures are presented. Here, either ^{171}Yb is excited to the $^3P_0$ state while leaving ^{173}Yb in the ground state, or vice versa, denoted by $^{171}_e$Yb-$^{173}_g$Yb and $^{171}_g$Yb-$^{173}_e$Yb, respectively. Using high-resolution clock spectroscopy, we measure the scattering lengths and directly show the SU(2)⊗SU(6) symmetry of both interactions. Both scattering lengths are attractive and comparable, as presented in Sec. 5.1.1.

We further measure losses in these interorbital Fermi-Fermi mixtures, yielding the inelastic parts of the s-wave scattering lengths, as shown in Sec. 5.1.2. Surprisingly, we find a large difference between the losses of both interorbital combinations. Together with the elastic part of the interactions, using a quantum defect theory description [174], we find the short-range reaction probability and estimate the p-wave scattering lengths in Sec. 5.1.3.

Along with our ^{171}Yb measurements (see Ch. 4) and other measurements of interorbital interactions in Yb [21–23, 28, 29, 155, 157, 175, 176], we expect these measurements can be used as a benchmark for future $^1S_0$-$^3P_0$ Yb molecular potential models, of which a simple speculative mass-scaling model is shown in Sec. 5.2. In Sec. 5.3, measurements on three-component Fermi-Fermi mixtures are shown.

The high symmetry can make these Fermi-Fermi mixtures beneficial to observe exotic d-wave superfluidity [93]. Additionally, the interorbital ^{171}Yb-^{173}Yb mixtures could prove to be promising candidates for the quantum simulation of so-called two-flavour superfluid symmetry-locking phases [94, 95].

The work in this chapter was supervised by K. Sengstock & C. Becker. A first version of the measurements was done by B. Abeln, M. Diem, N. Pintul and the author. The final measurements presented in this chapter and its analysis were done by B. Abeln and the author. The speculative mass-scaling model and quantum defect theory analysis were done by the author. The data presented in Sec. 5.1.1 and 5.1.2 was published in Ref. [2].

5.1   Interactions of Spin-Polarised ^{171}Yb - ^{173}Yb

Two parameters fully describe atomic interactions at ultralow temperatures, the elastic and inelastic s-wave scattering lengths. Together these form the complex scattering length $\tilde{a} = a - ib$ [174, 177], where a and $b > 0$ denote the elastic and inelastic parts respectively. The inelastic part of the interaction is often given as a loss coefficient β in units of $\mathrm{cm}^3\mathrm{s}^{-1}$.

For interactions between the $^1S_0$-ground and $^3P_0$-excited state of two-isotope mixtures, spectroscopy on the clock transition measures the elastic part of the interaction [110, 111]. Since the hyperfine splitting between the $^1S_0 \rightarrow {}^3P_0$ transition in ^{171}Yb and ^{173}Yb differ by about 1.2 GHz (see Fig. 2.1), these can easily be excited separately. Losses of these interacting states measure the inelastic part. To ensure only interorbital interisotope interactions play a role, atoms in both isotopes are spin-polarised, thus preventing intraisotope spin-exchanging interactions. Rabi oscillation and magnetic-field-dependence measurements are done to confirm this is not a spin-exchanging interaction.

5.1.1   Elastic SU(2)⊗SU(6)-Symmetric Interactions

Since the atoms making up the interorbital isotope mixtures are distinguishable, the physics describing interactions is different from the spin-exchanging interactions in interorbital intraisotope systems. In the following, the state of the atomic pair is represented by $|o_{171}, m_{F,171}; o_{173}, m_{F,173}\rangle$, where $o_i \in$ [e,g] denotes the orbital state of isotope 'i'. In these spin-polarised isotope mixtures, the elastic part of the s-wave interaction is described by a single scattering length a, which is determined in spectroscopic measurements via the interaction shift (see Eq. 4.14). The interaction shift is given by $\Delta U_{o_{171}o_{173}} = U_{o_{171}o_{173}} - U_{\mathrm{gg}}$. The energies of the clock transition for single atoms and isotope mixtures are depicted in Fig. 5.1, here exemplary for $^{171}_{\mathrm{e}}$Yb -$^{173}_{\mathrm{g}}$Yb. The spectroscopy is performed using π^0-polarised light such that the m_F state is unchanged.

In general every spin combination is subject to a different molecular potential, and hence a different interaction shift. For the $^{171}_{\mathrm{e/g}}$Yb -$^{173}_{\mathrm{g/e}}$Yb isotope mixtures here studied,
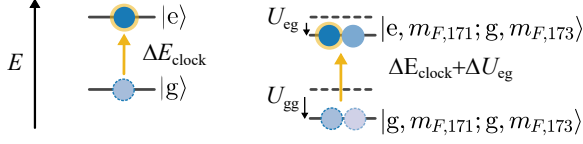
Figure 5.1: Energy scheme of (left) the single-body clock transition in comparison to (right) the interisotope interorbital interaction of a $^{171}_{e}$Yb -$^{173}_{g}$Yb mixture, similar to Fig. 4.2. Both U_{gg} and U_{eg} are attractive. Dark and light blue disks represent ^{171}Yb and ^{173}Yb atoms, respectively.

this leads to twelve unique scattering lengths for all $[m_{F,171}, m_{F,173}]$ combinations. For ground-ground state ^{171}Yb -^{173}Yb, however, SU(2)⊗SU(6) was observed [36], characterised by a single scattering length. In the following it is shown that the same SU(2)⊗SU(6) description holds for interorbital mixtures. This ensures that measuring two instead of twelve spin combinations suffices to probe the symmetry of the interaction.

Because s-wave interactions are rotationally symmetric, the Hamiltonian describing the system commutes with the total angular momentum of the pair $\hat{\mathbf{F}}^2_{\text{tot}}$, defined as the sum of the ^{171}Yb and ^{173}Yb total angular momentum $\hat{\mathbf{F}}_{\text{tot}} = \hat{\mathbf{F}}_{171} + \hat{\mathbf{F}}_{173}$ [2]. The total magnetisation is then given by $M_{\text{tot}} = m_{F,171} + m_{F,173}$, which in combination with F_{tot}, the eigenvalue of $\hat{\mathbf{F}}_{\text{tot}}$, are good quantum numbers. In terms of the basis $|F_{\text{tot}}, M_{\text{tot}}\rangle$, the eigenstates of $\hat{\mathbf{F}}^2_{\text{tot}}$, the Hamiltonian $\hat{\mathcal{H}}_{\text{int}}$ is given by [2]

$$\hat{\mathcal{H}}_{\text{int}} = \frac{4\pi\hbar}{2\mu}\delta(\mathbf{r}_{171} - \mathbf{r}_{173}) \sum_{F_{\text{tot}}=F_{\text{min}}}^{F_{\text{max}}} \sum_{M_{\text{tot}}=-F_{\text{tot}}}^{F_{\text{tot}}} a_{F_{\text{tot}}}|F_{\text{tot}}, M_{\text{tot}}\rangle\langle F_{\text{tot}}, M_{\text{tot}}|, \qquad (5.1)$$

where $\delta(\mathbf{r}_{171} - \mathbf{r}_{173})$ is the Dirac δ-function as a function of positions $\mathbf{r}_{171}$ and $\mathbf{r}_{173}$, and $a_{F_{\text{tot}}}$ is the F_{tot}-dependent scattering length. Since the angular momenta of both the ground and excited states are 1/2 for ^{171}Yb and 5/2 for ^{173}Yb, the total angular momentum of the pair is $F_{\text{tot}} \in [2, 3]$. Therefore, measuring the scattering lengths a_2 and a_3 suffices to test the symmetry and quantify the elastic interactions.

In experiments, however, we prepare atoms in a single m_F state (see Sec. 2.3.1). Using a basis transformation, the magnetisation basis $|m_{F,171}; m_{F,173}\rangle$ can be written in terms of the $|F_{\text{tot}}, M_{\text{tot}}\rangle$ basis via [2]

$$|m_{F,171}; m_{F,173}\rangle = \sum_{M_{\text{tot}}} c^{F_{\text{tot}},M_{\text{tot}}}_{m_{F,171};m_{F,173}}|F_{\text{tot}}, M_{\text{tot}}\rangle, \qquad (5.2)$$

where $c^{F_{\text{tot}},M_{\text{tot}}}_{m_{F,171};m_{F,173}}$ are the Clebsch-Gordan coefficients and where the summation goes

over all combinations of $m_{F,171}$ and $m_{F,173}$ such that $M_{\text{tot}} = m_{F,171} + m_{F,173}$. In this way, most two spin combinations[*] can be used to determine a_2 and a_3.

Spectroscopic Measurement of Elastic Interactions

To measure the elastic scattering lengths of two spin combinations of both $^{171}_{\text{e/g}}$Yb -$^{173}_{\text{g/e}}$Yb mixtures, we start with a ground state mixture of spin-polarised ^{171}Yb and ^{173}Yb (see Sec. 2.2.5 and Sec. 2.3.1) with about 10 to 40 thousand atoms per isotope at temperatures of about 0.25 to 0.55 T_{F}. This mixture is adiabatically loaded into a deep optical lattice and spectroscopy is performed, as described in Sec. 3.2.1. Either ^{171}Yb or ^{173}Yb is excited to measure the $^{171}_{\text{e}}$Yb -$^{173}_{\text{g}}$Yb or $^{171}_{\text{g}}$Yb -$^{173}_{\text{e}}$Yb interaction shifts, respectively. The quantisation axis is set by a magnetic field of 8.8 G in the y-direction, though the interactions are independent of magnetic field, as shown later in this section.

Figure 5.2 shows typical spectra of $^{171}_{\text{e}}$Yb -$^{173}_{\text{g}}$Yb mixtures, where $m_{F,171} = -1/2$, and $m_{F,171} = 5/2$ and $3/2$ in (a) and (b), respectively. Each colour denotes a different 1D lattice depth, whereas the 2D lattice depth was $s_{2\text{D}} = 16.971(15)E_{\text{r}}$. The spectra were taken using a pulse time of $t_{\text{p}} = 1.6$ ms, yielding a Fourier-limited peak with a full-width half-maximum (FWHM) of about 500 Hz. The peaks at $\delta = 0$ are due to the single-atom ^{171}Yb intraband transition, which is independent of the lattice depth. The single-atom peaks are fitted using Eq. 3.1 times a constant which accounts for their non-unity occupation in the lattice. The clock frequency of the single-atom peaks is monitored over all runs and fitted with a linear function to apply an *a posteriori* linear drift compensation[†]. Around 4 kHz the interaction peaks shows up, which are fitted with Lorentzians. These describe the interaction peaks significantly better than sinc^2 functions, which we attribute to decoherence (see also Sec. 3.1.2 and Sec. 5.1.1). Furthermore, the non-uniformity of the lattice can produce an asymmetric interaction peak, but this effect was estimated and determined to be negligible (see App. A). The interaction shift increases for increasing $s_{1\text{D}}$, as is expected from Eq. 4.14. The third peak, above 18 kHz is the single-atom ^{171}Yb blue-sideband transition, where a single atom from the lowest lattice band is excited into the second lattice band. These interband peak are fitted with Lorentzians, which describe the peaks well at these lattice depths[‡].

---

[*] Spin combinations $|m_{F,171}; m_{F,173}\rangle$ and $|-m_{F,171}; -m_{F,173}\rangle$ do not suffice to determine a_2 and a_3, due to the symmetry of the Clebsch-Gordan coefficients.

[†] Though a drift compensation of about -0.11 Hz/s was applied during the measurements, small linear drifts remain, typically of about 20 mHz/s. These are cancelled out by an *a posteriori* linear drift compensation per ten spectra. The residuals, which give an estimate of the non-linear drifts, are typically smaller than 15 Hz from spectrum to spectrum, which is small compared to the measured interaction shifts and peak widths. For further details, see Ref. [143].

[‡] At smaller lattice depths, below about $10E_{\text{r}}$, the shape of the interband peak is asymmetric and a more detailed analysis is needed. Measurements were done to study this regime, which are presented in Ref. [143].
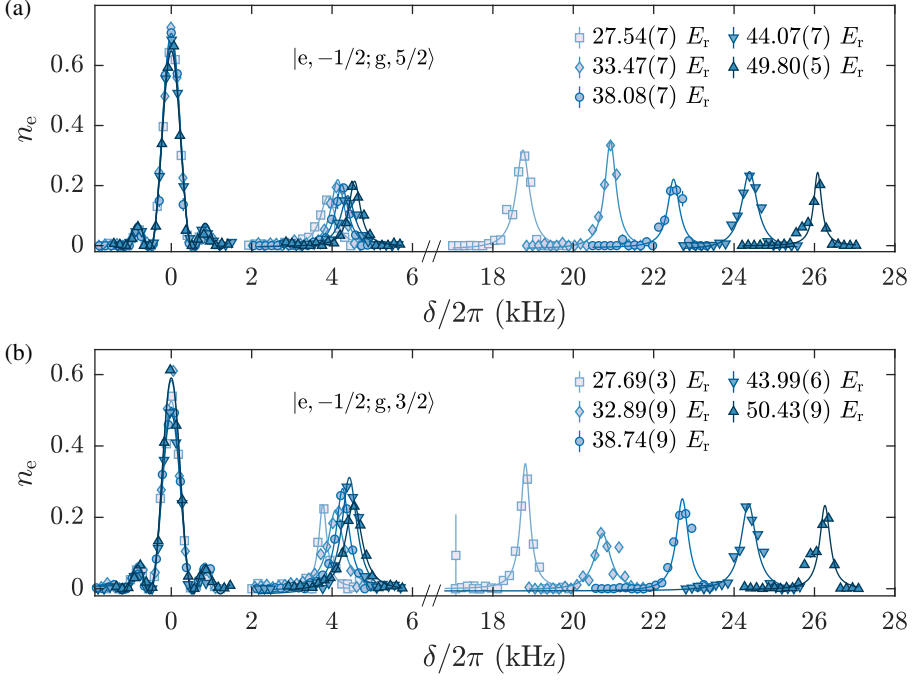
Figure 5.2: Clock spectroscopy of $^{171}_{\mathrm{e}}$Yb-$^{173}_{\mathrm{g}}$Yb mixtures. Data points represent the measured excitation fractions and error bars are the uncertainty in the determination (typically smaller than the marker size). Solid lines indicate fits to the data (see text). Different colours and markers indicate different $s_{1\mathrm{D}}$ (see legend). Note that the x-axis is shortened between 6 and 16 kHz. (a) shows the measurement of the $|e, -1/2; g, 5/2\rangle$ mixture and (b) shows the spectra of the $|e, -1/2; g, 3/2\rangle$ mixture. The figure is adapted from the published version [2]. © 2021 American Physical Society.

This enables us to measure the 1D lattice depth during the measurement, improving the accuracy of the scattering length. As explained in detail in Ref. [143], a lattice band calculation is performed to obtain $s_{1\mathrm{D}}$ from the energy shift. Because the clock beam propagates perpendicular to the 2D lattice, we cannot excite single atoms on the blue sideband of the 2D lattice and hence rely on the lattice-modulation spectroscopy performed directly before or after the measurements (see Sec. 2.4).

From these spectroscopic measurements, the interaction shifts ΔU_{eg}, the energy

difference between the single and interaction peaks, of both spin combinations are obtained as a function of s_{1D}. These measurements are repeated for several 1D lattice depths for both spin combinations and plotted in Fig. 5.3. Using Eq. 4.14, we find the scattering length by averaging over all

$$\Delta a_{m_{F,171};m_{F,173}} = \Delta U_{eg}(s_{1D})/(4\pi\hbar^2/2\mu) \int d\mathbf{r} \, |w_0(\mathbf{r}, s_{1D}, s_{2D})|^4 \qquad (5.3)$$

per spin combination*. We obtain $\Delta a_{-1/2,+5/2} = 498(1)a_0$ and $\Delta a_{-1/2,+3/2} = 495.7(1.3)a_0$. Note that by considering the scattering length $\Delta a_{eg} = a_{eg} - a_{gg}$ we do not need to account for the large relative uncertainty of the ground-ground state interaction $a_{gg} = -5.8(6) \times 10^2 \, a_0$ [86]. The solid and dashed line in Fig. 5.3 show the interaction shift using the best estimate of $\Delta a_{-1/2,+5/2}$ and $\Delta a_{-1/2,+3/2}$, respectively, and the calculated Wannier integral at the used lattice depths. These lines describe the data well, further confirming that a two-atom interaction peak was measured.

To obtain Δa_2 and Δa_3, the basis transformation of Eq. 5.2 is applied to find [2]

$$|-1/2, 5/2\rangle = \sqrt{\frac{1}{6}}|3, 2\rangle - \sqrt{\frac{5}{6}}|2, 2\rangle \qquad (5.4)$$

$$|-1/2, 3/2\rangle = \sqrt{\frac{1}{3}}|3, 1\rangle - \sqrt{\frac{2}{3}}|2, 1\rangle, \qquad (5.5)$$

and hence $\Delta a_2 = 2\Delta a_{-1/2,5/2} - \Delta a_{-1/2,3/2} = 501.2(2.5)a_0$ and $\Delta a_3 = -4\Delta a_{-1/2,5/2} + 5\Delta a_{-1/2,3/2} = 485(8)a_0$. Comparing the two, we conclude that Δa_2 and Δa_3 do not differ significantly from each other and that we observe SU(2)⊗SU(6) symmetry within our experimental uncertainties. We calculate the average scattering length $\Delta \bar{a}_{eg} = 497.4(8)a_0$ from the measured scattering lengths $a_{m_{F,171};m_{F,173}}$, thus describing the elastic part of the $^{171}_e$Yb -$^{173}_g$Yb interaction regardless of spin combination. Using the ground-ground state interaction $a_{gg} = -5.8(6) \times 10^2 \, a_0$ [86] we thus find $\bar{a}_{eg} = -8(6) \times 10^1 \, a_0$, where we note that the large relative uncertainty is predominantly caused by the uncertainty in a_{gg}.

We repeat these measurements on the $^{171}_g$Yb -$^{173}_e$Yb mixture with two spin combinations. Figure 5.4 shows a typical measurement, where using the same initial mixtures as before, ^{173}Yb is excited while ^{171}Yb remains in the ground state. Here the 2D lattice depth was $s_{2D} = 16.13(17)E_r$ and the pulse time was $t_p = 1.55$ ms, yielding a Fourier-limited peak with a width of about 516 Hz. Similar to before, the peaks at $\delta = 0$ are

---

*We preferred this method since in this way the uncertainty in the Wannier integral due to the 1D and 2D lattices is included. Directly fitting Eq. 4.14 while leaving a as a free parameter neglects the uncertainties in s_{1D} and s_{2D}.
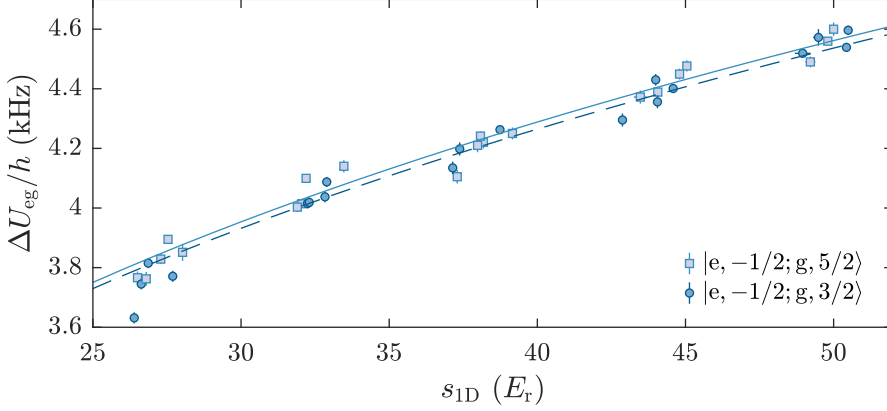
Figure 5.3: Interaction shifts of the $^{171}_{\mathrm{e}}$Yb -$^{173}_{\mathrm{g}}$Yb mixture as a function of 1D lattice depth. Data points are obtained from fits to spectra, such as in Fig. 5.2, and error bars indicate the uncertainties in the determination of ΔU_{eg} and s_{1D}. The solid and dashed lines show fits to the data (see text) of the $|e, -1/2; g, 5/2\rangle$ and $|e, -1/2; g, 3/2\rangle$ mixtures, respectively. The figure is adapted from the published version [2]. © 2021 American Physical Society.

due to single excited ^{173}Yb atoms, the peaks around 4 kHz are due to the interisotope interaction and the peaks above 16 kHz are due to the single-atom interband transition. Compared to the $^{171}_{\mathrm{e}}$Yb -$^{173}_{\mathrm{g}}$Yb measurement in Fig. 5.2, the single-atom intra- and interband peaks are significantly lower, suggesting that the atomic sample had fewer singly-occupied sites. We have observed the peak heights depend on the atom numbers of both isotopes and the temperatures. However, the interaction shifts ΔU are not effected by differences in total atom number.

Figure 5.5 shows the interaction shifts ΔU_{ge} as a function of the 1D lattice depth, both obtained from the spectroscopic measurements, such as depicted in Fig. 5.4 and repeated several times. In the same way as before, we find the scattering lengths $\Delta a_{-1/2,+5/2} = 481.3(1.8)a_0$ and $\Delta a_{+1/2,+5/2} = 482.9(1.3)a_0$. From these two, we find Δa_2 and Δa_3 using the basis transformation [2]

$$| +1/2, 5/2\rangle = |3, 3\rangle \tag{5.6}$$

$$| -1/2, 5/2\rangle = \sqrt{\frac{1}{6}}|3, 2\rangle - \sqrt{\frac{5}{6}}|2, 2\rangle, \tag{5.7}$$
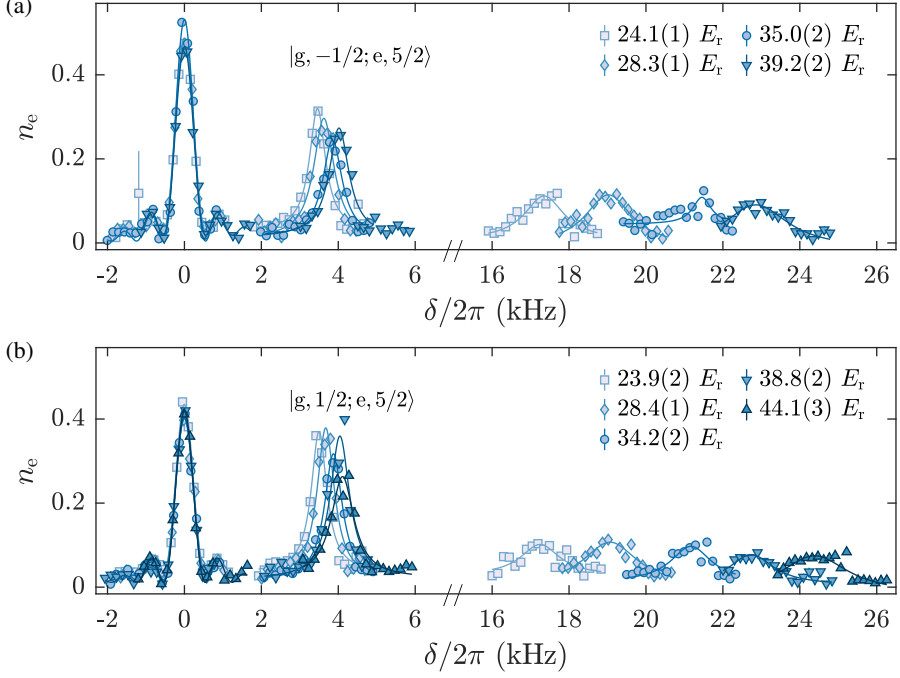
Figure 5.4: Clock spectroscopy of $^{171}_{\rm g}$Yb -$^{173}_{\rm e}$Yb mixtures, analogous to Fig. 5.2. (a) shows the measurement of the $|{\rm g}, -1/2; {\rm e}, 5/2\rangle$ mixture and (b) shows the spectra of the $|{\rm g}, 1/2; {\rm e}, 5/2\rangle$ mixture. Note that the x-axis is shortened between 6 and 15 kHz. The figure is adapted from the published version [2]. © 2021 American Physical Society.

and hence $\Delta a_2 = 6/5\Delta a_{-1/2,5/2} - 1/5\Delta a_{+1/2,5/2} = 481(2)a_0$ and $\Delta a_3 = \Delta a_{+1/2,5/2} = 482.9(1.3)a_0$. Comparing the two, we conclude that Δa_2 and Δa_3 do not differ significantly from each other and that we again observe SU(2)⊗SU(6) symmetry within our experimental uncertainties. Then, the average scattering length $\Delta \bar a_{\rm ge} = 482(1)a_0$ is obtained from the measured scattering lengths $a_{m_{F,171};m_{F,173}}$, thus describing the elastic part of the $^{171}_{\rm g}$Yb -$^{173}_{\rm e}$Yb interaction regardless of spin combination. As before, using $a_{\rm gg} = -5.8(6) \times 10^2\, a_0$ [86] we thus find $\bar a_{\rm ge} = -1.0(6) \times 10^2\, a_0$.

Table 5.1 gives an overview of the elastic scattering lengths measured for both interorbital interisotope interactions. We have observed SU(2)⊗SU(6) symmetry for both interactions. The relative deviations between Δa of both measured spin combinations
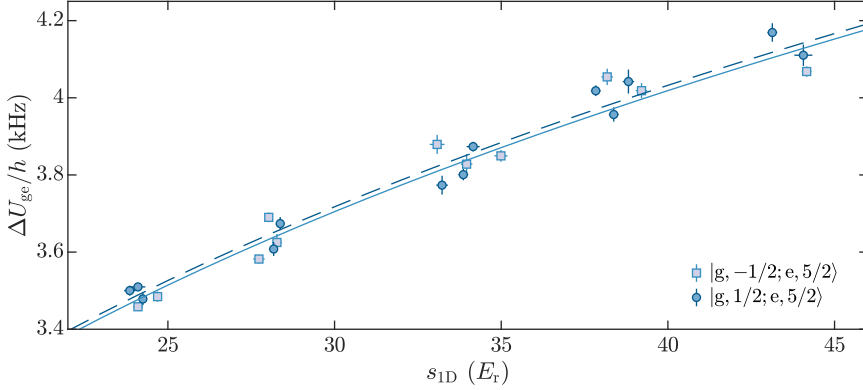
Figure 5.5: Interaction shifts of the $^{171}_{\,g}$Yb - $^{173}_{\,e}$Yb mixture as a function of 1D lattice depth, analogous to Fig. 5.3. The solid and dashed line show fits to the data (see text) of the $|g, -1/2; e, 5/2\rangle$ and $|g, 1/2; e, 5/2\rangle$ mixtures, respectively. The figure is adapted from the published version [2]. © 2021 American Physical Society.

are less than 1%. Theoretical predictions have shown that the SU($\mathcal{N}$) symmetry of ground-excited state interactions are expected to be broken below 0.1% [25]. Future more accurate studies of this interaction could be interesting to test this prediction.

It turns out the average scattering lengths $\Delta\bar{a}_{eg}$ and $\Delta\bar{a}_{ge}$ are similar, yet differ significantly. We attribute this similarity to the high degree of symmetry between $^{171}_{\,e}$Yb - $^{173}_{\,g}$Yb and $^{171}_{\,g}$Yb - $^{173}_{\,e}$Yb pairs, since the electronic structure of both isotopes is only different by hyperfine effects. Though a mass-scaling model has been applied successfully to describe intra- and interisotope interactions in ground-ground state Yb$_2$ [86], a prospective similar model for excited-ground state interactions requires additional terms to explain the difference between ^{171}Yb - $^{173}_{\,g}$Yb and $^{171}_{\,g}$Yb - $^{173}_{\,e}$Yb, which have the same reduced mass. We therefore think this measurement could be an interesting benchmark for beyond-mass scaling contributions to molecular potentials, though for a quantitative treatment of a_{gg} must be performed with an accuracy of less than about $5a_0$ to reduce the error on the absolute scattering lengths $\bar{a}_{eg}$ and $\bar{a}_{ge}$. Finally, note that the absolute scattering lengths $\bar{a}_{eg} = -8(6) \times 10^1\, a_0$ and $\bar{a}_{ge} = -1.0(6) \times 10^2\, a_0$ suggest that the interaction is attractive in nature.

Table 5.1: Summary of the elastic scattering lengths measured in this work [2]. The quantity $\bar{a}$ is the averaged spin state independent scattering length. All values are given in units of $a_0 \approx 5.29 \times 10^{-11}$ m [156].

Quantity	$^{171}_{e}$Yb -$^{173}_{g}$Yb	$^{171}_{g}$Yb -$^{173}_{e}$Yb
$\Delta a_{-1/2,+5/2}$	498(1)	481.3(1.8)
$\Delta a_{-1/2,+3/2}$	495.7(1.3)	-
$\Delta a_{+1/2,+5/2}$	-	482.9(1.3)
Δa_2	501.2(2.5)	481(2)
Δa_3	485(8)	482.9(1.3)
$\Delta \bar{a}$	497.4(8)	482(1)

Rabi Oscillations

Different from the spin-exchanging interactions discussed in Ch. 4, the interisotope interactions are expected to have the same Rabi couplings as single atoms. To verify this, we measure Rabi oscillations at the single-atom and interaction resonance frequencies for both interisotope mixtures. The measurements are treated in detail in Ref. [143], and a brief overview is given here.

A spin-polarised mixture of about 25(5) thousand ^{171}Yb atoms and a similar number of ^{173}Yb atoms is loaded into a lattice of depth $s_{1D} = 28.7(2)E_r$, $s_{2D} = 16.8(1)E_r$. The magnetic field is set to $B = 8.8$ G and ^{171}Yb is excited. Figure 5.6 shows typical Rabi oscillations on the single-atom and interaction resonances. Similarly to Sec. 4.2.1, the data was fitted with the numerical solutions of the optical Bloch equations. Here Γ_s was neglected, the detunings were obtained from spectroscopy measurements on the respective peaks* and a factor was introduced to account for the non-unity occupations. The measurements were repeated three times, and yield average bare Rabi frequencies of $\Omega_0 = 2\pi \times 352(4)$ Hz for the single-atom resonance and $\Omega_0 = 2\pi \times 356.4(7)$ Hz for the interaction resonance, corroborating that both couplings are the same. We furthermore find a decoherence rate of the interacting pairs of $\Gamma_c = 2\pi \times 24(3)$ Hz, smaller than the

---

* The spectroscopy was done directly after each Rabi oscillation measurement and we found that $|\delta| < \Omega_0/3$ for the single-atom peak and $|\delta_{int}| < \Omega_0/5$ for the interaction peak.
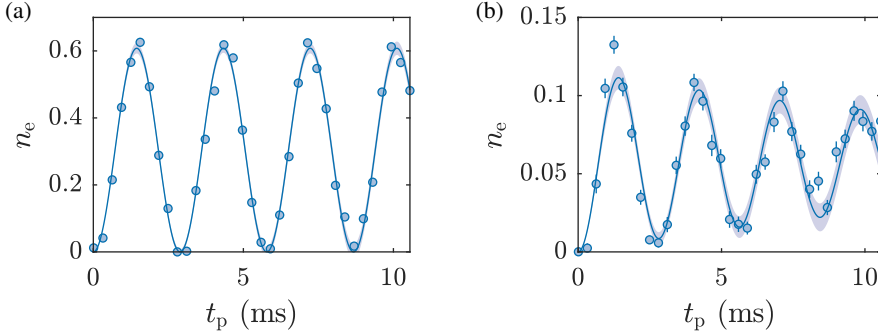
Figure 5.6: Typical Rabi oscillations of (a) single atoms and (b) interacting pairs in the $^{171}_{\text{e}}$Yb - $^{173}_{\text{g}}$Yb mixture. Data points show the measured excitation fractions with error bars the experimental uncertainty. Solid lines show the fitted optical Bloch equations (see text) and the shaded area shows the 95% confidence interval of the fit.

decoherence of spin-exchanging interactions in ^{171}Yb.

The measurement was repeated analogously for the $^{171}_{\text{g}}$Yb - $^{173}_{\text{e}}$Yb interactions, yielding $\Omega_0 = 2\pi \times 356.1(6)$ Hz for the single-atom resonance and $\Omega_0 = 2\pi \times 351(5)$ Hz for the interaction resonance, again corroborating that both couplings are the same. Here, however, the average decoherence rate of the pairs is $\Gamma_{\text{c}} = 2\pi \times 1.0(1) \times 10^2$ Hz, considerably larger than the decoherence in both the other interorbital mixture and spin-exchanging interactions in ^{171}Yb. The difference is currently not understood, though for more details see Ref. [143].

Verification of the Magnetic Field Independence

As explained in Sec. 5.1.1, the theoretical description of the interisotope interorbital interactions is markedly different from the spin-exchanging interorbital interactions as presented in Ch. 4. One major difference is the magnetic field dependence, which is not present in the interisotope interorbital interactions. Here, this independence is verified for the $^{171}_{\text{e}}$Yb - $^{173}_{\text{g}}$Yb interaction, though the same is expected to hold for the $^{171}_{\text{g}}$Yb - $^{173}_{\text{e}}$Yb interaction.

Clock spectroscopy is performed as in Sec. 5.1.1, but for varying magnetic fields and at constant lattice depths of $s_{\text{1D}} = 47.0(5)E_{\text{r}}$ and $s_{\text{2D}} = 26.1(2)E_{\text{r}}$. About 19(4) thousand ^{171}Yb atoms are loaded into the lattice with approximately the same number of ^{173}Yb atoms, and pulse times of 1.8 ms were used, leading to a Fourier-limited
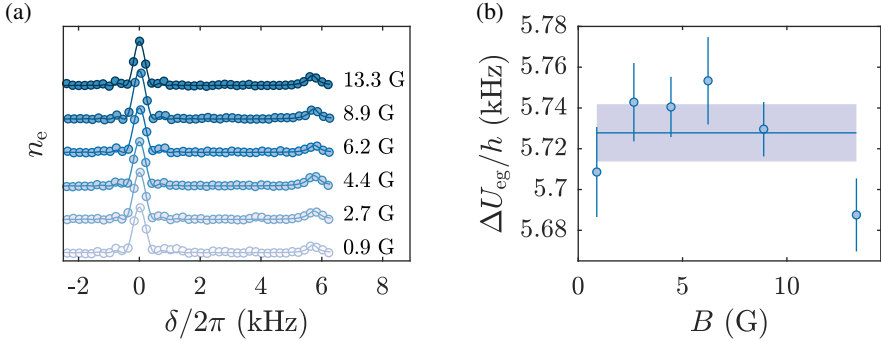
Figure 5.7: (a) Clock spectroscopy of $^{171}_e$Yb -$^{173}_g$Yb mixtures while varying the magnetic field, analogous to Fig. 5.2. Different colours indicate different magnetic fields, denoted on the right. Note that n_e is offset in the y-direction and that the detuning is with respect to the single atom transition. (b) Measured interaction shifts as a function of magnetic field, as obtained from fits to the spectroscopic data in (a). The data points represent the interaction shift between the single-atom and interaction peaks, and the error bars indicate the fit uncertainty. The solid line indicates the average interaction shift and the shaded area the 95% confidence interval.

FWHM line width of about 440 Hz. The resulting spectra are shown in Fig. 5.7a. The peak at zero detuning is identified as the single-atom transition, whereas the peak at $\delta/2\pi \approx 5.7$ kHz is identified as the interisotope interaction peak. As before, the single-atom and interaction peaks are fitted with a sinc^2 and Lorentzian, respectively. Note that in Fig. 5.7a the Zeeman shift has dropped out, since the detuning δ is calculated with respect to the single-atom transition.

Using the peak positions, the interaction shifts are determined, and shown in Fig. 5.7b as a function of the magnetic field. Each measured shift is within two standard deviations of the average. Therefore, we conclude that within our experimental uncertainties the interaction shift is independent of magnetic field for $B \lesssim 13.3$ G. The interaction shift for each magnetic field is furthermore well within 1% of the average shift, which hence functions as an upper limit of how insensitive the interaction is to variations in the magnetic field. We attribute the residual deviations to non-linear drifts and small fluctuations in the lattice depths. In the spectroscopy measurement presented in Sec. 5.1.1, we have observed that after *a posteriori* linear drift compensation the non-linear drifts are typically within 15 Hz over a few hours. Furthermore, the lattice depths were determined with an accuracy of about 1% (compare s_{1D} and s_{2D} above), which can be
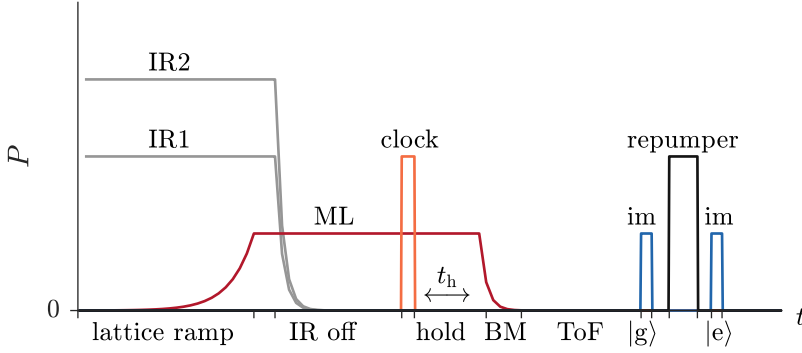
Figure 5.8: Schematic of a loss measurement sequence (not to scale), showing the laser beam powers P as a function of time t, analogous to Fig. 3.6. The hold time t_h after the clock pulse is varied.

caused by shot-to-shot fluctuations in the lattice beam powers. The spread in lattice depths results in a spread in the Wannier integrals of approximately 0.5%. These two effects are therefore expected to be the current limiting factors in our experiment.

Lastly, note that the interisotope interaction is not expected to exhibit an interorbital Feshbach resonance, unlike the interorbital spin-exchange interaction in ^{171}Yb [155] and ^{173}Yb [28]. The spin-exchange interaction is described by two molecular potentials, and the interorbital Feshbach resonance appears because a bound state of one of the potentials comes into resonance with the open channel of the other potential for a certain Zeeman energy shift. This is markedly different from the interisotope interactions here measured, since a single molecular potential describes the interaction.

5.1.2 Inelastic Interactions

To fully characterise the s-wave interactions of interorbital ^{171}Yb - ^{173}Yb mixtures, loss measurements were done to determine the inelastic scattering length. Similarly to the spectroscopy described in Sec. 5.1.1, spin-polarised ground-ground state mixtures are loaded into the 'magic' lattice at a magnetic field of 8.8 G and excited on either the ^{171}Yb or ^{173}Yb clock transition using the previously-found interorbital resonances. In this way, the sample consists of single ^{171}Yb and ^{173}Yb atoms, and interacting interorbital pairs. Subsequently, the atoms are held in the deep lattice for a variable hold time t_h, as depicted in Fig. 5.8, which is referred to as a *loss measurement* in the following.
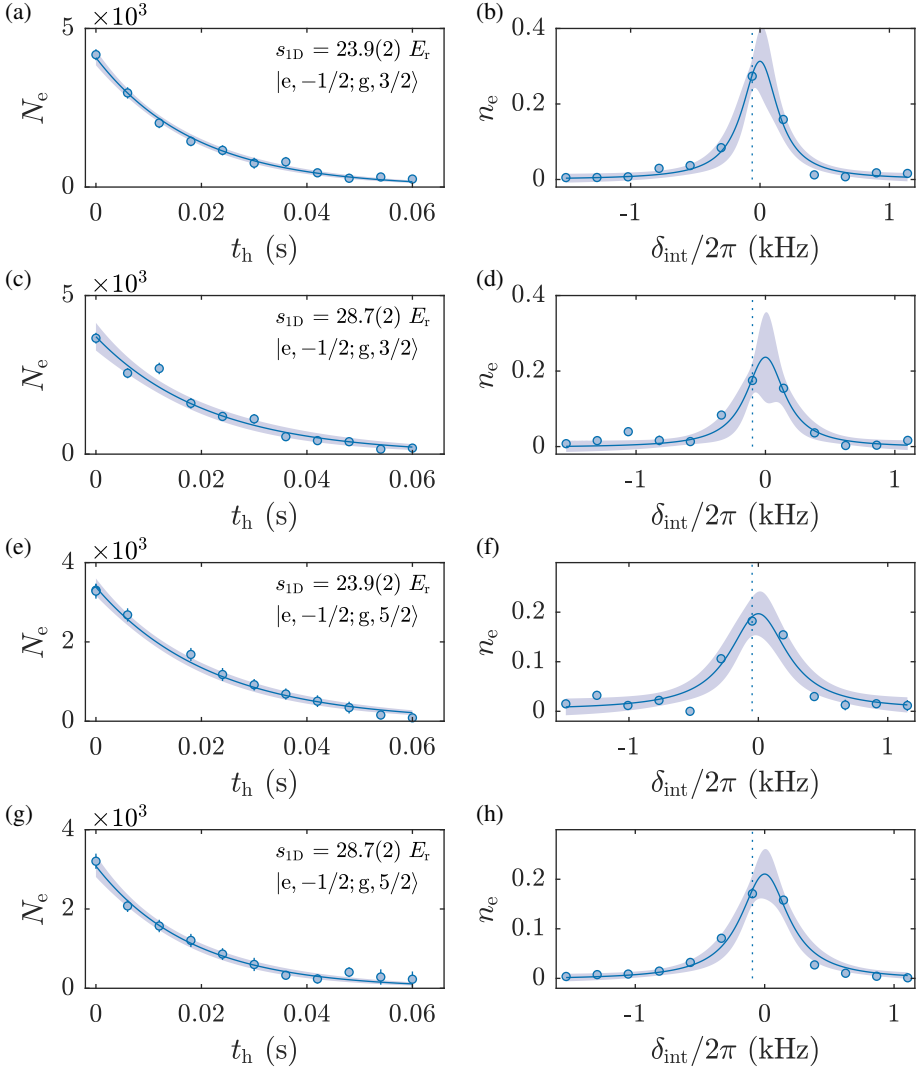
Figure 5.9: Typical loss measurements of $|e, -1/2; g, 3/2\rangle$ and $|e, -1/2; g, 5/2\rangle$ pairs. The left column shows loss measurements for different 1D lattice depths and spin configurations, denoted in the graph. Data points show the single-shot atom number and error bars show the uncertainty in its determinations. Solid lines show the fitted exponential (see text) and the shaded area shows its 95% confidence interval. The right column shows spectroscopy of the interaction peak, similar to Fig. 5.2 and 5.4. Here, n_e is plotted as a function of the detuning δ_{int} with respect to the interaction peak. The dashed line shows the frequency at which the corresponding loss measurement was done. The figure is adapted from the published version [2]. © 2021 American Physical Society.

Figure 5.9 shows typical loss measurements of the $^{171}_{e}$Yb -$^{173}_{g}$Yb mixture, where the number of excited-state ^{171}Yb atoms is shown. The excited state atom number shows an exponential decay, for the following reasons. Excited state atoms on lattice sites with another isotope are subject to two loss processes. First, inelastic collisions with the other isotope cause losses. Second, $|e\rangle$ atoms can be lost via one-body decays due to scattering of the lattice light, collisions with background atoms in the vacuum and spontaneous decay. Since both processes are stochastic, they show up as exponential decays*. The total decay rate of the excited state atom number Γ_{tot} is thus given by $\Gamma_{\text{tot}} = \Gamma_{\text{in}} + \Gamma_0$, where Γ_{in} denotes the inelastic decay rate and Γ_0 denotes the one-body decay rate. Hence, the excited state atom number is fitted with $N_{\text{e},0} \exp(-\Gamma_{\text{tot}}t_{\text{h}})$, where $N_{\text{e},0}$ is the initial atom number at $t_{\text{h}} = 0$. The fits are shown in Fig. 5.9a, 5.9c, 5.9e and 5.9g, and describe the data well.

To ensure we measure at a frequency close to the desired resonance frequency and to ensure drifts are negligible, we measure the interorbital interisotope interaction peak directly after each loss measurement. The corresponding spectra are shown in Fig. 5.9b, 5.9d, 5.9f and 5.9h. The data is fitted with a Lorentzian as described in Sec. 5.1.1, and the resonance frequency at which the loss measurement was performed is indicated by the vertical dashed line.

To obtain the inelastic loss rate Γ_{in}, we additionally perform a loss measurement on the single-atom resonance just before the interaction loss measurement. In this way, only single atoms are excited and the one-body loss rate Γ_0 is obtained, which is typically on the order of 0.4 Hz. Using the thus found Γ_0 and Γ_{tot}, the inelastic loss rates of the $^{171}_{e}$Yb -$^{173}_{g}$Yb interaction are found.

These three measurements, measuring Γ_{tot}, Γ_0 and the interaction spectrum, were performed several times and repeated for five different 1D lattice depths. The same was done for two spin configurations $|e, -1/2; g, 3/2\rangle$ and $|e, -1/2; g, 5/2\rangle$. The data was post-selected to ensure each loss measurement was done close to the interaction resonance. Figure 5.10 shows the inelastic decay rates as a function of 1D lattice depth for both spin configurations of the $^{171}_{e}$Yb -$^{173}_{g}$Yb mixture.

Similar to the elastic interaction in Eq. 4.14, for inelastic interactions the decay rates are related to the universal decay coefficient $\beta_{m_{F,171};m_{F,173}}$ via [2]

$$\Gamma_{\text{in}}(s_{1D}) = \beta_{m_{F,171};m_{F,173}} \int d\mathbf{r} |w_0(s_{1D}, s_{2D}, \mathbf{r})|^4 \qquad (5.8)$$

$$= \frac{4\pi\hbar}{2\mu} b_{m_{F,171};m_{F,173}} \int d\mathbf{r} |w_0(s_{1D}, s_{2D}, \mathbf{r})|^4 \qquad (5.9)$$

---

* For this reason we here consider the excited state atom number. The excitation fraction n_{e} is subject to more complicated dynamics since an unknown number of the excited atoms decays back into the ground state.
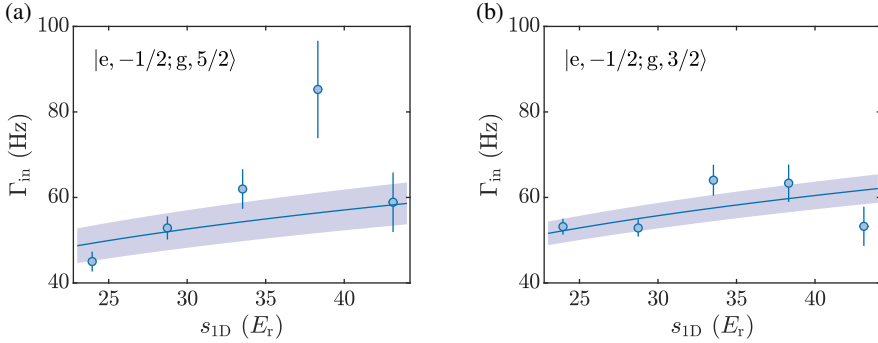
Figure 5.10: Decay rates of the $^{171}_{e}$Yb -$^{173}_{g}$Yb mixture as a function of 1D lattice depth of two spin configurations (see graph). The data points represent Γ_{in} as obtained from loss measurements and are typically three times averaged, and error bars indicate the propagated uncertainties. The solid lines show the expected $\Gamma_{in}(s_{1D})$ based on the obtained $\beta_{m_{F,171};m_{F,173}}$ and the shaded areas show its 95% confidence interval. The figure is adapted from the published version [2]. © 2021 American Physical Society.

where the decay coefficient was rewritten in terms of the inelastic scattering length $b_{m_{F,171};m_{F,173}}$. Using Eqs. 5.8 and 5.9 for the $^{171}_{e}$Yb -$^{173}_{g}$Yb mixtures, we find the decay coefficient per spin configuration $\beta_{-1/2,+5/2} = 1.69(7) \times 10^{-12}$ cm^{3}s^{-1} and $\beta_{-1/2,+3/2} = 1.79(5) \times 10^{-12}$ cm^{3}s^{-1}, or equivalently $b_{-1/2,+5/2} = 6.9(3)a_0$ and $b_{-1/2,+3/2} = 7.3(2)a_0$*, summarised in Table 5.2. Based on the decay coefficients, the expected $\Gamma_{in}(s_{1D})$ is calculated and shown as solid lines in Fig. 5.10, where the shaded area denotes its 95% confidence interval. Save for one outlier the expected $\Gamma_{in}(s_{1D})$ describes the data well.

The loss measurements are repeated for the $^{171}_{g}$Yb -$^{173}_{e}$Yb interaction, shown in Fig. 5.11. In complete analogy to the $^{171}_{e}$Yb -$^{173}_{g}$Yb mixture, the losses of interacting pairs and single atoms and the interaction peak resonance are measured. Here all measurements were done at $s_{2D} = 17.0(4)E_r$. The measurement is repeated several times for several 1D lattice depths and for two spin configurations $|g, 1/2; e, 5/2\rangle$ and $|g, -1/2; e, 5/2\rangle$. The loss data is described well by the exponential fit.

---

* Here the decay coefficients were obtained analogously to the elastic scattering lengths, by taking the average of $\beta = \Gamma_{in}(s_{1D})/\int d\mathbf{r}|w_0(s_{1D}, s_{2D}, \mathbf{r})|^4$ over all 1D lattice depths, and similarly for the inelastic scattering lengths.
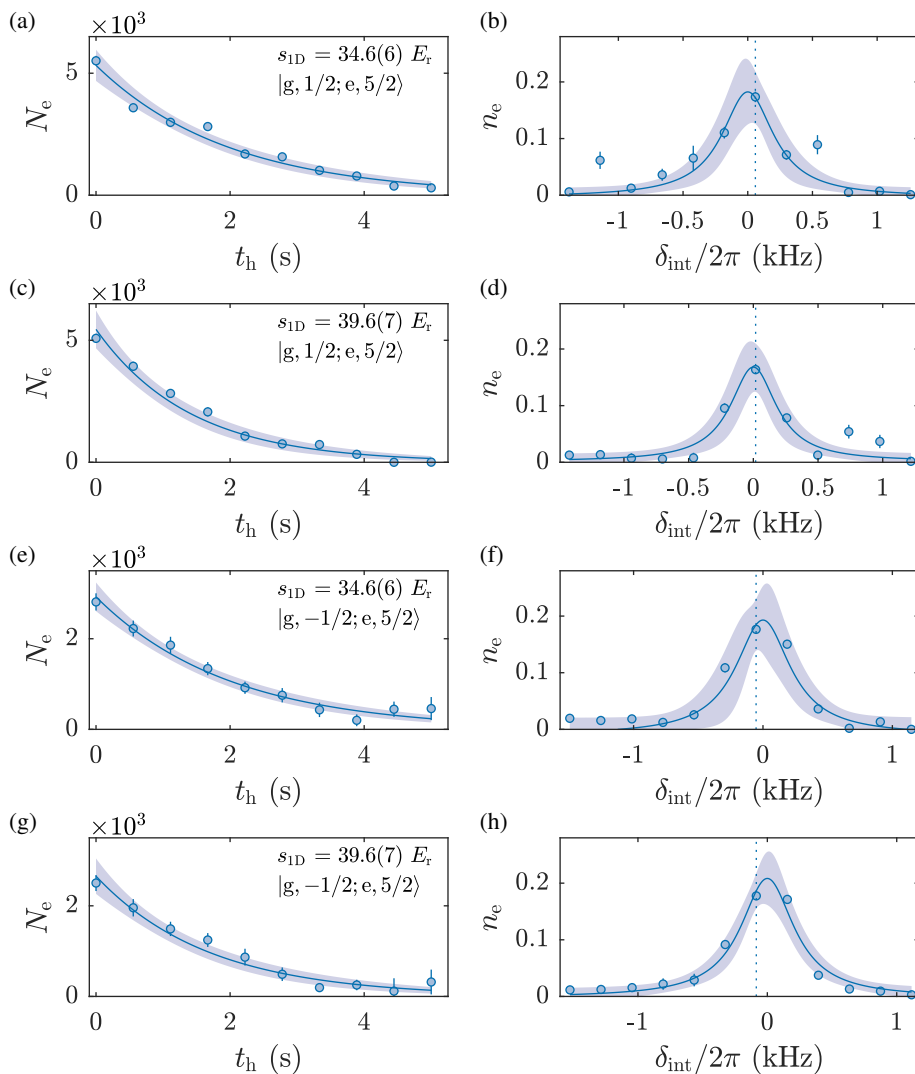
Figure 5.11: Typical loss measurements of $|g, 1/2; e, 5/2\rangle$ and $|g, -1/2; e, 5/2\rangle$ pairs, analogous to Fig. 5.9. The figure is adapted from the published version [2]. © 2021 American Physical Society.

Table 5.2: Summary of all inelastic interaction parameters measured in this work [2]. The subscripts i and j in $\beta_{i,j}$ and $b_{i,j}$ represent the m_F state of the ^{171}Yb and ^{173}Yb isotopes, respectively.

Quantity	$^{171}_{\text{e}}$Yb -$^{173}_{\text{g}}$Yb	$^{171}_{\text{g}}$Yb -$^{173}_{\text{e}}$Yb
$\beta_{-1/2,+5/2}$	$1.69(7) \times 10^{-12}$ cm^{3}s^{-1}	$4.6(1.7) \times 10^{-15}$ cm^{3}s^{-1}
$b_{-1/2,+5/2}$	$6.9(3)a_0$	$0.019(7)a_0$
$\beta_{-1/2,+3/2}$	$1.79(5) \times 10^{-12}$ cm^{3}s^{-1}	-
$b_{-1/2,+3/2}$	$7.3(2)a_0$	-
$\beta_{+1/2,+5/2}$	-	$3(1) \times 10^{-15}$ cm^{3}s^{-1}
$b_{+1/2,+5/2}$	-	$0.013(4)a_0$

Figure 5.12 shows the inelastic decay rates as obtained from the measured Γ_{tot} and Γ_0. Analogous to the $^{171}_{\text{e}}$Yb -$^{173}_{\text{g}}$Yb losses studied previously, the decay coefficients and inelastic scattering lengths are obtained as $\beta_{-1/2,+5/2} = 4.6(1.7) \times 10^{-15}$ cm^{3}s^{-1} and $\beta_{+1/2,+5/2} = 3(1) \times 10^{-15}$ cm^{3}s^{-1}, or equivalently $b_{-1/2,+5/2} = 0.019(7)a_0$ and $b_{+1/2,+5/2} = 0.013(4)a_0$. The error bars of Γ_{in} are relatively large compared to those in $^{171}_{\text{e}}$Yb -$^{173}_{\text{g}}$Yb, because the decay rates of this interorbital interaction are on the same order of magnitude as the one-body decay rates, therefore contributing significantly to the error in Γ_{in}. For some measurements, we even find negative inelastic decay rates, in other words $\Gamma_0 > \Gamma_{\text{tot}}$, which is not expected. Since the inelastic loss rate and one-body loss rates are so similar here, small drifts in the total atom number or clock frequency* can explain this. However, zero is still within two standard deviations for each negative $\Gamma_{\text{in}}(s_{1D})$, so the deviations could simply be statistical in nature. The resulting decay coefficients are nevertheless significantly different from zero.

Table 5.2 shows the measured decay coefficients and inelastic scattering lengths of interorbital interisotope mixtures. Remarkably, the losses of the $^{171}_{\text{g}}$Yb -$^{173}_{\text{e}}$Yb interaction are about 400 times smaller than those of the $^{171}_{\text{e}}$Yb -$^{173}_{\text{g}}$Yb interaction, whereas

---

*Unlike the spectroscopy measurement, no *a posteriori* linear-drift compensation was done here, because the single atom transition was not measured. In principle, it can be done using the interaction peaks, but these peak positions are influenced by both clock drifts and fluctuations in the lattice depths. To avoid this ambiguity, the *a posteriori* drift compensation was not done here.

(a)

(b)
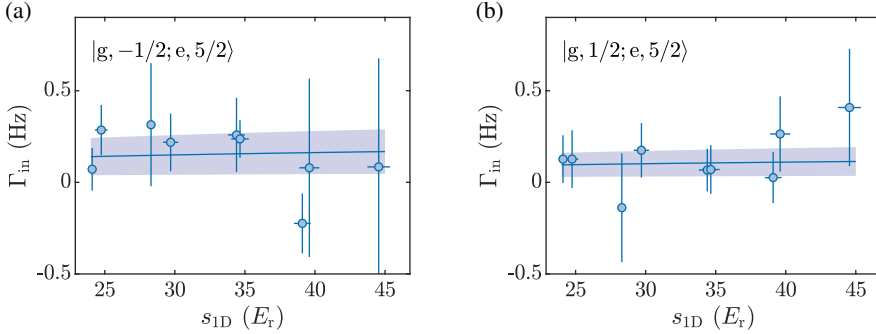
Figure 5.12: Decay rates of the $^{171}_{g}$Yb -$^{173}_{e}$Yb mixture as a function of 1D lattice depth, analogous to Fig. 5.10. Here the data points are single measurements or averaged twice. (a) shows the decay rates of the $|g, -1/2; e, 5/2\rangle$ mixture and (b) shows the decay rates of the $|g, 1/2; e, 5/2\rangle$ mixture. The figure is adapted from the published version [2]. © 2021 American Physical Society.

the elastic scattering lengths are similar (see Table 5.1). Currently, this difference is not understood. Future measurements are needed to exclude the effect of the lattice laser beams. In our experiment, the 1D and 2D lattice are detuned by 160 kHz to ensure these do not interfere. This, however, might lead to single-photon laser-assisted losses or a photo-associative coupling to a higher-lying molecular state, similar to the photo-association (PA) measurements done by Ref. [86]. If the difference is not due to experimental details, the smaller losses in $^{171}_{g}$Yb -$^{173}_{e}$Yb make it the more promising candidate for future quantum simulation measurements.

The inelastic losses of the two spin configurations measured for both interorbital mixtures are not significantly different from each other. However, unlike the elastic interactions, it is not expected that the loss processes can be described solely by the two quantum numbers F_{tot} and M_{tot}*. Therefore, we do not claim SU(2)⊗SU(6) symmetry for the inelastic interactions. Measurements with all twelve spin configurations are needed to draw further-reaching conclusions.

Lastly, we point out that the four decay coefficients here found are similar to other excited-ground state decay coefficients in ytterbium, such as ^{171}Yb [155] and ^{173}Yb [22].

---

* We acknowledge P. Schmelcher for helpful discussions on this topic.

5.1.3   Determination of the *p*-wave Scattering Lengths

With the determination of the elastic and inelastic interactions, the *s*-wave scattering is now fully characterised by the complex scattering length $\tilde{a} = a - ib$. Using the quantum-defect-theory (QDT) model by Ref. [174], $\tilde{a}$ can be used to find several other properties of the interaction. Their single-channel model assumes two particles interact via a Van der Waals (vdW) potential of the form $V(r) \propto -C_6/r^6$, where C_6 is a constant [174]. A complex molecular potential describes the long-range interactions, associated with the elastic interaction, and the short-range losses, associated with the inelastic interaction. This potential is characterised by a dimensionless scattering length s and loss parameter y. Here, $s = a_{\text{bg}}/a_{\text{vdW}}$, where a_{bg} is the background *s*-wave scattering length of the potential and $a_{\text{vdW}} = 2\pi(2\mu C_6/\hbar^2)^{1/4}/\Gamma(1/4)^2$ is the vdW scattering length, where $\Gamma(f)$ is the gamma function of f [174]. The loss parameter is defined such that for $y = 0$ there are no losses, and for $y = 1$ every scattering event leads to complete losses, hence limiting $0 \leq y \leq 1$ [174].

For small momenta $k|\tilde{a}| \ll 1$ and $k a_{\text{vdW}} \ll 1$, the complex *s*-wave scattering length can be rewritten in terms of the two QDT parameters as [174]

$$\frac{\tilde{a}(k)}{a_{\text{vdW}}} = s + y \frac{1 + (1-s)^2}{i + y(1-s)}. \tag{5.10}$$

For excited-ground state Yb molecular potentials, the theoretically calculated $C_6 = 2561(95)\, E_{\text{h}} a_0^6$ [178], where E_{h} is the Hartree energy, leads to a Van der Waals scattering length of $a_{\text{vdW}} = 80.8(7) a_0$. Using this, the QDT parameters are found, yielding $s = -1.0(7)$ and $y = 0.02(1)$ for the $|e, -1/2; g, 5/2\rangle$ state and $s = -1.2(7)$ and $y = 4.0(2.7) \times 10^{-5}$ for the $|g, -1/2; e, 5/2\rangle$ state. The corresponding parameters of the other measured spin configurations do not differ significantly, but are given in Table 5.3 at the end of this chapter for completeness.

The loss parameter y can be written in terms of the short-range reaction probability P_{re} as [177]

$$P_{\text{re}} = \frac{4y^2}{(1+y)^2}, \tag{5.11}$$

which is the probability an atom has an inelastic or reactive collision. Using the previously-found y, we find $P_{\text{re}} = 0.07(4)$ and $P_{\text{re}} = 1.6(1.1) \times 10^{-4}$ for the $|e, -1/2; g, 5/2\rangle$ and $|g, -1/2; e, 5/2\rangle$ states, respectively.

The s and y parameter are furthermore related to the complex *p*-wave scattering length $\tilde{a}_{l=1}$ as [174]

$$\frac{\tilde{a}_{l=1}(k)}{a_{\text{vdW},1}} = -2(a_{\text{vdW}}k)^2 \frac{y + i(s-1)}{ys + i(s-2)}, \tag{5.12}$$

where $a_{\mathrm{vdW},1} = a_{\mathrm{vdW}}\Gamma(1/4)^6/(144\pi^2\Gamma(3/4)^2)$ [174]. Similarly to the s-wave scattering length, $\tilde{a}_{l=1} = a_{l=1} - ib_{l=1}$, where $a_{l=1}$ and $b_{l=1}$ are the elastic and inelastic part of the interaction, respectively, and where the subscript $l = 1$ denotes the partial-wave quantum number of the p-wave interaction [174]. For the $|e, -1/2; g, 5/2\rangle$ and $|g, -1/2; e, 5/2\rangle$ states we find for the elastic p-wave scattering lengths $a_{l=1}/(a_{\mathrm{vdW}}k)^2 = -115(14)a_0$ and $a_{l=1}/(a_{\mathrm{vdW}}k)^2 = -119(12)a_0$, respectively. The inelastic part of the interactions are $b_{l=1}/(a_{\mathrm{vdW}}k)^2 = 1.6(8)a_0$ and $b_{l=1}/(a_{\mathrm{vdW}}k)^2 = 3.9(2.3) \times 10^{-3}a_0$, respectively.

The uncertainties of these estimated parameters are relatively large, which is due to the large uncertainty of a_{gg}. This is currently the limiting factor in the estimation of the p-wave scattering length, so future measurements attempting to reduce the uncertainty should focus on measuring a_{gg} with a higher accuracy. Nevertheless, from these estimations we conclude that, similar to the s-wave scattering, p-wave interactions of interorbital ^{171}Yb-^{173}Yb are attractive at small momenta. Furthermore, the large difference in inelastic scattering lengths of the s-wave interaction is also present in the p-wave interaction.

5.2 Towards a Molecular Potential of e-g Yb$_2$

Together with earlier work [21, 23, 28, 86, 155, 157, 175, 176], the measurement of the interorbital interisotope scattering lengths presented here pave the way towards a better understanding of ^{3}P$_0-^1$S$_0$ state molecular potentials. In the following, a simple mass scaling model is presented, similar to the one presented for ground-ground state Yb interactions presented in Ref. [86].

From the spin-exchange scattering lengths $a_{\mathrm{eg}\pm}$ measured in ^{173}Yb [21, 28, 157], the direct scattering length $a_{\mathrm{eg}0}$ was found*. The same is done for ^{171}Yb using Refs. [23, 155] and our work (see Ref. [2] and Sec. 4.2.3). Furthermore, the excited-ground state interaction in ^{174}Yb was measured [175, 176]. In this way, several interorbital interactions at four different reduced masses are now known. Figure 5.13 shows the scattering lengths as a function of the reduced mass of these interacting pairs.

The simple mass scaling model uses the treatment by Ref. [86]. The elastic s-wave scattering length in the zero-energy limit is given by [86]

$$a = a_{\mathrm{vdW}}(\mu)\left[1 - \tan\left(\Phi(\mu) - \frac{\pi}{8}\right)\right], \tag{5.13}$$

where, as before, the vdW length is given by $a_{\mathrm{vdW}}(\mu) = 2\pi(2\mu C_6/\hbar^2)^{1/4}/\Gamma(1/4)^2$. The

---

* Though the Florence group has measured the spin-exchanging interactions of ^{173}Yb twice [22, 157], only their more accurate measurement [157] is used here.
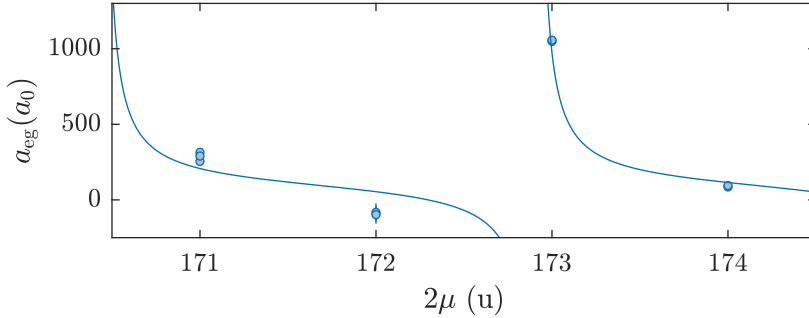
Figure 5.13: Speculative mass scaling model. The data points are the direct interactions as measured by Refs. [21, 23, 28, 86, 155, 157, 175, 176] and our work [2], and the error bars denote the experimental uncertainties. The solid line shows a fit to the data (see text).

semi-classical phase Φ is given by [86]

$$\Phi(\mu) = \frac{\sqrt{2\mu}}{\hbar} \int_{r_0}^{\infty} dr \sqrt{-V(r)}, \tag{5.14}$$

where $V(r) \approx -C_6/r^6$ is the vdW potential (see also Sec. 5.1.3) and r_0 is the classical turning point of the potential [86]. Lastly, the number of bound states N_b of the potential is given by [86]

$$N_b = \text{int}\left(\frac{\Phi}{\pi} - \frac{5}{8}\right) + 1, \tag{5.15}$$

where the function int(f) takes the integer part of f.

In principle the Schrödinger equation with the vdW potential should be solved numerically, as is done in Ref. [86]. Here, a simpler approach is taken, using Eq. 5.13 to fit the direct interactions, where the integral $A = \int_{r_0}^{\infty} dr \sqrt{-V(r)}$ is the only free parameter. Further, the theoretically calculated $C_6 = 2561\, E_h a_0^6$ [178] is used. The fit is shown in Fig. 5.13 and yields $A = 6.1043(4) \times 10^{-20} \sqrt{J}$m. This results in a number of bound states $N_b = 139$ at $2\mu = 172$, which is almost twice as large as the 71 bound states of the ground-ground state potential [86]. This could be explained by the larger expected depth of the interorbital potentials [179]. The divergence of the fit just below $2\mu = 173$, indicates the presence of a weakly bound state close to the continuum. Furthermore, assuming $V(r) = -C_6/r^6$ this suggest the classical turning point of the

potential is $r_0 = 13.5a_0$. However, these results should be treated with caution, since the fit has many similar local minima for a different number of bound states. Since the integral parameter A can be varied by about 2×10^{-21} $\sqrt{J}$m while still yielding satisfactory fits with different N_b, we estimate that the uncertainty is at least 5%. A more detailed description, which also takes into account the energies of the least bound states [28, 86, 155, 157], is required to give a better description of the measured scattering lengths, which is beyond the scope of this work.

5.3 Three-Component Fermi-Fermi Mixtures

In addition to the spin-polarised Fermi-Fermi mixtures studied before, measurements were done on interorbital Fermi-Fermi mixtures with multiple spin components. In such multi-spin Fermi-Fermi mixtures the competition of different interactions can lead to the emergence of interesting quantum phases [25, 87], or multi-body interactions [180].

To this end, a mixture of spin-balanced ^{171}Yb and spin-polarised ^{173}Yb in the ground state was loaded into a 'magic 'lattice with $s_{1D} = 40E_r$ and $s_{2D} = 25E_r$ at a magnetic field of $B = 8.8$ G. A clock π pulse of length 2.3 ms was used, except for the $|+\rangle$ and $|-\rangle$ spin-exchange peaks of ^{171}Yb for which the pulse length was adapted to enable maximum excitation (similar to Sec. 4.2.1). Figure 5.14 shows the resulting spectrum. The two highest peaks at about ± 2.3 kHz are due to single excited ^{171}Yb atoms in the $m_F = \mp 1/2$ states. Based on the measurements presented in Sec. 4.2.2, the resonances of the interorbital spin-exchanging interactions were known, allowing for the identification of the peaks at about 1 kHz and 5.8 kHz as the $|+\rangle$ and $|-\rangle$ state peaks, respectively. The remaining two peaks were identified as the interorbital interisotope interaction peaks based on the interaction shifts measured in Sec. 5.1.1.

Considering the peak heights teaches us something about the occupations in the lattice prior to the clock excitation. The total peak height of the single-atom transitions indicates that about 53% of all ^{171}Yb atoms are on singly-occupied sites. The four interacting states all have a maximum excitation of about 3%. Hence, at least 6% of the initial lattice sites consisted of ground-ground state ^{171}Yb (see also Sec. 4.2.3). Another 6% of the initial lattice sites consisted of a single ^{171}Yb atom in the $m_F = +1/2$ or $m_F = -1/2$ state with a single ^{173}Yb atom. However, the total peak height is not unity. This can in part be explained by decoherence of the interaction peaks, and potential imperfections in setting the clock time. Due to the finite decoherence during the clock excitation, the real occupations of the interacting states are a few percent higher.

Triply-occupied sites, in the following referred to as *triplons*, consisting of two ^{171}Yb atoms and one ^{173}Yb atom, cannot explain the non-unity excitation, as is ex-

Figure 5.14: Clock spectroscopy of ^{171}Yb in a mixture of spin-balanced ^{171}Yb and spin-polarised ^{173}Yb. The detuning is with respect to the degenerate single-atom resonance. The data points are three times averaged. The solid line shows a fit with four sinc^2 and two Lorentzian functions as a guide to the eye, where the shaded area denotes its 95% confidence interval. The states corresponding peaks is denoted in the kets. The figure is adapted from the published version [2]. © 2021 American Physical Society.

plained in the following. In the initial system, a triplon is in the state $|gg\rangle \otimes |g_{173}\rangle$, where $|gg\rangle$ is the spin-anti-symmetric ^{171}Yb ground-ground state as defined in Sec. 4.1. Neglecting multi-body effects, the energy of the state is $U_{ggg} = 2U_{gg}^{inter} + U_{gg}^{intra} \propto -1.16(8) \times 10^3 a_0$, where the 'inter' and 'intra' superscripts denote the ^{171}Yb–^{173}Yb interisotope and ^{171}Yb intraisotope interactions, respectively. Clock excitation of a ^{171}Yb atom brings the triplon into the $|\pm\rangle \otimes |g_{173}\rangle$ state, which has an energy of $U_{\pm g} = E_{\pm}(B) + U_{gg}^{inter} + U_{eg}^{inter}$. The expected energy shift is hence $\Delta U_{\pm g} = E_{\pm}(B) + \Delta U_{eg}^{inter} - U_{gg}^{intra}$, which is 6.2 kHz and 11 kHz for the $|+\rangle \otimes |g_{173}\rangle$ and $|-\rangle \otimes |g_{173}\rangle$ states, respectively, for the magnetic field and lattice depths used here. Though the $|-\rangle \otimes |g_{173}\rangle$ state is outside of the scanned range, we do not observe any excitation at 6.2 kHz. This is surprising, since the triplon ground-state interactions are large and attractive and hence naively a large triplon fraction is expected.

To understand the occupation numbers present in the lattice, a grand-canonical-ensemble model was studied, which has been applied successfully by Ref. [181] to understand double occupancy (doublons) in repulsively-interacting ^{40}K quantum gases in an optical lattice. The model was provided courtesy of H. Moritz, studied and modified by N. Pintul and supervised by the author. The results of balanced two-species systems are described in detail in Ref. [142]. Though the model provides internally
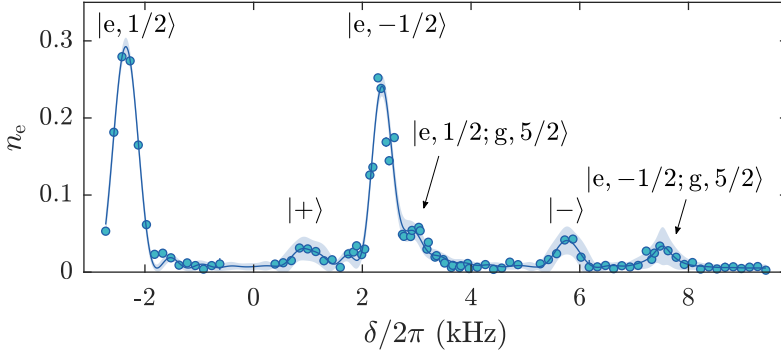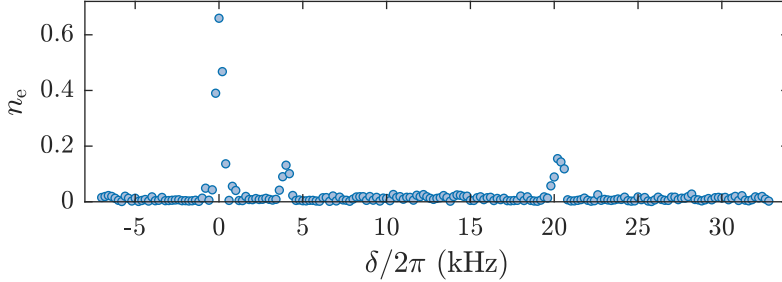
Figure 5.15: Clock spectroscopy of ^{173}Yb in a mixture of spin-balanced ^{171}Yb and spin-polarised ^{173}Yb. The lattice depths was set to $s_{1D} = 30E_r$ and $s_{2D} = 17E_r$. The three peaks, from left to right, are due to single-atom excitations, interorbital interisotope interactions and the single-atom blue sideband.

consistent predictions, the expected doublon fractions are consistently different from experiments. For ground-ground state ^{171}Yb with attractive interactions of $-3a_0$ [86], doublon fractions of over 0.9 are expected [142], whereas experimentally about 0.23 was measured (see Sec. 4.2.3). Based on this model, a sample with large attractive interactions, such as for $^{171}_g$Yb -$^{173}_g$Yb, is expected to have doublon fractions indistinguishable from unity, whereas we observe single-atom fractions of more than 0.4 (see Sec. 5.1.1). The model was therefore rejected for our experiments and was not extended to three-component samples. The fact that the measured doublon fractions of about 6% in the three-component Fermi-Fermi mixtures are so small, yet the same for vastly different ground-state interactions, suggests that energy considerations are not enough to explain the occupation fractions. The dominant processes leading to these unexpected occupations are currently not understood.

Three-body interactions, so far neglected, cause interactions shifts different from the summed two-body interaction shifts [180]. Judging by the three-body interactions in ^{87}Sr [180], the shift is not expected to bring the triplons out of the scanned range. To rule out the possibility of the triplon peak overlapping with the $|-\rangle$ resonance at 5.8 kHz, we repeat the three-component measurement with the same initial state. Here, however, the spin-polarised ^{173}Yb atoms are excited, to prevent the excitation of interorbital spin-exchange states. Figure 5.15 shows the resulting spectrum of a spin-balanced ^{171}Yb spin-polarised ^{173}Yb mixture, exciting the latter isotope. The spectrum displays three peaks, the single-atom peak at $\delta = 0$, the interisotope interorbital interaction

peak* at 4 kHz, and the single-atom blue sideband at 20 kHz. Neglecting three-body interactions, the excited triplon state is given by $|gg\rangle \otimes |e_{173}\rangle$ and the interaction peak is expected at $\Delta U_{\text{gge}} = 2\Delta U_{\text{ge}}^{\text{inter}} \approx 8$ kHz. However, the triplon peak is not observed.

The unknown processes that limit double occupation possibly further suppress triple occupation. Furthermore, three-body recombination [180, 182] prior to lattice loading can lead to suppression of initial triply-occupied sites. Additional experimental work is needed for a better understanding.

5.4   Conclusion & Outlook

To summarise, we have characterised interorbital s-wave interactions in ^{171}Yb-^{173}Yb Fermi-Fermi mixtures, summarised in Tables 5.1 and 5.2. The elastic interactions were found to be small and attractive at $\bar{a}_{\text{eg}} = -8(6) \times 10^1\, a_0$ and $\bar{a}_{\text{ge}} = -1.0(6) \times 10^2\, a_0$. The SU(2)⊗SU(6) symmetry of the elastic interactions was directly observed, well within 1% accuracy. Further, Rabi oscillations were measured on both interorbital mixtures, which confirmed that the coupling of interacting interisotope pairs is the same as it is for single atoms. The elastic interactions were shown to be independent of the magnetic field within 1%, as is expected. Furthermore, we have measured losses of two spin configurations to determine the inelastic part of the interactions. Remarkably, we found that the decay coefficient of $^{171}_{\text{g}}$Yb -$^{173}_{\text{e}}$Yb is about 400 times smaller than that of $^{171}_{\text{e}}$Yb -$^{173}_{\text{g}}$Yb. Using the elastic and inelastic part of the s-wave interactions and the quantum defect theory model of Ref. [174], the p-wave scattering parameters were estimated, as summarised in Table 5.3. A speculative molecular potential model was fitted and shown in Sec. 5.2. Lastly, measurements of three-component mixtures were done, but no triply-occupied sites were found.

Future measurements could aim at observing the breaking of the SU(2)⊗SU(6) symmetry, which is expected to occur on the scale below 10^{-3} [25]. If symmetry breaking is observed, it is interesting to measure all twelve possible spin configurations. This can be done in the current setup, using lower-intensity and longer clock pulses to reduce the spectroscopic line widths and increase the accuracy.

To completely characterise the inelastic interactions in these interisotope mixtures, losses of all twelve possible spin configurations should be measured. Furthermore, it should be ruled out that the large differences in decay coefficients between both interorbital mixtures are caused by experimental factors. The lattice laser might cause decays, which can be studied while varying the detuning between the 1D and 2D lattice.

---

* Since both m_F states of ^{171}Yb are present in the system, in reality this peak corresponds to the sum of the $|g, -1/2; e, 5/2\rangle$ and $|g, +1/2; e, 5/2\rangle$ peaks, which overlap due to the SU(2)⊗SU(6) symmetry of the interaction.

If the large difference in inelastic interactions persists, we expect these measurements provide an interesting benchmark for future theoretical models incorporating reactive processes.

The measurements presented here are expected to contribute to the understanding of $^1S_0-^3P_0$ Yb molecules. A mass-scaling model has been applied successfully for ground-ground state Yb interactions [86], and a similar model might be found for excited-ground state Yb, along with previous measurements in different isotopes [21–23, 28, 29, 155, 157, 175, 176]. However, the measurements presented here can be especially interesting because of the difference in $\bar{a}_{eg}$ and $\bar{a}_{ge}$ at the same reduced mass. Therefore, this measurement can be a useful benchmark for higher-order corrections to existing excited-ground-state molecular-potential models [178, 179]. To reduce the uncertainty in the absolute value of the interisotope interorbital interactions, however, a_{gg} should be measured more accurately. Additionally, by changing the clock beam to dual-frequency operation, the interisotope excited-excited state interactions can be measured.

To learn more about the quantum phases in three-component Fermi-Fermi mixtures, the occupation ratios have to be understood first. Once a better understanding is obtained, experiments can be done studying the competition of the different interactions, which can lead to interesting quantum phases [25, 87] or multi-body interactions [180].

Furthermore, the Efimov spectrum was calculated for three-body bound states of two ground-state ^{171}Yb and one ground-state ^{173}Yb atom [183]. Once the triple occupation in the lattice is increased, the interorbital interisotope mixtures can be an interesting platform as a comparison to ground-state three-body bound states.

Finally, the high symmetry SU(2)⊗SU($\mathcal{N} > 2$) is expected to exhibit exotic d-wave superfluidity [93]. Additionally, the interorbital ^{171}Yb-^{173}Yb mixture could be a favourable platform to observe two-flavour superfluid symmetry-locking (TFSSL) phases [94, 95], because it is deeper in the TFSSL phase than the proposed $^{171}_g$Yb - $^{173}_g$Yb mixtures. For these ground-ground-state mixtures, a critical temperature of $0.1T_F$ is estimated [95], yet the constraints deeper in the TFSSL phase are likely to be less stringent. Due to its small inelastic interactions, the $^{171}_g$Yb - $^{173}_e$Yb mixture is likely to be superior over $^{171}_e$Yb - $^{173}_g$Yb.

Table 5.3: Summary of the quantum defect theory parameters and resulting p-wave scattering lengths.

Quantity	$^{171}_{\mathrm{e}}\mathrm{Yb}$ - $^{173}_{\mathrm{g}}\mathrm{Yb}$	$^{171}_{\mathrm{g}}\mathrm{Yb}$ - $^{173}_{\mathrm{e}}\mathrm{Yb}$
$s_{-1/2,+5/2}$	$-1.0(7)$	$-1.2(7)$
$y_{-1/2,+5/2}$	$0.02(1)$	$4.0(2.7) \times 10^{-5}$
P_{re}	$0.07(4)$	$1.6(1.1) \times 10^{-4}$
$a_{l=1}/(a_{\mathrm{vdW}}k)^2$	$-115(14)a_0$	$-119(12)a_0$
$b_{l=1}/(a_{\mathrm{vdW}}k)^2$	$1.6(8)a_0$	$3.9(2.3) \times 10^{-3}a_0$
$s_{-1/2,+3/2}$	$-1.0(7)$	-
$y_{-1/2,+3/2}$	$0.02(1)$	-
P_{re}	$0.07(4)$	-
$a_{l=1}/(a_{\mathrm{vdW}}k)^2$	$-115(14)a_0$	-
$b_{l=1}/(a_{\mathrm{vdW}}k)^2$	$1.7(8)a_0$	-
$s_{+1/2,+5/2}$	-	$-1.2(7)$
$y_{+1/2,+5/2}$	-	$2.8(1.8) \times 10^{-5}$
P_{re}	-	$1.1(7) \times 10^{-4}$
$a_{l=1}/(a_{\mathrm{vdW}}k)^2$	-	$-118(13)a_0$
$b_{l=1}/(a_{\mathrm{vdW}}k)^2$	-	$2.7(1.5) \times 10^{-3}a_0$

Chapter 6

Dynamics in the Dissipative Fermi-Hubbard Model

Dissipation generally causes quantum systems to lose the coherent properties that make them interesting, and is hence often considered as the main obstacle to investigating and using quantum systems. Since quantum experiments are inevitably coupled to the environment, the study of dissipative phenomena has come to the forefront of physics. Whereas often experiments attempt to study quantum effects on timescales which are short compared to decoherence times, proposals were made utilising dissipation for quantum state engineering [96–100]. Predictions have underlined the usefulness of dissipation in entropy transfer [101] and correlations measurements [102]. Studying dissipation within ultracold quantum gases is of particular interest because of the high degree of tunability of quantum gases, for instance controlling the coupling to an external bath [103, 104]. One-body dissipation has been studied in numerous systems, for instance by irradiating a ^{87}Rb BEC with an electron beam [105, 106], near-resonant photon scattering [107, 108], or imaging-induced losses [109]. Two-body losses were studied using inelastic collisions in bosonic ^{87}Rb Feshbach-molecules in 1D tubes, where an inhibition of losses was observed and attributed to the build-up of correlations [110–112]. Polar fermionic KRb molecules showed a similar loss suppression [114, 115]. Furthermore, photo-association on the $^1S_0 \rightarrow {}^3P_1$ transition was used to tune the inelastic loss rate of ^{174}Yb atoms and observe the effect of driven-dissipation on the Mott-to-superfluid crossover [116].

More recently, tunable dissipation has been studied experimentally within a synthetic lattice of momentum states [117], and the dissipative Bose-Hubbard model was

studied using the $^3P_2$ state of ^{174}Yb [113]. Recent proposals have among others suggested using dissipation to study dynamical parity-time symmetry breaking [119] and the effect of dissipation on topological Bose-Mott insulators [120]. Furthermore, rate equations were found for the dissipative Bose-Hubbard model in a beyond-mean-field treatment [121], and a study on the weakly-dissipative Fermi-Hubbard model highlighted the connection between the spin conservation and the dynamics [123].

The main motivation of this work is the proposal by Ref. [99], where it was predicted that fermionic 1D systems with SU(2)-symmetric s-wave interactions form highly-entangled Dicke states after some transient time. A Dicke state [124] is a many-body state where the spin part of the wavefunction is fully symmetric, whereas the spatial part of the wavefunction is anti-symmetric. The symmetric spin wavefunction has a minimal uncertainty ΔS_z which acts as a type of spin-squeezing, and hence has optimal spectrographic properties allowing one to break the standard quantum limit and reach the Heisenberg limit [99]. As we will show in the following, our work is compatible with the dynamic formation of a highly-entangled Dicke state.

Additionally, Ref. [118] pointed out that these dissipative SU(2)-symmetric 1D systems exhibit a dynamical sign-reversal of magnetic correlations. This is because the many-body states prone to losses are the lowest energy states while the spin-symmetric state has the highest energy of the initially uncorrelated system [118]. Since the latter state is unaffected by the losses, the highest energy state is stabilised over time, generating a maximum energy state similar to negative-temperature states in closed systems [118, 184, 185]. Furthermore, in a more recent work the dissipative Bose- and Fermi-Hubbard models were solved analytically [122].

The work in this chapter was supervised by K. Sengstock & C. Becker. The data was taken by B. Hundt, A. Kochanke and T. Ponath. A first version of the analysis was done by B. Hundt [128], and the analysis in this chapter and of the publication [1] was performed by the author. Numerical simulations were carried out by L. Freystatzky under supervision of L. Mathey. The final interpretation was done by the author in collaboration with L. Freystatzky, B. Abeln, M. Diem, B. Santra, L. Mathey, K. Sengstock and C. Becker. The work presented in this chapter was published in Ref. [1].

6.1   State Preparation

For reasons that will become apparent later, the desired initial state is a Mott insulator [186] of $^3P_0$ excited state ^{173}Yb atoms. To transfer ground-state atoms to the excited state, a so-called *rapid adiabatic passage* is used, which is more experimentally robust than π-pulse excitation, as explained in the following.

Furthermore, to study the effect of many-body spin correlations, optical pumping

Table 6.1: Relative spin-state populations $N_{m_F} / \sum_{m_F} N_{m_F}$ for six-spin, two-spin or spin-polarised samples of ^{173}Yb.[1]

Spin Mixture	m_F					
	-5/2	-3/2	-1/2	+1/2	+3/2	+5/2
Six	0.18(1)	0.208(4)	0.185(5)	0.161(2)	0.137(3)	0.130(8)
Two	0.46(3)	0.45(3)	0.07(2)	< 0.01	0.02(1)	< 0.01
Spin-polarised	0.93(7)	0.06(6)	< 0.01	< 0.01	< 0.01	< 0.01

is used to create atomic samples with one, two or six m_F states. Here, the realisation of optical pumping is slightly different from the updated implementation described in Sec. 2.3.1. Formerly, instead of the 3D-MOT beams a dedicated laser beam was used, prior to evaporation with the green dipole trap [128, 129]. Table 6.1 shows the relative spin-state populations $N_{m_F} / \sum_{m_F} N_{m_F}$ for different spin configurations, as obtained from an analysis using an optical Stern-Gerlach method as described in Sec. 2.3.2.

6.1.1 Rapid Adiabatic Passage

A rapid adiabatic passage (RAP) [158, 187] is an alternative way of transferring ground state atoms to the excited state. Instead of exciting the atoms on resonance with a π pulse, one starts far-detuned and sweeps over the resonance. In the (g, e) basis, the time-dependent Hamiltonian $\hat{\mathcal{H}}_{\mathrm{RAP}}$ describing this two-level system is given by [187]

$$\hat{\mathcal{H}}_{\mathrm{RAP}}(t) = \frac{\hbar}{2} \begin{pmatrix} \delta(t) & \Omega_0(t) \\ \Omega_0(t) & -\delta(t) \end{pmatrix}, \tag{6.1}$$

where the detuning and Rabi frequency were assumed to be real. The laser coupling mixes the pure $|g\rangle$ and $|e\rangle$ states, resulting in the eigenstates $\Phi_\pm$ [187]

$$|\Phi_+\rangle = \sin\Theta(t)|g\rangle + \cos\Theta(t)|e\rangle \tag{6.2}$$
$$|\Phi_-\rangle = \cos\Theta(t)|g\rangle - \sin\Theta(t)|e\rangle, \tag{6.3}$$

where $\Theta(t) = \frac{1}{2}\arctan[\Omega_0(t)/\delta(t)]$ is the mixing angle modulo π. These eigenstates are referred to as the *dressed states*, and have energies $E_\pm$ [187]

$$E_\pm = \pm\frac{\hbar}{2} \sqrt{\delta(t)^2 + \Omega_0(t)^2}. \tag{6.4}$$
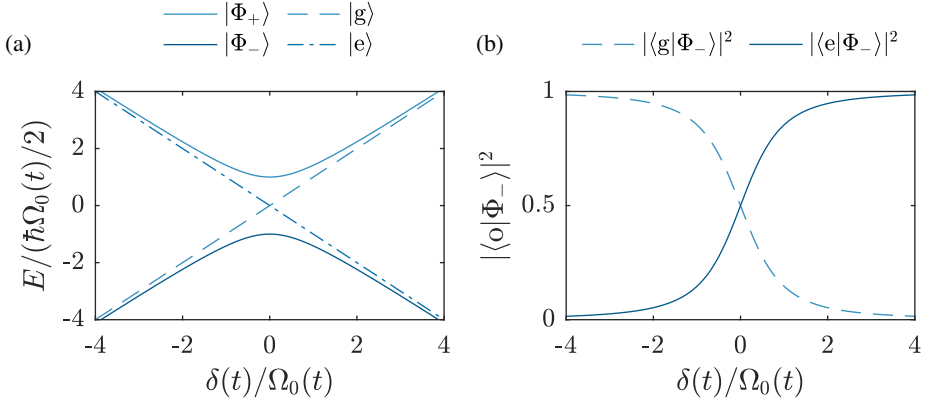
Figure 6.1: (a) Energies in units of coupling energy during a rapid adiabatic passage as a function of dimensionless detuning. The lines indicate different states (see legend). The energy splitting between the $|\Phi_+\rangle$ and $|\Phi_-\rangle$ states is $\hbar\Omega_0(t)$. (b) State occupations $|\langle o|\Phi_-\rangle|^2$ of the orbital $o \in [g, e]$ during a RAP as a function of dimensionless detuning. The solid and dashed lines indicate the excited and ground state occupation (see legend).

Figure 6.1a shows the energies as a function of dimensionless detuning. The dashed and dash-dotted lines indicate the energies of the ground and excited states, respectively. The solid lines indicate the energies of the dressed states, and the coupling gives rise to an avoided crossing, resulting in an energy splitting between the $|\Phi_+\rangle$ and $|\Phi_-\rangle$ states of $\hbar\Omega_0$ on resonance.

Figure 6.1b shows the probability of measuring the Φ_- dressed state in the ground or excited state as a function of dimensionless detuning. The working principle of RAP can now be understood as follows. Consider a single ground state atom illuminated by a clock laser beam with a frequency far below resonance $\delta \ll -\Omega_0$, where $|\Phi_-\rangle \approx |g\rangle$. Sweeping the laser frequency to detunings much larger than resonance $\delta \gg \Omega_0$ leads to a complete transfer to the excited state, as there $|\Phi_-\rangle \approx |e\rangle$.

When only transfer to the excited state is required, this method is advantageous over π-pulse excitation because it is insensitive to small experimental variations in the resonance, such as varying resonance frequencies over the sample or small changes in Ω_0 due to fluctuations in the the laser frequency and power. For the same reason, RAP is not useful for high-resolution spectroscopy.

However, to completely transfer ground-state atoms to the excited state, the adia-

batic condition [187]

$$\frac{1}{2}\left|\frac{\mathrm{d}\Omega_0(t)}{\mathrm{d}t}\delta(t) - \Omega_0\frac{\mathrm{d}\delta(t)}{\mathrm{d}t}\right| \ll \left(\delta(t)^2 + \Omega_0^2\right)^{3/2} \tag{6.5}$$

must be fulfilled. Assuming a constant Rabi coupling, in other words, a constant clock beam intensity, and a linear frequency sweep this reduces to a sweep time t_s of [129]

$$t_s \gg \frac{|\delta(t)\Omega_0|}{\left(\delta(t)^2 + \Omega_0^2\right)^{3/2}}, \tag{6.6}$$

where the right-hand side has a maximum of about $0.38/\Omega_0$ at $\delta \approx \pm 0.72\Omega_0$, which can be used to find an appropriate sweep time. The condition applied to our system is verified in detail in Refs. [128, 129] and the settings were adapted to fulfil the condition.

To characterise the efficiency of the RAP, measurements were performed on a spin-polarised gas of ^{173}Yb atoms. The atoms were loaded into a deep lattice of $s_{1D} = 50E_r$ and $s_{1D} = 42E_r$. The RAP is initiated by switching on the clock beam with a bare Rabi frequency $\Omega_0/2\pi \approx 3.8\,\mathrm{kHz}$ and initial detuning $\delta/2\pi = -50\,\mathrm{kHz}$ with respect to the
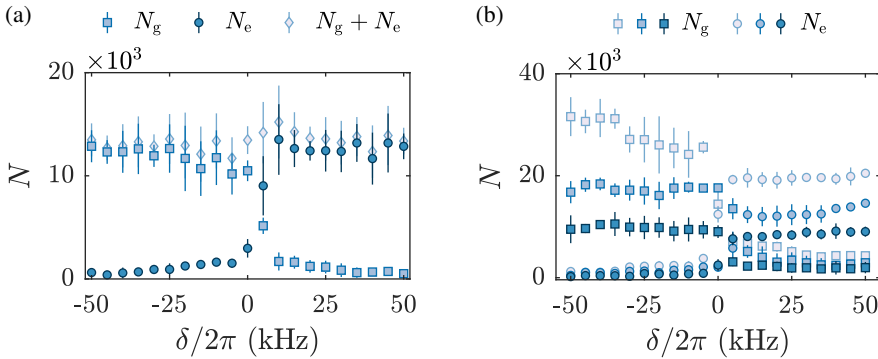
Figure 6.2: Atom numbers during a 20 ms RAP as a function of detuning. The different colours and markers indicate the orbital states (see legend). (a) shows a RAP of a spin-polarized sample. The data is five times averaged and the error bars show the standard deviations. (b) shows a RAP of three six-spin mixtures with different initial ground-state atom numbers (indicated by the colours). The data is four times averaged and the error bars show the standard deviations. The figure is adapted from the published version [1]. © IOP Publishing. Reproduced with permission. All rights reserved.

clock transition. The clock frequency is then swept to $\delta/2\pi = 50\,\mathrm{kHz}$ in $20\,\mathrm{ms}$. To characterise the transfer efficiency, the sweep is interrupted at different detunings and the atom numbers in both states are measured, shown in Fig. 6.2a. A close-to-unity transfer of atoms in the ground state to the excited state is observed.

Figure 6.2b shows an analogous characterisation of the RAP efficiency of six-spin component samples, here for three different initial atom numbers. Though in all cases some atoms are lost during the transfer, this effect is largest for large initial atom numbers. We attribute this to the build up of a small band-insulating core, which increases for increasing atom number. Because the RAP also excites both atoms on double-occupied sites, a fraction of the atoms is transferred to the $|ee\rangle$ state, which is subject to strong losses on a timescale of $2\pi/\Gamma_{ee} \approx 0.6\,\mathrm{ms}$. Since this is much shorter than the sweep time, the band-insulating core is depleted before the end of the RAP.

6.2   The Dissipative Fermi-Hubbard Model

To study a system with a dissipative coupling to some bath, a master equation is typically used [99, 102, 111, 118, 188, 189]. Using this approach, it was shown that SU(2)-symmetric s-wave-interacting fermions with two-body losses* decay to a finite remaining atom number, forming a Dicke state, since these states are dark to two-body losses [99]. Here, however, a simplified model [111, 114, 115] is used get an understanding of the dynamics of our observable, the number of excited-state atoms N_e.

Three energy scales characterise the 1D dissipative Fermi-Hubbard model, the tunnelling J, the elastic on-site interaction U_{ee} and the on-site loss $\hbar\Gamma_{ee}$. The elastic interaction U_{ee} obeys Eq. 4.14 and scales with $a_{ee} = 306(11)a_0$ [21, 86], while Γ_{ee} is related to $\beta_{ee} = 2.2(6) \times 10^{-11}\,\mathrm{cm^3 s^{-1}}$ [21] via Eq. 5.8. The energy scheme in a two-well picture is shown in Fig. 6.3a. If an atom tunnels to a neighbouring site with an atom with a different spin state, the energy increases by U_{ee}. These doubly-occupied sites (doublons) are subject to two-body losses with a rate of Γ_{ee}. In the case of strong elastic and inelastic interactions $J \ll U_{ee}, \hbar\Gamma_{ee}$, the tunnelling can be integrated out, yielding an effective loss rate Γ_{eff} [1, 111, 114, 115]

$$\Gamma_{eff} = 4\,\frac{J^2}{\hbar U_{ee}}\left(\frac{U_{ee}/\hbar\Gamma_{ee}}{1 + 4(U_{ee}/\hbar\Gamma_{ee})^2}\right), \tag{6.7}$$

resulting in an effective model as depicted in Fig. 6.3b. The effective loss rate as a function of the decay strength $\hbar\Gamma_{ee}/U_{ee}$ is shown in Fig. 6.3c, where $t_{se} = \hbar U_{ee}/J^2$ is

---

* The interactions are also required to be purely s-wave in nature, which is easily satisfied in the ultracold regime used here. The prediction is expected to hold already at non-degenerate temperatures below $1\,\mu\mathrm{K}$ [99].
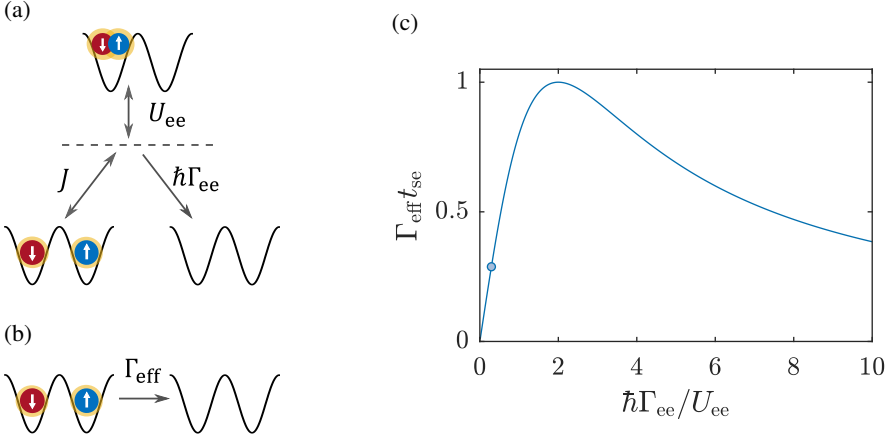
Figure 6.3: (a) Energy scheme of the two-well dissipative Fermi-Hubbard model. The relevant energies are given by the tunnelling J, the elastic interaction energy U_{ee} and the inelastic interaction energy $\hbar\Gamma_{ee}$. (b) Schematic of the effective two-level system assuming $J \ll U_{ee}, \hbar\Gamma_{ee}$. The two states are coupled with a rate of Γ_{eff}. (c) Dimensionless effective loss rate as a function of decay strength $\hbar\Gamma_{ee}/U_{ee}$. The point indicates the decay strength $\hbar\Gamma_{ee}/U_{ee} \approx 0.29$ of ^{173}Yb. The figure is adapted from the published version [1]. © IOP Publishing. Reproduced with permission. All rights reserved.

the superexchange time. The superexchange time is the time for the virtual process that neighbouring atoms with different spins undergo, whereby the spin of the neighbouring atoms is exchanged. There are two regions for which Γ_{eff} is small. For $U_{ee} \gg \hbar\Gamma_{ee}$, losses are inhibited by Mott-insulator-like suppression of doublons. For $U_{ee} \ll \hbar\Gamma_{ee}$, losses are suppressed by quantum-Zeno-like physics, where the strong losses act as a continuous measurement of double occupancy. In Ref. [116], the decay strength was tuned and the characteristic shape of Γ_{eff} was reproduced by variable photo-associative losses of ^{174}Yb bosons in a 3D lattice. However, in our experimental implementation with excited ^{173}Yb atoms, the decay strength is fixed at $\hbar\Gamma_{ee}/U_{ee} \approx 0.29(8)$ [21, 86]. For ^{171}Yb it is 0.19(8) [155], whereas for ^{87}Sr it is 0.26(16) [20], hence all approximately probing the same Γ_{eff}.

In this simplified model, the excited-state atom number N_e is governed by the dif-

ferential equation [1, 111]

$$\frac{dN_e(t)}{dt} = -\mathcal{P}_{\mathcal{N}} \frac{\kappa}{N_{e,0}} N_e(t)^2, \tag{6.8}$$

where $N_{e,0}$ is the initial atom number and $\mathcal{P}_{\mathcal{N}} = (\mathcal{N} - 1)/\mathcal{N}$ is the probability that an atom has a nearest-neighbour atom with a different spin, assuming $\mathcal{N}$ different m_F states and unitary filling, derived in Refs. [1, 129]. The loss coefficient κ is given by [1, 114]

$$\kappa = 4 q \Gamma_{\text{eff}} g^{(2)} \eta_0, \tag{6.9}$$

where $q = 2$ is the number of nearest neighbours for the 1D lattice, η_0 is the initial filling of the lattice, which is unity for a Mott insulator, and $g^{(2)}$ is the nearest-neighbour correlation function, which for $\mathcal{N} = 2$ spin states takes the form [1, 102]

$$g^{(2)} = \frac{1}{N_{e,\text{tot}} - 1} \sum_{\langle ij \rangle} \frac{\left\langle \hat{n}_i \hat{n}_j - 4\hat{\mathbf{S}}_i \cdot \hat{\mathbf{S}}_j / \hbar^2 \right\rangle}{\langle \hat{n}_i \rangle \langle \hat{n}_j \rangle}, \tag{6.10}$$

where $N_{e,\text{tot}}$ is the total atom number in the 1D lattice tube, $\hat{n}_i$ is the number operator and $\hat{\mathbf{S}}_i$ is the spin operator for an atom on site i. The summation goes over all nearest neighbours $\langle ij \rangle$. A generalised nearest-neighbour correlation function for any $\mathcal{N} \geq 2$ was defined as [1]

$$g^{(2)} = \frac{1}{N_{e,\text{tot}} - 1} \sum_{\langle ij \rangle} \sum_{\sigma \neq \sigma'} \frac{\left\langle \hat{n}_{i\sigma} \hat{n}_{j\sigma'} + \hat{n}_{i\sigma'} \hat{n}_{j\sigma} - \hat{c}_{i\sigma'}^\dagger \hat{c}_{j\sigma'}^\dagger \hat{c}_{i\sigma} \hat{c}_{j\sigma'} - \hat{c}_{i\sigma}^\dagger \hat{c}_{j\sigma'}^\dagger \hat{c}_{i\sigma'} \hat{c}_{j\sigma} \right\rangle}{\langle \hat{n}_i \rangle \langle \hat{n}_j \rangle}, \tag{6.11}$$

where $\hat{c}_{i\sigma}$ and $\hat{c}_{i\sigma'}^\dagger$ are the fermionic annihilation and creation operators for site i, respectively, and where $\sigma \in [-m_F, -m_F + 1, \ldots, m_F]$ denotes the spin state. In this simplified model, the observable $N_e(t)$ is thus related to the effective loss rate and the nearest-neighbour correlation function.

Figure 6.4 shows a schematic of various possible $\mathcal{N} = 2$ atomic configurations in the lattice to provide an intuition for $g^{(2)}$. Three configurations exhibit $g^{(2)} = 0$, shown in Fig. 6.4a. A sample without nearest neighbours trivially has vanishing nearest-neighbour correlation function. A ferromagnetic many-body state, where all atoms have the same spin, also has $g^{(2)} = 0$ as the density and spin part of the numerator of Eq. 6.10 cancel out. A Dicke state, the final state of the dissipative Fermi-Hubbard model as predicted by Ref. [99], also exhibits $g^{(2)} = 0$, which is derived in App. B. However, a state without spin-correlations, as depicted in Fig. 6.4b, has $g^{(2)} = 1$. A Néel state, where the spin is alternately up or down, has $g^{(2)} = 2$. A quantum antiferromagnetic state (not shown in the figure), which has a fully anti-symmetric spin wave function, also has $g^{(2)} = 2$.
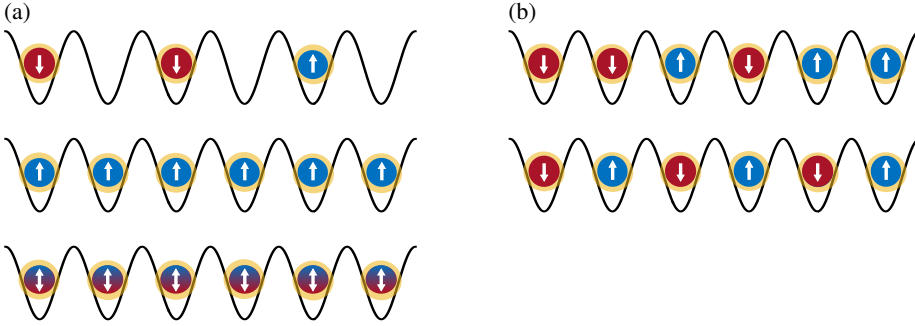
Figure 6.4: Exemplary atom configurations of a two-spin mixture in a lattice. The solid lines show the optical lattice potential. Atoms are represented by the discs, where the spin state is denoted by the colour and arrow. The yellow circle around the discs denote the atoms are in the excited state. (a) Configurations with $g^{(2)} = 0$. (top) a state without nearest neighbours, (centre) a ferromagnetic state, (bottom) a sketch of a highly-entangled Dicke state. (b) Configurations (top) of a state without spin correlations such that $g^{(2)} = 1$ and (bottom) of a Néel state with $g^{(2)} = 2$. The figure is adapted from the published version [1]. © IOP Publishing. Reproduced with permission. All rights reserved.

The Dicke state [99, 124] is a highly-entangled many-body state with a fully symmetric spin wave function. This results in a maximal total spin $S_{max} = N/2$ and minimal uncertainty ΔS_z, as depicted in Fig. 6.5 on a generalised Bloch sphere. The minimal uncertainty can be understood as a type of spin-squeezing, which results in optimal metrological properties [99, 190, 191]. Due to the fermionic anti-symmetry requirement of the many-body state, it also has a fully anti-symmetric spatial wavefunction, and is therefore a dark state with respect to two-body s-wave losses [99].

The formation of these highly-entangled Dicke states via dissipation can now be understood in the following way. Any many-body state can be written as a superposition of a Dicke state and other states. One of the main results of Ref. [99] is that in 1D, only Dicke states have this anti-symmetric spatial wave function, and hence all other states decay on a finite timescale. This provides an alternative, more comprehensive, picture to the build-up of nearest neighbour correlations. For an uncorrelated state, it was shown that the final atom number N_∞ depends only on the initial atom number N_0,
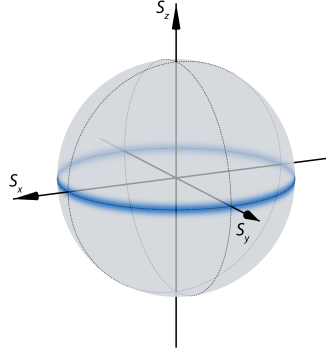
Figure 6.5: Schematic representation of a Dicke state on a generalised Bloch sphere. The blue ring depicts the Dicke state and is characterised by a radius of $S = S_{\max}$ and a minimal uncertainty ΔS_z. [1] © IOP Publishing. Reproduced with permission. All rights reserved.

via [99]

$$N_\infty(N_0) = \frac{\sqrt{\pi}\,\Gamma\left(\frac{N_0}{2} + 1\right)}{\Gamma\left(\frac{N_0}{2} + \frac{1}{2}\right)} - 1, \tag{6.12}$$

where $\Gamma(f)$ is the gamma function of f. To get some understanding for this equation, Ref. [99] considers the case of two initial atoms, for which the expected remaining fraction $N_\infty/N_0 = 1/2$. For two uncorrelated atoms, the initial state is given by the equal superposition of the spin-singlet state $|s\rangle$ and spin-triplet state $|t\rangle$, here for example* written as $|\uparrow\downarrow\rangle = 1/\sqrt{2}|s\rangle + 1/\sqrt{2}|t\rangle = 1/2(|\uparrow\downarrow\rangle - |\downarrow\uparrow\rangle) + 1/2(|\uparrow\downarrow\rangle + |\downarrow\uparrow\rangle)$. Since the full fermionic wavefunction must be anti-symmetric, the spin-singlet state has a symmetric spatial wavefunction, whereas the spatial wavefunction of the spin-triplet state is anti-symmetric. Due to the anti-symmetry of the spatial wavefunction of the $|t\rangle$ state, it is dark to two-body losses [99]. Hence, only the spin-singlet state decays, and the triplet state remains for long times. This triplet state is the two-atom Dicke state, which exhibits maximum spin $S_{\text{tot}} = 1$ and minimal ΔS_z. Within a localised-spin picture, this

---

*In this example, the atom of the left (right) lattice site has spin up (down), but it holds for any phase between the singlet and triplet state, as long as the weighting is equal. The equal weighting requirement is another way of stating the initial state is uncorrelated.

can be seen as a build-up of correlations

$$|{\uparrow}{\downarrow}\rangle \overset{t \gg 1/\Gamma_{ee}}{\Longrightarrow} \frac{1}{2}\left(|{\uparrow}{\downarrow}\rangle + |{\downarrow}{\uparrow}\rangle\right)$$

Alternatively, within a many-body-state picture, this can be seen as the loss of states without a symmetric spin wavefunction

$$\frac{1}{\sqrt{2}}|s\rangle + \frac{1}{\sqrt{2}}|t\rangle \overset{t \gg 1/\Gamma_{ee}}{\Longrightarrow} \frac{1}{\sqrt{2}}|t\rangle.$$

In either case, for this two-particle example the remaining amplitude of the wavefunction is 1/2. For larger atom numbers, the remaining fraction can be calculated using Eq. 6.12.

Furthermore, Ref. [118] has shown that the sign of magnetic correlations changes over time, for an uncorrelated initial state of both fermionic and bosonic systems with SU(2) symmetry. The states subject to two-body losses have a lower energy than the state with a symmetric spin wave function, thus stabilising high-energy states, which is similar to negative temperature states in closed systems [118, 184, 185][*]. Simultaneously, the loss of low-energy anti-symmetric spin states leads to a sign reversal of the magnetic correlations. Though double occupancy is suppressed by U_{ee}, the virtual superexchange processes drive two-body losses [118]. This is markedly different from systems without two-body losses, where the superexchange process leads to the formation of anti-symmetric spin states for long times $t \gg t_{se}$.

6.3 Experimental Realisation with Excited ^{173}Yb

To study the dissipative Fermi-Hubbard model, we start with an ultracold gas of about 15 thousand ^{173}Yb atoms at $T \approx 0.25 T_F$ with one, two or six nuclear spin states, as described in Sec. 6.1. The atoms are then loaded into a deep 'magic' lattice of depths $s_{1D} = 50 E_r$ and $s_{2D} = 42 E_r$. This creates a Mott insulator with a small band-insulating core for $\mathcal{N} \geq 2$, as explained in Sec. 6.1.1. Using a RAP, the atoms are transferred to the $^3P_0$ excited state, which is subject to two-body losses with a decay strength of $\hbar\Gamma_{ee}/U_{ee} = 0.29(8)$ [21, 86] and SU(6) symmetry. Directly after the RAP, the 1D lattice is ramped down in 300 μs to a variable final lattice depth $s_{1D} \in [5, 6, 8]E_r$. Since the 2D lattice remains constant, this creates a system of quasi-1D lattice tubes, where tunnelling in the 2D plane is strongly supressed on experimental timescales. A $B = 3$ G

---

[*] Remember that the ground state of the Fermi-Hubbard model is a quantum antiferromagnetic state. All other possible states have higher energies.
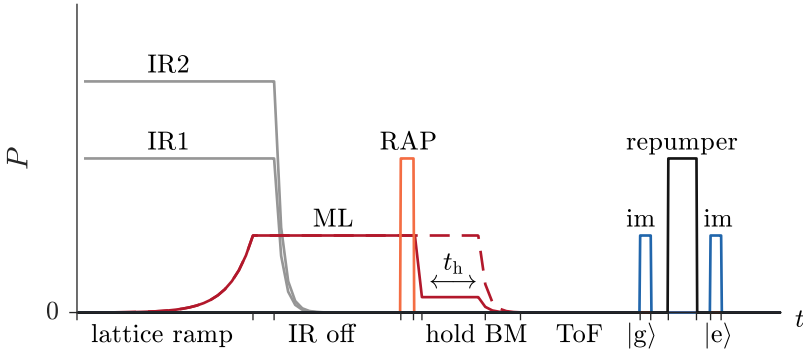
Figure 6.6: Schematic of a dissipation measurement sequence (not to scale), showing the laser beam powers P as a function of time t, analogous to Fig. 3.6. The yellow line indicates the clock beam power during the RAP, after which the 1D lattice beam is ramped down. The solid and dashed red lines indicate the 1D- and 2D-lattice laser-beam powers, respectively.

magnetic field in the y-direction provides a quantisation axis during the experiment, setting the S_z direction of the spin. After band mapping and time of flight, we measure the number of atoms in the ground and excited state. These measurements are referred to as *dissipation measurements* in the following, which are primarily distinguished from loss measurements (see Sec. 5.1.2) by the RAP excitation and ramping down of the 1D lattice afterwards to enable tunnelling. A schematic of the laser beam powers during a dissipation measurement is shown in Fig. 6.6.

6.3.1 Dissipation of Spin-Polarised Gases

Figure 6.7 shows dissipation measurements of excited spin-polarised atoms, where the Pauli-exclusion principle prevents double occupation and hence two-body losses. The remaining one-body losses are caused by collisions with background atoms in the vacuum, light scattering from the optical lattice, and radiative decay into the ground state. Like the one-body losses in Sec. 5.1.2, the atom number is fitted with $N_e(t_h) = N_{e,0} \exp(-\Gamma_0 t_h)$, where the initial atom number $N_{e,0}$ and the one-body decay rate Γ_0 are free parameters. The fits yield $1/e$ lifetimes of about 2.1(8) s, which is similar to the lifetime of spin-polarised atoms in a deep lattice (see Sec. 2.4.1).

Considering the spin-polarised losses in Figs. 6.7b and 6.7c, a small fast initial loss
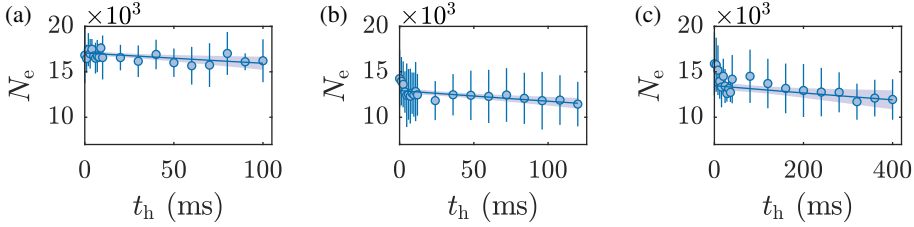
Figure 6.7: Dissipation measurement of excited spin-polarised ^{173}Yb atoms. Data points represent measured atom numbers and are five times averaged, with error bars representing the standard deviation. Solid lines represent an exponential fit (see text) and the shaded area shows its 95% confidence interval. The final 1D lattice depth was set to (a) $5E_r$, (b) $6E_r$ and (c) $8E_r$.

is observed. We attribute this to the small remaining fraction of about 7% of the atoms in other spin states (see Table 6.1). These other spin states together with an equal number of atoms in the desired spin state undergo quick dissipative losses, leading to a loss of about 10% of the atoms at short times.

The two- and six-spin mixtures, discussed in the following, are subject to both one- and two-body losses. To enable the study of purely two-body losses, the atom number of these spin mixtures is normalised to the one-body losses using a factor $\exp(\Gamma_0 t_h)$ per lattice depth *.

6.3.2 Dissipation of Two-Spin Mixtures

Figure 6.8 shows dissipation measurements of two-spin mixtures for various final lattice depths. Here, the excited state atom number is normalised to the one-body loss rate, such that only two-body losses remain, and normalised to the initial atom number at $t_h = 0$. Furthermore, the time is rescaled to the superexchange time $t_{se} = \hbar U/J^2$, which is a characteristic time scale of the system. After a short time $t_h \approx t_{se}$, the losses cease within experimental uncertainties, in qualitative agreement with the predicted dynamics [99].

To understand and quantify the two-spin loss dynamics within the simplified model, we consider Eq. 6.8. For a constant loss coefficient κ, the solution is given by $N_e(t) =$

---

* A more accurate treatment would use the solution of the rate equation $dN_e/dt = -\Gamma_0 N_e - \mathcal{P}_N \kappa N_e^2/N_{e,0}$ to fit the spin mixture data. However, this normalisation treatment is justified since the timescale of the two-body losses turns out to be about two orders of magnitude shorter than that of the one-body losses, making the difference between both methods negligible.
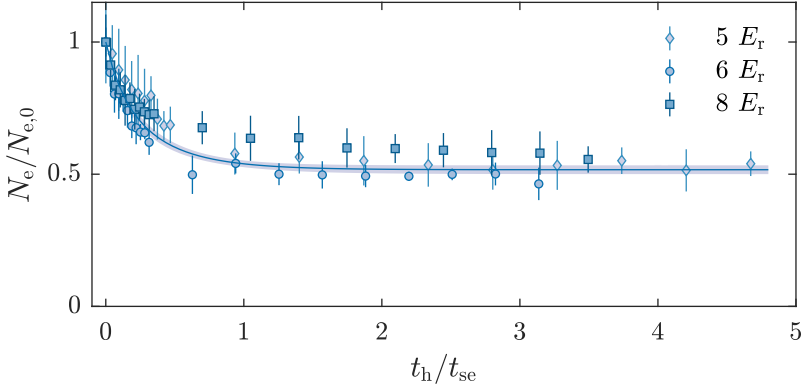
Figure 6.8: Dissipation measurement of a two-spin mixture of excited ^{173}Yb atoms, similar to Fig. 6.7. The relative atom number $N_{\mathrm{e}}(t)/N_{\mathrm{e},0}$ is plotted as a function of dimensionless hold time $t_{\mathrm{h}}/t_{\mathrm{se}}$. The different markers and colours denote data taken at different final lattice depths (see legend). The solid line shows the best fit with exponentially decaying κ (see text) and the shaded area shows its 95% confidence interval, yielding $\kappa_0 = 4.6(3)/t_{\mathrm{se}}$ and $\tau = 0.41(3)t_{\mathrm{se}}$. The figure is adapted from the published version [1]. © IOP Publishing. Reproduced with permission. All rights reserved.

$N_{\mathrm{e},0}/(1 + \mathcal{P}_{\mathcal{N}}\kappa t)$. Since this tends to zero for large times, this cannot describe our observations. The inhibition of two-body losses can only be explained by a vanishing κ. Since there are significant two-body losses for times $t_{\mathrm{h}} < t_{\mathrm{se}}$, the loss coefficient must be some decreasing function, which can only be explained by a decreasing $g^{(2)}$, since the others terms in $\kappa = 4q\Gamma_{\mathrm{eff}}g^{(2)}\eta_0$ remain constant throughout the measurement. The nearest-neighbour correlations function, however, can change over time since losses affect various correlated states differently. The functionality of the dynamic $\kappa(t)$ is not known *a priori*. We rule out power-law dynamics of the loss coefficient $\mathrm{d}\kappa/\mathrm{d}t \propto -\kappa^n$, since for any power $n > 1$ the atom number decays to zero for increasing times. However, for an exponentially decaying $\kappa(t) = \kappa_0 \exp(-t/\tau)$, where κ_0 is the initial loss coefficient at $t = 0$ and τ is the correlation build-up time, the excited-state atom number dynamics becomes [1]

$$N_{\mathrm{e}}(t) = \frac{N_{\mathrm{e},0}}{1 + \mathcal{P}_{\mathcal{N}}\,\kappa_0\,\tau - \mathcal{P}_{\mathcal{N}}\,\kappa_0\,\tau\,\mathrm{e}^{-t/\tau}}, \tag{6.13}$$

which for long times approaches the final atom number N_∞ [1]

$$N_\infty = N_e(t \to \infty) = \frac{N_{e,0}}{1 + \mathcal{P}_N \kappa_0 \tau}. \tag{6.14}$$

The two-spin mixture data is fitted with Eq. 6.13 and shown as the solid line in Fig. 6.8, which describes the data well*. Hence we conclude that $\kappa(t)$ and thus $g^{(2)}(t)$ decay exponentially. The fit yields $\kappa_0 = 4.6(3)/t_{se}$ and $\tau = 0.41(3)t_{se}$.

Though the exponentially-decaying $\kappa(t)$ is a phenomenological description, a recent work [123] found an analytic expression for the particle number dynamics of weakly-dissipative Fermi-Hubbard systems in 1D. Equation 6.13 is approximately the same as the short-time dynamics of the analytic expression and only shows minor deviations for longer time scales.

For a more complete understanding, both nearest-neighbour and higher-order correlations must be studied directly. Since we cannot access correlations directly, we argue why we think the final state is a Dicke state. As noted in Sec. 6.2, several many-body states exhibit $g^{(2)} = 0$. We rule out a state without nearest neighbours, because this state is not stable with respect to tunnelling. We further rule out a ferromagnetic state, since the initial state is spin-balanced such that $S_{z,tot} \approx 0$ and the two-body losses preserve the total spin†. Many-body states with domain walls between ferromagnetic domains are unstable to tunnelling. Therefore, we attribute the vanishing $g^{(2)}$ of the final state to the formation of a highly-entangled Dicke state, as predicted by Ref. [99].

Further note the stark difference between the loss dynamics of interorbital inter-isotope mixtures in Sec. 5.1.2 and these intraisotope spin mixtures. The interisotope mixtures decay to zero exponentially, since the particles are distinguishable and no correlated many-body states build up over time.

As mentioned, using the normalisation with the superexchange time t_{se}, the atom number dynamics with different s_{1D} overlap within experimental uncertainties, suggesting the dynamics is independent of lattice depths. A numerical simulation of a two-spin system on six sites confirmed that a varying onsite interaction U_{ee} only changes the dissipation timescale, but not the qualitative behaviour [1]. Furthermore, the dark states of the simulated system were confirmed to be Dicke states. Therefore, even though the original predictions [99] were made in 1D tubes without an onsite interaction U_{ee}, we conclude that the prediction applies to our lattice system. However, the dissipation timescale of the numeric simulation was almost one order of magnitude

---

* We also fitted the solution for a constant loss coefficient, but such a fit cannot describe the data well (see Ref. [1]).

† The SU(2) symmetry of the system prevents spin-exchanging interactions. Furthermore, the Pauli exclusion principle ensures that every lossy doubly-occupied site contains two different spins.

larger than what we measured in the experiment, which is an open question. Nevertheless, the simulation enables accessing the spin-correlations, and an approximately exponentially decaying $g^{(2)}$ was confirmed [1].

One of the main results of the prediction [99] is that fermions exhibiting inelastic *s*-wave interactions without initial correlations satisfies the bound in Eq. 6.12 for long times. In our experiment, the sample is made up of quasi-1D tubes with an *a priori* unknown number of atoms per tube, complicating the verification of the final atom number compared to the predicted bound. Assuming the atom distribution in the lattice is the same as that of the Fermi gas prior to lattice loading, the number of atoms per tube was calculated, similar to the method used by Ref. [192]. For our typical initial atom numbers of 13 thousand, the central tube contains 30 atoms and all other tubes hold fewer. Using the distribution of atoms per tubes as a weighting, we find an expected remaining ratio of $N_\infty/N_{e,0} \approx 0.27$. This is significantly smaller than the average measured ratio of $N_e(t_h \gg t_{se})/N_{e,0} = 0.51(3)$, based on the last five data points of the dissipation measurements. We rule out the effect of localised states [193], since for $s_{1D} = 5E_r$ these are expected to appear for tubes larger than 70 sites, whereas for $s_{1D} = 8E_r$ these appear above 32 sites. However, given the large repulsive interorbital interactions in ^{173}Yb [21], residual ground-state atoms are expected to effectively separate the tubes into smaller tubes*. About 7% of all atoms are in the ground state for short timescales, as obtained from double imaging (see Sec. 2.6) during the dissipation measurements. Assuming a random distribution of these blocking ground-state atoms over the lattice, the expected final fraction becomes $N_\infty/N_{e,0} \approx 0.35$. Though this explains a part of the discrepancy, this cannot explain everything. We attribute the remaining deviation to initial correlations prior to the measurement. As seen in Sec. 6.1.1 and Fig. 6.2b, applying a RAP to a spin mixture leads to losses prior to the dissipation measurement, which we attribute to the short decay times $2\pi/\Gamma_{ee} \approx 0.6$ ms of excited doublons in a deep lattice. Since a part of the symmetric spin-wave function is projected out by the RAP in this way, the initial correlations decrease $0 < g_0^{(2)} < 1$, leading to a remaining fraction that is larger than expected for an uncorrelated state with $g_0^{(2)} = 1$. The theoretical simulations done [1] showed that a higher initial Dicke state weight can indeed explain a larger remaining fraction.

Finally, note that one-body losses continue after the inferred formation of the Dicke state, which is why the atom number in Fig. 6.8 remains constant after normalising with the one-body decay rate†. Even though these one-body losses persist, they are not

---

* The interorbital interactions have been measured several times [21, 22, 28, 157], but the most accurate to date are given by $a_{eg^-} = 220(2)a_0$ [21] and $a_{eg^+} = 1894(18)a_0$ [157]. Using these, the direct interaction, the interaction of interorbital pairs with the same spin, is thus given by $a_{eg0} = 1057(9)a_0$.

† In other words, the unnormalised two-spin excited-state atoms decay at the same rate as atoms in spin-polarised samples.

expected to destroy the Dicke state on intermediate times, though for long enough times all atoms will have decayed via these one-body losses. Therefore, in future experiments using the formation of the Dicke state it is advisable to use lattice depths where the timescale of one-body losses is much longer than the timescale of the formation of the Dicke state, similar to the situation here.

6.3.3 Dissipation of Six-Spin Mixtures

To utilise the unique possibilities of SU(6)-symmetric ^{173}Yb, the dissipation measurement was repeated with all spin components. Since the predictions [99, 118] were made for SU(2)-symmetric systems, it is currently unknown if it can be generalised to SU($\mathcal{N} > 2$) symmetry. However, the sign-reversal of the magnetic correlations [118] is expected to hold for SU($\mathcal{N} \geq 2$)[194].

Figure 6.9 shows dissipation measurements of six-spin samples for three final 1D-lattice depths, analogous to Fig. 6.8. The dynamics qualitatively looks the same as the two-spin dynamics. After a short time $t_h \approx t_{se}$ the two-body losses cease within experimental uncertainties, suggesting the formation of a highly-correlated state which is dark to two-body losses. To explain the inhibition of two-body losses, we rule out the formation of a ferromagnetic state, because the remaining fraction of about 40% of the initial atoms is larger than any single m_F-state occupation (compare Table 6.1). Furthermore, as pointed out for two-spin mixtures, two-body losses conserve the initial total spin, which is approximately zero*. We further rule out a final state without nearest neighbours on the same grounds as for two-spin mixtures. In principle, losses of three or more atoms per site are thinkable for these six-spin mixtures, though these will be even more suppressed than double occupation already is. Though the data does not allow us to prove the formation of an SU(6)-symmetric Dicke state, we think the similarity of the two- and six-spin dynamics suggests as much.

Similarly to the two-spin mixtures, we fit Eq. 6.13 with $\mathcal{P}_6 = 5/6$, yielding $\kappa_0 = 3.2(2)/t_{se}$ and $\tau = 0.51(4)t_{se}$. The initial decay coefficient of six-spin components is smaller than κ_0 of two-spin components. This might be because the temperature of six-spin Fermi gases is typically a few percent lower than it is for two-spin Fermi gases, because optical pumping leads to finite heating (see Sec. 2.3.1). A lower temperature is expected to lead to more double occupancy among ground state atoms, causing larger losses during the RAP and thus a smaller initial $g_0^{(2)}$. The initial atom number of six-spin mixtures is about 11.5 thousand atoms compared to 13 thousand atoms of two-spin mixtures, corroborating this idea. The correlation-build-up timescale τ is larger

---

*Though this hold generally for two-spin mixtures, for six-spin mixtures the argument only holds on average over many two-body losses. Since almost five thousand atoms are lost over the dissipation measurement, this is a good approximation.
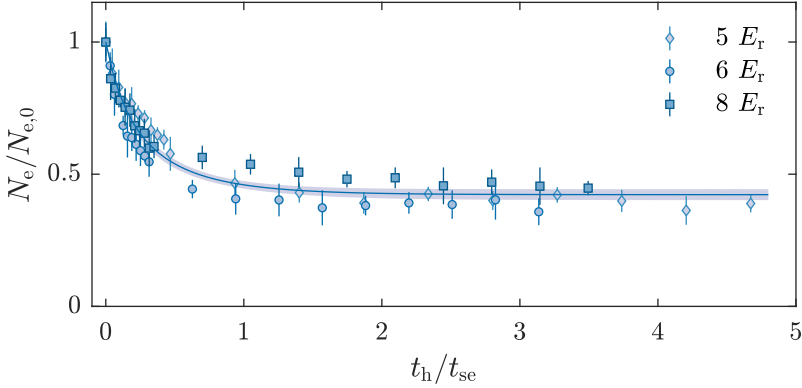
Figure 6.9: Dissipation measurement of a six-spin mixture of excited ^{173}Yb atoms, analogous to Fig. 6.8. The fit yields $\kappa_0 = 3.2(2)/t_{se}$ and $\tau = 0.51(4)t_{se}$. The figure is adapted from the published version [1]. © IOP Publishing. Reproduced with permission. All rights reserved.

for six-spins than it is for two, though the uncertainties are such that the deviation might merely be statistical. Nevertheless, further theoretical studies are required to get a better understanding of these non-trivial differences.

Lastly, the remaining fraction of both two- and six-spin samples is compared. Figure 6.10 shows the remaining fraction for both spin configurations and for each s_{1D}, as obtained from the last five data points and initial atom number per dissipation measurement. Though the remaining fraction is independent of lattice depth within experimental uncertainties, it is significantly lower for six-spin samples. The average remaining fractions are 0.51(3) and 0.41(2) for two- and six-spin mixtures, respectively. Though we do not know about theoretical predictions for $\mathcal{N} > 2$ mixtures, we consider it likely that an uncorrelated six-spin mixture has a lower Dicke state weight and thus a smaller remaining fraction than two-spin mixtures. However, more theoretical and experimental work is needed to obtain a better understanding of these differences.
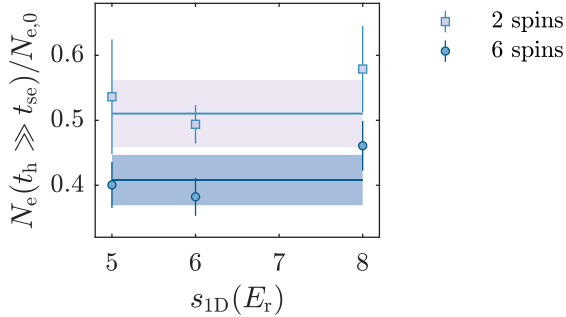
Figure 6.10: Remaining atom fraction $N_e(t_h \gg t_{se})/N_{e,0}$ as a function of final lattice depth. Data points depict the remaining fraction as obtained from the last five data points of the respective dissipation measurements and the initial atom number. Error bars represent the propagated uncertainties. The solid lines show the average remaining fractions and the shaded area its 95% confidence interval. The markers and colours represent different spin mixtures (see legend).

6.4 Conclusion & Outlook

To summarise, we have performed measurements on two- and six-spin mixtures of ^{173}Yb in a 1D lattice, studying the dissipative Fermi-Hubbard model. For two-spin mixtures, we measured an inhibition of two-body losses on timescales of approximately one superexchange time, independent on the exact atom number or 1D lattice depth. We attribute the ceasing of losses to the formation of a highly-entangled Dicke state, as predicted for this dissipative SU(2)-symmetric 1D system [99]. Dicke states are expected to be useful tools for high-precision spectroscopy because they allow beating the standard quantum limit and reaching the Heisenberg limit [99]. Using a simplified model, we found that the correlations build up exponentially on a timescale of $\tau = 0.41(3)t_{se}$ for two-spin mixtures, regardless of 1D lattice depth. The dynamics are also in qualitative agreement with the predicted atom number dynamics in a system which undergoes a sign reversal of magnetic correlations [118].

Six-spin fermionic systems showed very similar dynamics. Though it is unknown if the Dicke state formation also holds for SU($N > 2$)-symmetric systems, our measurements could be an interesting benchmark to test future theoretical work. Continued theoretical models are also required to understand the non-trivial difference between the dynamics of the SU(2) and SU(6)-symmetric systems.

Additionally, future experimental work could focus on tomographic [190, 191] or spectrographic [99] measurement to verify the nature of the final many-body state. Studying the dynamics in double wells is expected to greatly simplify the interpretation, because the final atom would not depend on the initial Fermi gas density. Furthermore, the dissipative dynamics can be studied in ^{171}Yb or ^{87}Sr, which have approximately the same dissipation strength as ^{173}Yb. In future work, however, it is advisable to blast any remaining $|g\rangle$ atoms on the $^1S_0 \rightarrow ^1P_1$ transition prior to the beginning of the measurement to ensure no ground-state atoms block the tunnelling of $|e\rangle$ atoms.

Alternatively, the magnetic field can be increased to separate the m_F-state resonances and to use a π^0-polarised clock pulse to selectively transfer one spin state into the ground state. The π^0-polarised pulse conserves the m_F state, hence maintaining the symmetry of the spin wave function. The resulting state could thus be an interorbital Dicke state where both the spin and orbital part of the wavefunction are symmetric. Then, clock spectroscopy can be done to show that there are no interorbital spin-exchange peaks, since doubly-occupied sites are suppressed. By doing this for various hold times t_h, the disappearance of interorbital spin-exchange peaks could be a sign of the formation of a highly-entangled Dicke state.

Since uncorrelated states are expected to satisfy a certain boundary (see Ref. [99] and Eq. 6.12), the atom number can also be a promising candidate to probe initial correlations which are otherwise hard to access. The ground state of the Fermi-Hubbard model is a quantum antiferromagnetic many-body state, which completely decays since it is not a dark state of the dissipative Hamiltonian*. Hence, the remaining fraction yields the initial weight of the quantum antiferromagnetic state, thus enabling a type of thermometry. For this, however, initial losses due to doublons must be ruled out.

The sign-reversal of the magnetic correlations is predicted to be observable in quantum gas microscopes [118]. Although our experiment does not have a sufficient resolution, other experiments [195, 196] can have the possibility to do this.

Finally, although the Dicke-state prediction was made for reactive SU(2)-symmetric 1D systems, it does not hold for higher dimensions with separable coordinates [99]. Since triangular lattices in 2D are not separable, this could create an interesting further platform to study the dynamical formation of Dicke states. This could be particularly interesting, since two-spin mixtures in a triangular lattice are prone to frustration [197]. With up to six spins for ^{173}Yb, the two-spin dynamics can be compared to three-spin measurements which are not affected by frustration. Another comparison can be made by studying two-spin mixtures in a triangular and hexagonal lattice, the latter of which does not cause frustration in two-spin systems [198].

---

*Note that this does not hold for the Néel state (see Sec. 6.2). Though the nearest-neighbour correlation function is $g^{(2)} = 2$, its spin wave function is not fully anti-symmetric (consider, for instance, exchange of two next-nearest neighbouring atoms), and hence the Néel state has a finite Dicke state weight.

Appendices

Appendix A

Spectroscopy in a Realistic Lattice

Optical lattices are typically realised in experiments using interfering Gaussian beams [8]. The centre of the lattice consequently has the highest light intensity and thus potential depths, whereas away from the centre, the potential depth is lower. Many atoms loaded into a lattice are therefore subject to different lattice depths. In this appendix, the size of this effect is studied and shown to be insignificant for our purposes. The analysis and graphs were done by the author.

For single atoms excited on the $^1S_0 \rightarrow\,^3P_0$ line in a lattice at the 'magic' wavelength, the transition probability is independent of the lattice depth. For two-body interactions, however, a more accurate treatment is required, since the interaction shifts depend on the lattice depths. As discussed in Sec. 4.1.1, a two-body interaction shift ΔU scales with the scattering length Δa and the integral over the Wannier function, in the following denoted by

$$W_0(s_{1D}, s_{2D}) = \int d\mathbf{r}\,|w_0(\mathbf{r}, s_{1D}, s_{2D})|^4, \qquad (A.1)$$

where it was assumed that both interacting particles are described by the same Wannier function and that the interaction energy is much smaller than the interband energy. In this way, the interaction shift is related to s_{1D} and s_{2D}.

Let us assume a lattice with 17 by 17 by 21 sites. As explained in Sec. 2.4.1, the optical lattice is made using four laser beams. The retro-reflected 1D laser beam has a waist of $94\,\mu m$ and the three 2D lattice beams have a waist of $84\,\mu m$ [128]. For these

calculations, a deep lattice was assumed, which is made using the maximum beam powers of about $800\,\mathrm{mW}$ for the 1D lattice beam and $300\,\mathrm{mW}$ per 2D lattice beam. The intensity distribution of a Gaussian beam in the z direction is given by [199]

$$I(r, z) = I_{\max} \left(\frac{w(0)}{w(z)} \right)^2 \mathrm{e}^{-2r^2/w(z)^2}, \tag{A.2}$$

where $I_{\max}$ denotes the maximum intensity in terms of beam power P as $I_{\max} = 2P/\pi w(0)^2$, $w(z)$ gives the spot size at z, such that at $z = 0$ the spot size is the waist $w(0)$, and r is the radial distance. The spot size is given by [199]

$$w(z) = w(0) \sqrt{1 + \left(\frac{z}{z_{\mathrm{R}}} \right)^2}, \tag{A.3}$$

where the Rayleigh range is given by $z_{\mathrm{R}} = \pi w(0)^2/\lambda$ [199]. Here the origin was chosen at the position of the beam waists.

Using Eq. A.2, the relative intensities $I/I_{\max}$ are calculated on a grid with distances set by the lattice distances, which are $\lambda/2$ for the 1D lattice and $2\lambda/3$ for the 2D lattice[166]. In the 1D lattice direction, 21 sites were considered, and 17 by 17 sites were considered in the 2D lattice plane, which results in about 6×10^3 sites for interacting pairs, a typical number in most spectroscopy measurements. Figure A.1a shows a histogram of the occurrence of the relative intensities. The Gaussian beams result in an asymmetric intensity profile over the whole grid. This is because there is an upper boundary in the relative intensity, which is exactly unity on the central site in the waists. The minimum of the relative intensity is 0.965 and the median lies at 0.988.

Simultaneously, the occurrence of different relative 1D and 2D lattice depths was calculated, assuming $s_{\mathrm{1D}} = 35E_{\mathrm{r}}$ and $s_{\mathrm{2D}} = 25E_{\mathrm{r}}$, and using Eq. A.1 the resulting Wannier integrals were calculated. Figure A.1b shows the occurrence of the relative Wannier integrals $W_0/W_{0,\max}$, where $W_{0,\max}$ is the Wannier integral at the maximum lattice depth $W_{0,\max} = W_0(35E_{\mathrm{r}}, 25E_{\mathrm{r}})$. The minimum of the relative Wannier integrals over the sample is 0.994 and the median is 0.998. The spread in the relative Wannier integrals is smaller than that of the relative intensities and the median is close to unity, because the slope of $W_0(s_{\mathrm{1D}}, s_{\mathrm{2D}})$ is smaller than unity for all lattice depths. Further note that the shape of the histogram is different from the relative intensity occurrence because W_0 depends on s_{1D} and s_{2D} non-linearly.

To study the effect of the realistic lattice beams on spectroscopic measurements, the interaction shift ΔU is calculated. For this a shift of $8\Omega_0$ is assumed, similar to the shift measured in the interisotope spectroscopy (see Ch. 5). Next, the occurrences of the relative Wannier integrals are used as a weighting to calculate the realistic interaction shifts. Figure A.2a shows a comparison of the expected spectrscopic signal for

(a)

(b)

Figure A.1: (a) Occurrence of relative laser intensities I/I_{max}. (b) Occurrence of relative Wannier integrals $W_0/W_{0,\mathrm{max}}$. All calculations were made for a lattice of 17 by 17 by 21 sites (see text).

a uniform lattice $n_{\mathrm{e,0}}$ with the signal for a realistic lattice $n_{\mathrm{e,r}}$, under the assumptions stated. The two signals can barely be distinguished, and hence the difference is shown in Fig. A.2b. The difference between the realistic and uniform-depth signal is typically within 1.5% for all detunings. Due to the spread in Wannier integrals, the peak of the realistic signal decreases to about $(1 - 1.2 \times 10^{-4})$ and shifts to approximately $7.98\Omega_0$. The asymmetric shape of the relative Wannier integrals cannot be distinguished on this scale.

Though for smaller Ω_0, larger atom numbers and a deeper lattices the effect of the non-uniformity of the lattice will increase, for the realistic values chosen here the effects are completely negligible. Furthermore, the lattice-modulation spectroscopy (see Sec. 2.4.1) used to determine the lattice depths rather finds effective average lattice depths, not the maximum lattice depths in the very centre of the lattice. Therefore, the difference between the realistic signal and the analysis of the spectroscopic measurements in Ch. 4 and 5 is even smaller than the difference between the realistic and uniform cases. Because of these reasons, we can justifiably neglect the non-uniformity of the lattice.
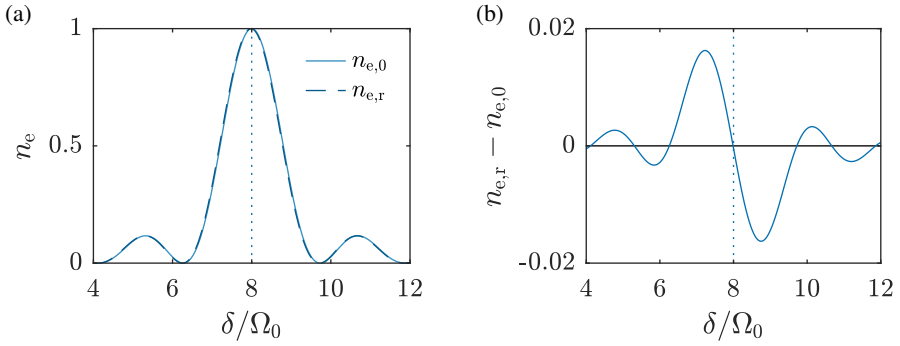
Figure A.2: The spectroscopic signal in a realistic lattice compared to a lattice with uniform depth, assuming a π-pulse. A shift of $\Delta U = 8\Omega_0$ was assumed (denoted by the vertical dotted line). All calculations were made for a lattice of 17 by 17 by 21 sites (see text). (a) Expected spectroscopic signal of a uniform-depth lattice $n_{e,0}$ (solid line) and of a realistic lattice $n_{e,r}$ (dashed line). (b) Difference between the realistic spectroscopic signal and the uniform-depth signal.

Appendix B

$g^{(2)}$ of a Dicke State

Since one cannot access the eigenstates of the many-body problem in the dissipative Fermi-Hubbard model, we need to find the observables for different eigenstates. Since different eigenstates yield different observables, we can infer which eigenstates consitute our system. In Ch. 6 we found the nearest-neighbour correlation function $g^{(2)}$ for several possible many-body states. In the following, we will show that $g^{(2)}$ is zero for two-spin Dicke states. The derivation was done by the author and published in Ref. [1].

The Dicke state which is expected to form in a 1D gas with SU(2)-symmetric two-body losses is given by [99]

$$\Psi = \mathcal{A}\Phi(r_1, \ldots, r_N) \sum_{\sigma} |\sigma\rangle, \tag{B.1}$$

where $\mathcal{A}$ is a normalisation factor, $\Phi(r_1, \ldots, r_N)$ is the fully anti-symmetric spatial wave function, such that $\Phi(\ldots, r_i, \ldots, r_j, \ldots) = -\Phi(\ldots, r_j, \ldots, r_i, \ldots)$ for any $i \neq j$. Furthermore, $\sum_{\sigma} |\sigma\rangle = \sum_{\sigma_1} \cdots \sum_{\sigma_N} |\sigma_1\rangle \otimes \cdots \otimes |\sigma_N\rangle$ is the fully-symmetric spin wave function. For brevity, we will use the notation $|\Phi\rangle$ for $\Phi(r_1, \ldots, r_N)$.

Recall that $g^{(2)}$ is given by Eq. 6.10

$$g^{(2)} = \frac{1}{N-1} \sum_{\langle ij \rangle} \frac{\left\langle \hat{n}_i \hat{n}_j - 4\hat{\mathbf{S}}_i \cdot \hat{\mathbf{S}}_j / \hbar^2 \right\rangle}{\langle \hat{n}_i \rangle \langle \hat{n}_j \rangle}. \tag{B.2}$$

We now consider the numerator of $g^{(2)}$ for a Dicke state

$$|\mathcal{A}|^2 \left(\langle \Phi | \sum_{\sigma} \langle \sigma | \hat{n}_i \hat{n}_j | \Phi \rangle \sum_{\sigma'} |\sigma'\rangle - \frac{4}{\hbar^2} \langle \Phi | \sum_{\sigma} \langle \sigma | \hat{\mathbf{S}}_i \cdot \hat{\mathbf{S}}_j | \Phi \rangle \sum_{\sigma'} |\sigma'\rangle \right), \tag{B.3}$$

which can be rewritten as

$$|\mathcal{A}|^2 \left(\sum_\sigma \sum_{\sigma'} \langle\sigma|\sigma'\rangle \langle\Phi| \hat{n}_i \hat{n}_j |\Phi\rangle - \frac{4}{\hbar^2} \underbrace{\langle\Phi|\Phi\rangle}_{=1} \sum_\sigma \sum_{\sigma'} \langle\sigma| \hat{\mathbf{S}}_i \cdot \hat{\mathbf{S}}_j |\sigma'\rangle \right). \tag{B.4}$$

Next, note that $\langle\Phi| \hat{n}_i \hat{n}_j |\Phi\rangle$ is either unity if both nearest-neighbouring sites are occupied, or zero if one or both sites are empty, in which case the contribution to $g^{(2)}$ is zero. Further, we introduce $C \equiv \sum_{\sigma \neq \sigma_i, \sigma_j} \sum_{\sigma' \neq \sigma'_i, \sigma'_j} \langle \sigma \neq \sigma_i, \sigma_j | \sigma' \neq \sigma'_i, \sigma'_j \rangle$, which is the sum over all spin states except the nearest-neighbour spins i and j. The notation $|\sigma_{i,j}\rangle \equiv \sum_{\sigma_i} \sum_{\sigma_j} |\sigma_i\rangle \otimes |\sigma_j\rangle$ is introduced, which can be written as $|\uparrow\uparrow\rangle + |\uparrow\downarrow\rangle + |\downarrow\uparrow\rangle + |\downarrow\downarrow\rangle$. Then, Eq. B.4 can be rewritten as

$$|\mathcal{A}|^2 C \left(\langle\sigma_{i,j}|\sigma'_{i,j}\rangle - \frac{4}{\hbar^2} \langle\sigma_{i,j}| \hat{\mathbf{S}}_i \cdot \hat{\mathbf{S}}_j |\sigma'_{i,j}\rangle \right). \tag{B.5}$$

Considering the term between brackets, we find

$$4 - \tfrac{4}{\hbar^2} \left(\langle\sigma_{i,j}| \tfrac{1}{2} \left(\hat{S}_{+,i}\hat{S}_{-,j} + \hat{S}_{-,i}\hat{S}_{+,j} \right) |\sigma'_{i,j}\rangle + \underbrace{\langle\sigma_{i,j}| \hat{S}_{z,i}\hat{S}_{z,j} |\sigma'_{i,j}\rangle}_{=0} \right) \tag{B.6}$$

$$= \qquad 4 - \tfrac{2}{\hbar^2} \langle\sigma_{i,j}| \left(\hat{S}_{+,i}\hat{S}_{-,j} + \hat{S}_{-,i}\hat{S}_{+,j} \right) |\sigma'_{i,j}\rangle \tag{B.7}$$

$$= \qquad 4 - \tfrac{2}{\hbar^2} \left(\underbrace{\langle\uparrow\downarrow| \hat{S}_{+,i}\hat{S}_{-,j} |\downarrow\uparrow\rangle}_{=\hbar^2} + \underbrace{\langle\downarrow\uparrow| \hat{S}_{-,i}\hat{S}_{+,j} |\uparrow\downarrow\rangle}_{=\hbar^2} \right) \tag{B.8}$$

$$= \qquad\qquad\qquad 0. \tag{B.9}$$

Further note that the denominator of Eq. B.2 is non-zero. Therefore, we have shown that each pair of nearest neighbours of a many-body Dicke state has a nearest neighbour correlation function of zero, resulting in a total $g^{(2)} = 0$ for the whole system.

Bibliography

[1] K. Sponselee, L. Freystatzky, B. Abeln, M. Diem, B. Hundt, A. Kochanke, T. Ponath, B. Santra, L. Mathey, K. Sengstock, and C. Becker. "Dynamics of ultracold quantum gases in the dissipative Fermi–Hubbard model". In: *Quantum Science and Technology* 4.1 (2018), p. 014002. DOI: 10.1088/2058-9565/aadccd (cit. on pp. vi, 3, 5, 9, 17, 90, 91, 93–98, 102–104, 106, 115).

[2] B. Abeln, K. Sponselee, M. Diem, N. Pintul, K. Sengstock, and C. Becker. "Interorbital interactions in an SU(2) ⊗ SU(6)-symmetric Fermi-Fermi mixture". In: *Phys. Rev. A* 103 (2021), p. 033315. DOI: 10.1103/PhysRevA.103.033315 (cit. on pp. vi, 2, 5, 8, 9, 43–47, 52–54, 62, 63, 65–70, 74–79, 81, 82, 84).

[3] E. A. Cornell and C. E. Wieman. "Nobel Lecture: Bose-Einstein condensation in a dilute gas, the first 70 years and some recent experiments". In: *Rev. Mod. Phys.* 74 (3 2002), pp. 875–893. DOI: 10.1103/RevModPhys.74.875 (cit. on p. 1).

[4] Wolfgang Ketterle. "Nobel lecture: When atoms behave as waves: Bose-Einstein condensation and the atom laser". In: *Rev. Mod. Phys.* 74 (4 2002), pp. 1131–1151. DOI: 10.1103/RevModPhys.74.1131 (cit. on p. 1).

[5] B. DeMarco and D. S. Jin. "Onset of Fermi Degeneracy in a Trapped Atomic Gas". In: *Science* 285.5434 (1999), pp. 1703–1706. ISSN: 0036-8075. DOI: 10.1126/science.285.5434.1703 (cit. on pp. 1, 2).

[6] R. P. Feynman. "Simulating physics with computers". In: *International Journal of Theoretical Physics* 21 (1982), pp. 467–488. DOI: 10.1007/BF02650179 (cit. on p. 1).

[7] Immanuel Bloch, Jean Dalibard, and Wilhelm Zwerger. "Many-body physics with ultracold gases". In: *Rev. Mod. Phys.* 80 (3 2008), pp. 885–964. DOI: 10.1103/RevModPhys.80.885 (cit. on p. 1).

[8] Christian Gross and Immanuel Bloch. "Quantum simulations with ultracold atoms in optical lattices". In: *Science* 357.6355 (2017), pp. 995–1001. ISSN: 0036-8075. DOI: `10.1126/science.aal3837`. eprint: `http://science.sciencemag.org/content/357/6355/995.full.pdf` (cit. on pp. 1, 17, 111).

[9] J. Hubbard. "Electron correlations in narrow energy bands". In: *Proc. R. Soc. Lond. A* 276 (1963), 238–257. DOI: `10.1098/rspa.1963.0204` (cit. on p. 1).

[10] J. Hubbard. "Electron correlations in narrow energy bands III. An improved solution". In: *Proc. R. Soc. Lond. A* 281 (1964), 401–419. DOI: `10.1098/rspa.1964.0190` (cit. on p. 1).

[11] D. Jaksch, C. Bruder, J. I. Cirac, C. W. Gardiner, and P. Zoller. "Cold Bosonic Atoms in Optical Lattices". In: *Phys. Rev. Lett.* 81 (15 1998), pp. 3108–3111. DOI: `10.1103/PhysRevLett.81.3108` (cit. on p. 1).

[12] Tilman Esslinger. "Fermi-Hubbard Physics with Atoms in an Optical Lattice". In: *Annual Review of Condensed Matter Physics* 1.1 (2010), pp. 129–152. DOI: `10.1146/annurev-conmatphys-070909-104059`. eprint: `https://doi.org/10.1146/annurev-conmatphys-070909-104059` (cit. on p. 1).

[13] Yosuke Takasu, Kenichi Maki, Kaduki Komori, Tetsushi Takano, Kazuhito Honda, Mitsutaka Kumakura, Tsutomu Yabuzaki, and Yoshiro Takahashi. "Spin-Singlet Bose-Einstein Condensation of Two-Electron Atoms". In: *Phys. Rev. Lett.* 91 (4 2003), p. 040404. DOI: `10.1103/PhysRevLett.91.040404` (cit. on p. 1).

[14] Hidetoshi Katori, Masao Takamoto, V. G. Pal'chikov, and V. D. Ovsiannikov. "Ultrastable Optical Clock with Neutral Atoms in an Engineered Light Shift Trap". In: *Phys. Rev. Lett.* 91 (17 2003), p. 173005. DOI: `10.1103/PhysRevLett.91.173005` (cit. on pp. 1, 7, 18).

[15] Masao Takamoto and Hidetoshi Katori. "Spectroscopy of the $^1S_0-^3P_0$ Clock Transition of ^{87}Sr in an Optical Lattice". In: *Phys. Rev. Lett.* 91 (22 2003), p. 223001. DOI: `10.1103/PhysRevLett.91.223001` (cit. on pp. 1, 7).

[16] M. Takamoto, F.L. Hong, R. Higashi, and H. Katori. "An optical lattice clock". In: *Nature* 435 (2005), 321–324. DOI: `10.1038/nature03541` (cit. on pp. 1, 7).

[17] W. F. McGrew et al. "Atomic clock performance enabling geodesy below the centimetre level". In: *Nature* 564 (2018), 87–90. DOI: `10.1038/s41586-018-0738-2` (cit. on pp. 1, 7).

[18]   G. Edward Marti, Ross B. Hutson, Akihisa Goban, Sara L. Campbell, Nicola Poli, and Jun Ye. "Imaging Optical Frequencies with 100 μHz Precision and 1.1 μm Resolution". In: *Phys. Rev. Lett.* 120 (10 2018), p. 103201. DOI: `10.1103/PhysRevLett.120.103201` (cit. on pp. 1, 7).

[19]   Tobias Bothwell, Dhruv Kedar, Eric Oelker, John M Robinson, Sarah L Bromley, Weston L Tew, Jun Ye, and Colin J Kennedy. "JILA SrI optical lattice clock with uncertainty of 2.0×10^{-18}". In: *Metrologia* 56.6 (2019), p. 065004. DOI: `10.1088/1681-7575/ab4089` (cit. on pp. 1, 7).

[20]   X. Zhang, M. Bishof, S. L. Bromley, C. V. Kraus, M. S. Safronova, P. Zoller, A. M. Rey, and J. Ye. "Spectroscopic observation of SU(N)-symmetric interactions in Sr orbital magnetism". In: *Science* 345.6203 (2014), pp. 1467–1473. ISSN: 0036-8075. DOI: `10.1126/science.1254978` (cit. on pp. 1, 2, 7, 43, 59, 95).

[21]   F. Scazza, C. Hofrichter, M. Höfer, P. C. De Groot, I. Bloch, and S. Fölling. "Observation of two-orbital spin-exchange interactions with ultracold SU(N)-symmetric fermions". In: *Nature Physics* 10.10 (2014), 779–784. ISSN: 1745-2481. DOI: `10.1038/nphys3061` (cit. on pp. 1, 2, 7, 8, 43, 59, 61, 81, 82, 87, 94, 95, 99, 104).

[22]   G. Cappellini et al. "Direct Observation of Coherent Interorbital Spin-Exchange Dynamics". In: *Phys. Rev. Lett.* 113 (12 2014), p. 120402. DOI: `10.1103/PhysRevLett.113.120402` (cit. on pp. 1, 2, 43, 45, 59, 61, 79, 81, 87, 104).

[23]   Koki Ono, Jun Kobayashi, Yoshiki Amano, Koji Sato, and Yoshiro Takahashi. "Antiferromagnetic interorbital spin-exchange interaction of ^{171}Yb". In: *Phys. Rev. A* 99 (3 2019), p. 032707. DOI: `10.1103/PhysRevA.99.032707` (cit. on pp. 1, 8, 43, 58, 59, 61, 81, 82, 87).

[24]   Sergey G. Porsev, Andrei Derevianko, and E. N. Fortson. "Possibility of an optical clock using the $6^1S_0 \rightarrow 6^3P_0^o$ transition in ^{171,173}Yb atoms held in an optical lattice". In: *Phys. Rev. A* 69 (2 2004), p. 021403. DOI: `10.1103/PhysRevA.69.021403` (cit. on pp. 1, 6, 7, 20, 26, 40).

[25]   A. V. Gorshkov, M. Hermele, V. Gurarie, C. Xu, P. S. Julienne, J. Ye, P. Zoller, E. Demler, M. D. Lukin, and A. M. Rey. "Two-orbital SU(N) magnetism with ultracold alkaline-earth atoms". In: *Nature Physics* 6.4 (2010), 289–295. ISSN: 1745-2481. DOI: `10.1038/nphys1535` (cit. on pp. 2, 7, 18, 43, 59, 69, 83, 86, 87).

[26]   Miguel A Cazalilla and Ana Maria Rey. "Ultracold Fermi gases with emergent SU(N) symmetry". In: *Reports on Progress in Physics* 77.12 (2014), p. 124401. ISSN: 1361-6633. DOI: `10.1088/0034-4885/77/12/124401` (cit. on pp. 2, 7).

[27]   Ren Zhang, Yanting Cheng, Hui Zhai, and Peng Zhang. "Orbital Feshbach Res-
       onance in Alkali-Earth Atoms". In: *Phys. Rev. Lett.* 115 (13 2015), p. 135301.
       DOI: 10.1103/PhysRevLett.115.135301 (cit. on pp. 2, 8).

[28]   M. Höfer, L. Riegger, F. Scazza, C. Hofrichter, D. R. Fernandes, M. M. Parish,
       J. Levinsen, I. Bloch, and S. Fölling. "Observation of an Orbital Interaction-
       Induced Feshbach Resonance in ^{173}Yb". In: *Phys. Rev. Lett.* 115 (26 2015),
       p. 265302. DOI: 10.1103/PhysRevLett.115.265302 (cit. on pp. 2, 8, 61, 73,
       81–83, 87, 104).

[29]   G. Pagano, M. Mancini, G. Cappellini, L. Livi, C. Sias, J. Catani, M. Inguscio,
       and L. Fallani. "Strongly Interacting Gas of Two-Electron Fermions at an Or-
       bital Feshbach Resonance". In: *Phys. Rev. Lett.* 115 (26 2015), p. 265301. DOI:
       10.1103/PhysRevLett.115.265301 (cit. on pp. 2, 8, 61, 87).

[30]   Lianyi He, Jia Wang, Shi-Guo Peng, Xia-Ji Liu, and Hui Hu. "Strongly corre-
       lated Fermi superfluid near an orbital Feshbach resonance: Stability, equation
       of state, and Leggett mode". In: *Phys. Rev. A* 94 (4 2016), p. 043624. DOI:
       10.1103/PhysRevA.94.043624 (cit. on pp. 2, 8).

[31]   Michael Foss-Feig, Michael Hermele, and Ana Maria Rey. "Probing the Kondo
       lattice model with alkaline-earth-metal atoms". In: *Phys. Rev. A* 81 (5 2010),
       p. 051603. DOI: 10.1103/PhysRevA.81.051603 (cit. on pp. 2, 7, 18, 43, 59).

[32]   Michael Foss-Feig, Michael Hermele, Victor Gurarie, and Ana Maria Rey.
       "Heavy fermions in an optical lattice". In: *Phys. Rev. A* 82 (5 2010), p. 053624.
       DOI: 10.1103/PhysRevA.82.053624 (cit. on pp. 2, 7, 18, 43, 59).

[33]   Ren Zhang, Deping Zhang, Yanting Cheng, Wei Chen, Peng Zhang, and Hui
       Zhai. "Kondo effect in alkaline-earth-metal atomic gases with confinement-
       induced resonances". In: *Phys. Rev. A* 93 (4 2016), p. 043601. DOI: 10.1103/
       PhysRevA.93.043601 (cit. on pp. 2, 7, 18, 43, 59).

[34]   Márton Kanász-Nagy, Yuto Ashida, Tao Shi, Cătălin Paşcu Moca, Tatsuhiko
       N. Ikeda, Simon Fölling, J. Ignacio Cirac, Gergely Zaránd, and Eugene A.
       Demler. "Exploring the anisotropic Kondo model in and out of equilibrium
       with alkaline-earth atoms". In: *Phys. Rev. B* 97 (15 2018), p. 155156. DOI: 10.
       1103/PhysRevB.97.155156 (cit. on pp. 2, 7, 18, 43, 59).

[35]   Takeshi Fukuhara, Yosuke Takasu, Mitsutaka Kumakura, and Yoshiro Taka-
       hashi. "Degenerate Fermi Gases of Ytterbium". In: *Phys. Rev. Lett.* 98 (3 2007),
       p. 030401. DOI: 10.1103/PhysRevLett.98.030401 (cit. on pp. 2, 7).

[36] Shintaro Taie, Yosuke Takasu, Seiji Sugawa, Rekishu Yamazaki, Takuya Tsujimoto, Ryo Murakami, and Yoshiro Takahashi. "Realization of a $SU(2) \times SU(6)$ System of Fermions in a Cold Atomic Gas". In: *Phys. Rev. Lett.* 105 (19 2010), p. 190401. DOI: `10.1103/PhysRevLett.105.190401` (cit. on pp. 2, 7, 63).

[37] B. J. DeSalvo, M. Yan, P. G. Mickelson, Y. N. Martinez de Escobar, and T. C. Killian. "Degenerate Fermi Gas of ^{87}Sr". In: *Phys. Rev. Lett.* 105 (3 2010), p. 030402. DOI: `10.1103/PhysRevLett.105.030402` (cit. on pp. 2, 7).

[38] Meng Khoon Tey, Simon Stellmer, Rudolf Grimm, and Florian Schreck. "Double-degenerate Bose-Fermi mixture of strontium". In: *Phys. Rev. A* 82 (1 2010), p. 011608. DOI: `10.1103/PhysRevA.82.011608` (cit. on pp. 2, 7).

[39] Guido Pagano, Marco Mancini, Giacomo Cappellini, Pietro Lombardi, Florian Schäfer, Hui Hu, Xia-Ji Liu, Jacopo Catani, Carlo Sias, Massimo Inguscio, and Leonardo Fallani. "A one-dimensional liquid of fermions with tunable spin". In: *Nature Physics* 10.3 (2014), 198–201. ISSN: 1745-2481. DOI: `10.1038/nphys2878` (cit. on p. 2).

[40] Bo Song, Yangqian Yan, Chengdong He, Zejian Ren, Qi Zhou, and Gyu-Boong Jo. "Evidence for Bosonization in a Three-Dimensional Gas of $SU(N)$ Fermions". In: *Phys. Rev. X* 10 (4 2020), p. 041053. DOI: `10.1103/PhysRevX.10.041053` (cit. on p. 2).

[41] Sayan Choudhury, Kazi R. Islam, Yanhua Hou, Jim A. Aman, Thomas C. Killian, and Kaden R. A. Hazzard. "Collective modes of ultracold fermionic alkaline-earth-metal gases with $SU(N)$ symmetry". In: *Phys. Rev. A* 101 (5 2020), p. 053612. DOI: `10.1103/PhysRevA.101.053612` (cit. on p. 2).

[42] Carsten Honerkamp and Walter Hofstetter. "Ultracold Fermions and the $SU(N)$ Hubbard Model". In: *Phys. Rev. Lett.* 92 (17 2004), p. 170403. DOI: `10.1103/PhysRevLett.92.170403` (cit. on p. 2).

[43] Michael Hermele, Victor Gurarie, and Ana Maria Rey. "Mott Insulators of Ultracold Fermionic Alkaline Earth Atoms: Underconstrained Magnetism and Chiral Spin Liquid". In: *Phys. Rev. Lett.* 103 (13 2009), p. 135301. DOI: `10.1103/PhysRevLett.103.135301` (cit. on p. 2).

[44] Cenke Xu. "Liquids in multiorbital $SU(N)$ magnets made up of ultracold alkaline-earth atoms". In: *Phys. Rev. B* 81 (14 2010), p. 144431. DOI: `10.1103/PhysRevB.81.144431` (cit. on p. 2).

[45]   Shintaro Taie, Rekishu Yamazaki, Seiji Sugawa, and Yoshiro Takahashi. "An SU(6) Mott insulator of an atomic Fermi gas realized by large-spin Pomeranchuk cooling". In: *Nature Physics* 8.11 (2012), 825–830. ISSN: 1745-2481. DOI: `10.1038/nphys2430` (cit. on p. 2).

[46]   Christian Hofrichter, Luis Riegger, Francesco Scazza, Moritz Höfer, Diogo Rio Fernandes, Immanuel Bloch, and Simon Fölling. "Direct Probing of the Mott Crossover in the SU(*N*) Fermi-Hubbard Model". In: *Phys. Rev. X* 6 (2 2016), p. 021030. DOI: `10.1103/PhysRevX.6.021030` (cit. on p. 2).

[47]   Shenglong Xu, Julio T. Barreiro, Yu Wang, and Congjun Wu. "Interaction Effects with Varying *N* in SU(*N*) Symmetric Fermion Lattice Systems". In: *Phys. Rev. Lett.* 121 (16 2018), p. 167205. DOI: `10.1103/PhysRevLett.121.167205` (cit. on p. 2).

[48]   M. Mancini, G. Pagano, G. Cappellini, L. Livi, M. Rider, J. Catani, C. Sias, P. Zoller, M. Inguscio, M. Dalmonte, and L. Fallani. "Observation of chiral edge states with neutral fermions in synthetic Hall ribbons". In: *Science* 349.6255 (2015), pp. 1510–1513. ISSN: 0036-8075. DOI: `10.1126/science.aaa8736`. eprint: `https://science.sciencemag.org/content/349/6255/1510.full.pdf` (cit. on p. 2).

[49]   L. F. Livi, G. Cappellini, M. Diem, L. Franchi, C. Clivati, M. Frittelli, F. Levi, D. Calonico, J. Catani, M. Inguscio, and L. Fallani. "Synthetic Dimensions and Spin-Orbit Coupling with an Optical Clock Transition". In: *Phys. Rev. Lett.* 117 (22 2016), p. 220401. DOI: `10.1103/PhysRevLett.117.220401` (cit. on pp. 2, 7, 38).

[50]   Jin Hyoun Kang, Jeong Ho Han, and Y. Shin. "Realization of a Cross-Linked Chiral Ladder with Neutral Fermions in a 1D Optical Lattice by Orbital-Momentum Coupling". In: *Phys. Rev. Lett.* 121 (15 2018), p. 150403. DOI: `10.1103/PhysRevLett.121.150403` (cit. on p. 2).

[51]   Jeong Ho Han, Jin Hyoun Kang, and Y. Shin. "Band Gap Closing in a Synthetic Hall Tube of Neutral Fermions". In: *Phys. Rev. Lett.* 122 (6 2019), p. 065303. DOI: `10.1103/PhysRevLett.122.065303` (cit. on p. 2).

[52]   C. Ospelkaus, S. Ospelkaus, K. Sengstock, and K. Bongs. "Interaction-Driven Dynamics of ^{40}K$-^{87}$Rb Fermion-Boson Gas Mixtures in the Large-Particle-Number Limit". In: *Phys. Rev. Lett.* 96 (2 2006), p. 020401. DOI: `10.1103/PhysRevLett.96.020401` (cit. on p. 2).

[53] S. Ospelkaus, A. Pe'er, K. K. Ni, J. J. Zirbel, B. Neyenhuis, S. Kotochigova, P. S. Julienne, J. Ye, and D. S. Jin. "Efficient state transfer in an ultracold dense gas of heteronuclear molecules". In: *Nature Physics* 4.8 (2008), pp. 622–626. ISSN: 1745-2481. DOI: `10.1038/nphys997` (cit. on p. 2).

[54] M. H. G. de Miranda, A. Chotia, B. Neyenhuis, D. Wang, G. Quéméner, S. Ospelkaus, J. L. Bohn, J. Ye, and D. S. Jin. "Controlling the quantum stereo-dynamics of ultracold bimolecular reactions". In: *Nature Physics* 7.6 (2011), 502–507. ISSN: 1745-2481. DOI: `10.1038/nphys1939` (cit. on p. 2).

[55] Amodsen Chotia, Brian Neyenhuis, Steven A. Moses, Bo Yan, Jacob P. Covey, Michael Foss-Feig, Ana Maria Rey, Deborah S. Jin, and Jun Ye. "Long-Lived Dipolar Molecules and Feshbach Molecules in a 3D Optical Lattice". In: *Phys. Rev. Lett.* 108 (8 2012), p. 080405. DOI: `10.1103/PhysRevLett.108.080405` (cit. on p. 2).

[56] C. Kohstall, M. Zaccanti, M. Jag, A. Trenkwalder, P. Massignan, G. M. Bruun, F. Schreck, and R. Grimm. "Metastability and coherence of repulsive polarons in a strongly interacting Fermi mixture". In: *Nature* 485.7400 (2012), 615–618. ISSN: 1476-4687. DOI: `10.1038/nature11065` (cit. on p. 2).

[57] Marco Koschorreck, Daniel Pertot, Enrico Vogt, Bernd Fröhlich, Michael Feld, and Michael Köhl. "Attractive and repulsive Fermi polarons in two dimensions". In: *Nature* 485.7400 (2012), 619–622. ISSN: 1476-4687. DOI: `10.1038/nature11151` (cit. on p. 2).

[58] Pietro Massignan, Matteo Zaccanti, and Georg M Bruun. "Polarons, dressed molecules and itinerant ferromagnetism in ultracold Fermi gases". In: *Reports on Progress in Physics* 77.3 (2014), p. 034401. ISSN: 1361-6633. DOI: `10.1088/0034-4885/77/3/034401` (cit. on p. 2).

[59] N. Darkwah Oppong, L. Riegger, O. Bettermann, M. Höfer, J. Levinsen, M. M. Parish, I. Bloch, and S. Fölling. "Observation of Coherent Multiorbital Polarons in a Two-Dimensional Fermi Gas". In: *Phys. Rev. Lett.* 122 (19 2019), p. 193604. DOI: `10.1103/PhysRevLett.122.193604` (cit. on p. 2).

[60] M. Iskin and C. A. R. Sá de Melo. "Superfluid and Insulating Phases of Fermion Mixtures in Optical Lattices". In: *Phys. Rev. Lett.* 99 (8 2007), p. 080403. DOI: `10.1103/PhysRevLett.99.080403` (cit. on p. 2).

[61] Kenneth Günter, Thilo Stöferle, Henning Moritz, Michael Köhl, and Tilman Esslinger. "Bose-Fermi Mixtures in a Three-Dimensional Optical Lattice". In: *Phys. Rev. Lett.* 96 (18 2006), p. 180402. DOI: `10.1103/PhysRevLett.96.180402` (cit. on p. 2).

[62]   Zhihao Xu and Shu Chen. "Topological Mott insulators of ultracold atomic mixtures induced by interactions in one-dimensional optical superlattices". In: *Phys. Rev. B* 88 (4 2013), p. 045110. DOI: `10.1103/PhysRevB.88.045110` (cit. on p. 2).

[63]   Pierre Nataf, Miklós Lajkó, Alexander Wietek, Karlo Penc, Frédéric Mila, and Andreas M. Läuchli. "Chiral Spin Liquids in Triangular-Lattice SU(N) Fermionic Mott Insulators with Artificial Gauge Fields". In: *Phys. Rev. Lett.* 117 (16 2016), p. 167202. DOI: `10.1103/PhysRevLett.117.167202` (cit. on p. 2).

[64]   Franco T. Lisandrini, Alejandro M. Lobos, Ariel O. Dobry, and Claudio J. Gazza. "Topological Kondo insulators in one dimension: Continuous Haldane-type ground-state evolution from the strongly interacting to the noninteracting limit". In: *Phys. Rev. B* 96 (7 2017), p. 075124. DOI: `10.1103/PhysRevB.96.075124` (cit. on p. 2).

[65]   Daniel Greif, Thomas Uehlinger, Gregor Jotzu, Leticia Tarruell, and Tilman Esslinger. "Short-Range Quantum Magnetism of Ultracold Fermions in an Optical Lattice". In: *Science* 340.6138 (2013), pp. 1307–1310. ISSN: 0036-8075. DOI: `10.1126/science.1236362` (cit. on p. 2).

[66]   Maxwell F. Parsons, Anton Mazurenko, Christie S. Chiu, Geoffrey Ji, Daniel Greif, and Markus Greiner. "Site-resolved measurement of the spin-correlation function in the Fermi-Hubbard model". In: *Science* 353.6305 (2016), pp. 1253–1256. ISSN: 0036-8075. DOI: `10.1126/science.aag1430` (cit. on p. 2).

[67]   Anton Mazurenko, Christie S. Chiu, Geoffrey Ji, Maxwell F. Parsons, Márton Kanász-Nagy, Richard Schmidt, Fabian Grusdt, Eugene Demler, Daniel Greif, and Markus Greiner. "A cold-atom Fermi-Hubbard antiferromagnet". In: *Nature* 545.7655 (2017), 462–466. ISSN: 1476-4687. DOI: `10.1038/nature22362` (cit. on p. 2).

[68]   C. J. Myatt, E. A. Burt, R. W. Ghrist, E. A. Cornell, and C. E. Wieman. "Production of Two Overlapping Bose-Einstein Condensates by Sympathetic Cooling". In: *Phys. Rev. Lett.* 78 (4 1997), pp. 586–589. DOI: `10.1103/PhysRevLett.78.586` (cit. on p. 2).

[69]   D. S. Hall, M. R. Matthews, J. R. Ensher, C. E. Wieman, and E. A. Cornell. "Dynamics of Component Separation in a Binary Mixture of Bose-Einstein Condensates". In: *Phys. Rev. Lett.* 81 (8 1998), pp. 1539–1542. DOI: `10.1103/PhysRevLett.81.1539` (cit. on p. 2).

[70] J. Stenger, S. Inouye, D. M. Stamper-Kurn, H.-J. Miesner, A. P. Chikkatur, and W. Ketterle. "Spin domains in ground-state Bose–Einstein condensates". In: *Nature* 396.6709 (1998), 345–348. ISSN: 1476-4687. DOI: 10.1038/24567 (cit. on p. 2).

[71] Cindy A. Regal, Christopher Ticknor, John L. Bohn, and Deborah S. Jin. "Creation of ultracold molecules from a Fermi gas of atoms". In: *Nature* 424.6944 (2003), 47–50. ISSN: 1476-4687. DOI: 10.1038/nature01738 (cit. on p. 2).

[72] Andrew G. Truscott, Kevin E. Strecker, William I. McAlexander, Guthrie B. Partridge, and Randall G. Hulet. "Observation of Fermi Pressure in a Gas of Trapped Atoms". In: *Science* 291.5513 (2001), pp. 2570–2572. ISSN: 0036-8075. DOI: 10.1126/science.1059318 (cit. on p. 2).

[73] F. Schreck, L. Khaykovich, K. L. Corwin, G. Ferrari, T. Bourdel, J. Cubizolles, and C. Salomon. "Quasipure Bose-Einstein Condensate Immersed in a Fermi Sea". In: *Phys. Rev. Lett.* 87 (8 2001), p. 080403. DOI: 10.1103/PhysRevLett.87.080403 (cit. on p. 2).

[74] S. B. Papp, J. M. Pino, and C. E. Wieman. "Tunable Miscibility in a Dual-Species Bose-Einstein Condensate". In: *Phys. Rev. Lett.* 101 (4 2008), p. 040402. DOI: 10.1103/PhysRevLett.101.040402 (cit. on p. 2).

[75] Takeshi Fukuhara, Seiji Sugawa, Yosuke Takasu, and Yoshiro Takahashi. "All-optical formation of quantum degenerate mixtures". In: *Phys. Rev. A* 79 (2 2009), p. 021601. DOI: 10.1103/PhysRevA.79.021601 (cit. on p. 2).

[76] Z. Hadzibabic, C. A. Stan, K. Dieckmann, S. Gupta, M. W. Zwierlein, A. Görlitz, and W. Ketterle. "Two-Species Mixture of Quantum Degenerate Bose and Fermi Gases". In: *Phys. Rev. Lett.* 88 (16 2002), p. 160401. DOI: 10.1103/PhysRevLett.88.160401 (cit. on p. 2).

[77] C. A. Stan, M. W. Zwierlein, C. H. Schunck, S. M. F. Raupach, and W. Ketterle. "Observation of Feshbach Resonances between Two Different Atomic Species". In: *Phys. Rev. Lett.* 93 (14 2004), p. 143001. DOI: 10.1103/PhysRevLett.93.143001 (cit. on p. 2).

[78] S. Inouye, J. Goldwin, M. L. Olsen, C. Ticknor, J. L. Bohn, and D. S. Jin. "Observation of Heteronuclear Feshbach Resonances in a Mixture of Bosons and Fermions". In: *Phys. Rev. Lett.* 93 (18 2004), p. 183201. DOI: 10.1103/PhysRevLett.93.183201 (cit. on p. 2).

[79] M. Taglieber, A.-C. Voigt, T. Aoki, T. W. Hänsch, and K. Dieckmann. "Quantum Degenerate Two-Species Fermi-Fermi Mixture Coexisting with a Bose-Einstein Condensate". In: *Phys. Rev. Lett.* 100 (1 2008), p. 010401. DOI: 10.1103/PhysRevLett.100.010401 (cit. on p. 2).

[80] E. Wille et al. "Exploring an Ultracold Fermi-Fermi Mixture: Interspecies Feshbach Resonances and Scattering Properties of ^{6}Li and ^{40}K". In: *Phys. Rev. Lett.* 100 (5 2008), p. 053201. DOI: 10.1103/PhysRevLett.100.053201 (cit. on p. 2).

[81] Hideaki Hara, Yosuke Takasu, Yoshifumi Yamaoka, John M. Doyle, and Yoshiro Takahashi. "Quantum Degenerate Mixtures of Alkali and Alkaline-Earth-Like Atoms". In: *Phys. Rev. Lett.* 106 (20 2011), p. 205304. DOI: 10.1103/PhysRevLett.106.205304 (cit. on p. 2).

[82] A. Hubener, M. Snoek, and W. Hofstetter. "Magnetic phases of two-component ultracold bosons in an optical lattice". In: *Phys. Rev. B* 80 (24 2009), p. 245109. DOI: 10.1103/PhysRevB.80.245109 (cit. on p. 2).

[83] B. Capogrosso-Sansone, Ş. G. Söyler, N. V. Prokof'ev, and B. V. Svistunov. "Critical entropies for magnetic ordering in bosonic mixtures on a lattice". In: *Phys. Rev. A* 81 (5 2010), p. 053622. DOI: 10.1103/PhysRevA.81.053622 (cit. on p. 2).

[84] M. Lewenstein, L. Santos, M. A. Baranov, and H. Fehrmann. "Atomic Bose-Fermi Mixtures in an Optical Lattice". In: *Phys. Rev. Lett.* 92 (5 2004), p. 050401. DOI: 10.1103/PhysRevLett.92.050401 (cit. on p. 2).

[85] I. Titvinidze, M. Snoek, and W. Hofstetter. "Supersolid Bose-Fermi Mixtures in Optical Lattices". In: *Phys. Rev. Lett.* 100 (10 2008), p. 100401. DOI: 10.1103/PhysRevLett.100.100401 (cit. on p. 2).

[86] Masaaki Kitagawa, Katsunari Enomoto, Kentaro Kasa, Yoshiro Takahashi, Roman Ciuryło, Pascal Naidon, and Paul S. Julienne. "Two-color photoassociation spectroscopy of ytterbium atoms and the precise determinations of *s*-wave scattering lengths". In: *Phys. Rev. A* 77 (1 2008), p. 012719. DOI: 10.1103/PhysRevA.77.012719 (cit. on pp. 2, 8, 14, 16, 48, 56, 57, 66, 68, 69, 79, 81–83, 85, 87, 94, 95, 99).

[87] Seiji Sugawa, Kensuke Inaba, Shintaro Taie, Rekishu Yamazaki, Makoto Yamashita, and Yoshiro Takahashi. "Interaction and filling-induced quantum phases of dual Mott insulators of bosons and fermions". In: *Nat. Phys.* 7 (2011), p. 642. DOI: 10.1038/nphys2028 (cit. on pp. 2, 83, 87).

[88] M. W. Zwierlein, C. A. Stan, C. H. Schunck, S. M. F. Raupach, S. Gupta, Z. Hadzibabic, and W. Ketterle. "Observation of Bose-Einstein Condensation of Molecules". In: *Phys. Rev. Lett.* 91 (25 2003), p. 250401. DOI: `10.1103/PhysRevLett.91.250401` (cit. on p. 2).

[89] Markus Greiner, Cindy A. Regal, and Deborah S. Jin. "Emergence of a molecular Bose-Einstein condensate from a Fermi gas". In: *Nat. Phys.* 426 (2003), 537–540. DOI: `10.1038/nature02199` (cit. on p. 2).

[90] Martin W. Zwierlein, André Schirotzek, Christian H. Schunck, and Wolfgang Ketterle. "Fermionic Superfluidity with Imbalanced Spin Populations". In: *Science* 311.5760 (2006), pp. 492–496. ISSN: 0036-8075. DOI: `10.1126/science.1122318` (cit. on p. 2).

[91] C. H. Schunck, Y. Shin, A. Schirotzek, M. W. Zwierlein, and W. Ketterle. "Pairing Without Superfluidity: The Ground State of an Imbalanced Fermi Mixture". In: *Science* 316.5826 (2007), pp. 867–870. ISSN: 0036-8075. DOI: `10.1126/science.1140749` (cit. on p. 2).

[92] S.-K. Yip. "Theory of a fermionic superfluid with SU(2)×SU(6) symmetry". In: *Phys. Rev. A* 83 (6 2011), p. 063607. DOI: `10.1103/PhysRevA.83.063607` (cit. on p. 2).

[93] Chen-Yen Lai, Chuntai Shi, and S.-W. Tsai. "Correlated phases of population imbalanced Fermi-Fermi mixtures on an optical lattice". In: *Phys. Rev. B* 87 (7 2013), p. 075134. DOI: `10.1103/PhysRevB.87.075134` (cit. on pp. 2, 61, 87).

[94] Luca Lepori, Andrea Trombettoni, and Walter Vinci. "Simulation of two-flavor symmetry-locking phases in ultracold fermionic mixtures". In: *EPL* 109 (2015), p. 50002. DOI: `10.1209/0295-5075/109/50002` (cit. on pp. 2, 61, 87).

[95] Joao C. Pinto Barros, Luca Lepori, and Andrea Trombettoni. "Phase diagram and non-Abelian symmetry locking for fermionic mixtures with unequal interactions". In: *Phys. Rev. A* 96 (1 2017), p. 013603. DOI: `10.1103/PhysRevA.96.013603` (cit. on pp. 2, 61, 87).

[96] S. Diehl, A. Micheli, A. Kantian, B. Kraus, H. P. Büchler, and P. Zoller. "Quantum states and phases in driven open quantum systems with cold atoms". In: *Nature Physics* 4.11 (2008), pp. 878–883. ISSN: 17452473. DOI: `10.1038/nphys1073`. arXiv: `0803.1482` (cit. on pp. 3, 89).

[97] Frank Verstraete, Michael M. Wolf, and J. Ignacio Cirac. "Quantum computation and quantum-state engineering driven by dissipation". In: *Nature Physics* 5.9 (2009), pp. 633–636. ISSN: 17452473. DOI: `10.1038/nphys1342`. arXiv: `0803.1447` (cit. on pp. 3, 89).

[98]   Sebastian Diehl, Enrique Rico, Mikhail A. Baranov, and Peter Zoller. "Topol-
        ogy by dissipation in atomic quantum wires". In: *Nature Physics* 7.12 (2011),
        pp. 971–977. ISSN: 17452481. DOI: 10.1038/NPHYS2106. arXiv: 1105.5947
        (cit. on pp. 3, 89).

[99]   Michael Foss-Feig, Andrew J. Daley, James K. Thompson, and Ana Maria Rey.
        "Steady-state many-body entanglement of hot reactive fermions". In: *Physi-
        cal Review Letters* 109.23 (2012), pp. 1–5. ISSN: 00319007. DOI: 10.1103/
        PhysRevLett.109.230501. arXiv: arXiv:1207.4741v1 (cit. on pp. 3, 4,
        89, 90, 94, 96–98, 101, 103–105, 107, 108, 115).

[100]   D. Witthaut, F. Trimborn, and S. Wimberger. "Dissipation induced coherence
        of a two-mode Bose-Einstein condensate". In: *Physical Review Letters* 101.20
        (2008). ISSN: 00319007. DOI: 10.1103/PhysRevLett.101.200402. arXiv:
        arXiv:0809.1776v1 (cit. on pp. 3, 89).

[101]   A. Griessner, A. J. Daley, S. R. Clark, D. Jaksch, and P. Zoller. "Dark-state
        cooling of atoms by superfluid immersion". In: *Physical Review Letters* 97.22
        (2006), pp. 1–4. ISSN: 00319007. DOI: 10.1103/PhysRevLett.97.220403.
        arXiv: 0607254 [cond-mat] (cit. on pp. 3, 89).

[102]   Stefan K. Baur and Erich J. Mueller. "Two-body recombination in a quantum-
        mechanical lattice gas: Entropy generation and probing of short-range mag-
        netic correlations". In: *Physical Review A - Atomic, Molecular, and Optical
        Physics* 82.2 (2010). ISSN: 10502947. DOI: 10.1103/PhysRevA.82.023626.
        arXiv: 1003.5235 (cit. on pp. 3, 89, 94, 96).

[103]   J. Catani, G. Barontini, G. Lamporesi, F. Rabatti, G. Thalhammer, F. Minardi,
        S. Stringari, and M. Inguscio. "Entropy exchange in a mixture of ultracold
        atoms". In: *Physical Review Letters* 103.14 (2009), pp. 2–5. ISSN: 00319007.
        DOI: 10.1103/PhysRevLett.103.140401. arXiv: 0906.2264 (cit. on pp. 3,
        89).

[104]   D. Chen, C. Meldgin, and B. Demarco. "Bath-induced band decay of a Hubbard
        lattice gas". In: *Physical Review A - Atomic, Molecular, and Optical Physics*
        90.1 (2014), pp. 1–5. ISSN: 10941622. DOI: 10.1103/PhysRevA.90.013602.
        arXiv: 1401.5096 (cit. on pp. 3, 89).

[105]   G. Barontini, R. Labouvie, F. Stubenrauch, A. Vogler, V. Guarrera, and H. Ott.
        "Controlling the dynamics of an open many-body quantum system with lo-
        calized dissipation". In: *Physical Review Letters* 110.3 (2013), pp. 1–5. ISSN:
        00319007. DOI: 10.1103/PhysRevLett.110.035302. arXiv: arXiv:1212.
        4824v1 (cit. on pp. 3, 89).

[106] Ralf Labouvie, Bodhaditya Santra, Simon Heun, and Herwig Ott. "Bistability in a Driven-Dissipative Superfluid". In: *Physical Review Letters* 116.23 (2016), pp. 1–5. ISSN: 10797114. DOI: `10.1103/PhysRevLett.116.235302` (cit. on pp. 3, 89).

[107] Henrik P. Lüschen, Pranjal Bordia, Sean S. Hodgman, Michael Schreiber, Saubhik Sarkar, Andrew J. Daley, Mark H. Fischer, Ehud Altman, Immanuel Bloch, and Ulrich Schneider. "Signatures of many-body localization in a controlled open quantum system". In: *Physical Review X* 7.1 (2017), pp. 1–13. ISSN: 21603308. DOI: `10.1103/PhysRevX.7.011034`. arXiv: `1610.01613` (cit. on pp. 3, 89).

[108] R. Bouganne, M. Bosch Aguilera, A. Ghermaoui, J. Beugnon, and Gerbier F. "Anomalous decay of coherence in a dissipative many-body system". In: *Nature Physics* 16 (2020), p. 040402. DOI: `10.1038/s41567-019-0678-2` (cit. on pp. 3, 89).

[109] Y. S. Patil, S. Chakram, and M. Vengalattore. "Measurement-Induced Localization of an Ultracold Lattice Gas". In: *Physical Review Letters* 115.14 (2015), pp. 1–5. ISSN: 10797114. DOI: `10.1103/PhysRevLett.115.140402`. arXiv: `1411.2678` (cit. on pp. 3, 89).

[110] N. Syassen, D. M. Bauer, M. Lettner, T. Volz, D. Dietze, J. J. García-Ripoll, J. I. Cirac, G. Rempe, and S. Dürr. "Strong dissipation inhibits losses and induces correlations in cold molecular gases". In: *Science* 320.5881 (2008), pp. 1329–1331. ISSN: 00368075. DOI: `10.1126/science.1155309`. arXiv: `0806.4310` (cit. on pp. 3, 62, 89).

[111] J. J. García-Ripoll, S. Dürr, N. Syassen, D. M. Bauer, M. Lettner, G. Rempe, and J. I. Cirac. "Dissipation-induced hard-core boson gas in an optical lattice". In: *New Journal of Physics* 11 (2009). ISSN: 13672630. DOI: `10.1088/1367-2630/11/1/013053` (cit. on pp. 3, 62, 89, 94, 96).

[112] S. Dürr, J. J. García-Ripoll, N. Syassen, D. M. Bauer, M. Lettner, J. I. Cirac, and G. Rempe. "Lieb-Liniger model of a dissipation-induced Tonks-Girardeau gas". In: *Physical Review A - Atomic, Molecular, and Optical Physics* 79.2 (2009), pp. 1–13. ISSN: 10502947. DOI: `10.1103/PhysRevA.79.023614`. arXiv: `arXiv:0809.3696v2` (cit. on pp. 3, 89).

[113] Takafumi Tomita, Shuta Nakajima, Yosuke Takasu, and Yoshiro Takahashi. "Dissipative Bose-Hubbard system with intrinsic two-body loss". In: *Phys. Rev. A* 99 (3 2019), p. 031601. DOI: `10.1103/PhysRevA.99.031601` (cit. on pp. 3, 90).

[114]   Bo Yan, Steven A. Moses, Bryce Gadway, Jacob P. Covey, Kaden R. A. Haz-zard, Ana Maria Rey, Deborah S. Jin, and Jun Ye. "Observation of dipolar spin-exchange interactions with lattice confined polar molecules". In: *Nature* 501 (2013), pp. 521–525. ISSN: 1476-4687. DOI: `10.1038/nature12483`. arXiv: `1305.5598` (cit. on pp. 3, 89, 94, 96).

[115]   B. Zhu et al. "Suppressing the loss of ultracold molecules via the continuous quantum Zeno effect". In: *Physical Review Letters* 112.7 (2014), pp. 1–5. ISSN: 00319007. DOI: `10.1103/PhysRevLett.112.070404`. arXiv: `1310.2221` (cit. on pp. 3, 89, 94).

[116]   Takafumi Tomita, Shuta Nakajima, Ippei Danshita, Yosuke Takasu, and Yoshiro Takahashi. "Observation of the Mott insulator to superfluid crossover of a driven-dissipative Bose-Hubbard system". In: *Science Advances* 3.12 (2017). DOI: `10.1126/sciadv.1701513`. eprint: `https://advances.sciencemag.org/content/3/12/e1701513.full.pdf` (cit. on pp. 3, 89, 95).

[117]   Samantha Lapp, Jackson Ang'ong'a, Fangzhao Alex An, and Bryce Gadway. "Engineering tunable local loss in a synthetic lattice of momentum states". In: *New Journal of Physics* 21.4 (2019), p. 045006. DOI: `10.1088/1367-2630/ab1147` (cit. on pp. 3, 89).

[118]   Masaya Nakagawa, Naoto Tsuji, Norio Kawakami, and Masahito Ueda. "Dynamical Sign Reversal of Magnetic Correlations in Dissipative Hubbard Models". In: *Phys. Rev. Lett.* 124 (14 2020), p. 147203. DOI: `10.1103/PhysRevLett.124.147203` (cit. on pp. 3, 90, 94, 99, 105, 107, 108).

[119]   Lei Pan, Xueliang Wang, Xiaoling Cui, and Shu Chen. "Interaction-induced dynamical $\mathcal{PT}$-symmetry breaking in dissipative Fermi-Hubbard models". In: *Phys. Rev. A* 102 (2 2020), p. 023306. DOI: `10.1103/PhysRevA.102.023306` (cit. on pp. 3, 90).

[120]   Zhihao Xu and Shu Chen. "Topological Bose-Mott insulators in one-dimensional non-Hermitian superlattices". In: *Phys. Rev. B* 102 (3 2020), p. 035153. DOI: `10.1103/PhysRevB.102.035153` (cit. on pp. 3, 90).

[121]   Davide Rossini, Alexis Ghermaoui, Manel Bosch Aguilera, Rémy Vatré, Raphaël Bouganne, Jérôme Beugnon, Fabrice Gerbier, and Leonardo Mazza. "Strong correlations in lossy one-dimensional quantum gases: from the quantum Zeno effect to the generalized Gibbs ensemble". In: (2020). arXiv: `2011.04318 [cond-mat.quant-gas]` (cit. on pp. 3, 90).

[122] Masaya Nakagawa, Norio Kawakami, and Masahito Ueda. "Exact Liouvillian Spectrum of a One-Dimensional Dissipative Hubbard Model". In: *Phys. Rev. Lett.* 126 (11 2021), p. 110404. DOI: `10.1103/PhysRevLett.126.110404` (cit. on pp. 3, 90).

[123] Lorenzo Rosso, Davide Rossini, Alberto Biella, and Leonardo Mazza. *One-dimensional spin-1/2 fermionic gases with two-body losses: weak dissipation and spin conservation*. 2021. arXiv: `2104.07929 [cond-mat.quant-gas]` (cit. on pp. 3, 90, 103).

[124] R.H. Dicke. "Coherence in Spontaneous Radiation Processes". In: *Physical Review* 93.1 (1954), pp. 99–110. ISSN: 0031-899X. DOI: `10.1038/nphoton.2015.54`. arXiv: `1407.7336` (cit. on pp. 3, 90, 97).

[125] Sören Dörscher, Alexander Thobe, Bastian Hundt, André Kochanke, Rodolphe Le Targat, Patrick Windpassinger, Christoph Becker, and Klaus Sengstock. "Creation of quantum-degenerate gases of ytterbium in a compact 2D-/3D-magneto-optical trap setup". In: *Review of Scientific Instruments* 84.4 (2013), p. 043109. DOI: `10.1063/1.4802682` (cit. on pp. 5, 9, 11, 12, 15).

[126] Sören Dörscher. "Creation of ytterbium quantum gases with a compact 2D-/3D-MOT setup". PhD thesis. Hamburg: Universität Hamburg, 2013 (cit. on pp. 5, 9, 11, 12, 14–16, 21).

[127] Alexander Thobe. "Ultracold Yb Gases with Control over Spin and Orbital Degrees of Freedom". PhD thesis. Hamburg: Universität Hamburg, 2014 (cit. on pp. 5, 9, 11, 12, 14, 15, 17, 18, 21, 44–47).

[128] Bastian Hundt. "Optical Potentials for the Realization of Dissipative Fermi-Hubbard Models with Ultracold Ytterbium Atoms". PhD thesis. Hamburg: Universität Hamburg, 2016 (cit. on pp. 5, 9, 11, 12, 14, 15, 17, 18, 21, 90, 91, 93, 111).

[129] André Kochanke. "Towards Quantum Simulation of the Kondo-Lattice-Model". PhD thesis. Hamburg: Universität Hamburg, 2017 (cit. on pp. 5, 6, 9, 11, 12, 14, 15, 17, 18, 21, 22, 35, 38, 91, 93, 96).

[130] Thomas Ponath. "Probing Ytterbium Quantum Gases in an Optical Lattice using the Clock Transition". PhD thesis. Hamburg: Universität Hamburg, 2018 (cit. on pp. 5, 9, 11, 12, 21, 26, 38).

[131] Thomas Rützel. "Conceptual Design and Setup of a Highly Stable Laser for Precision Measurements on Ultracold Quantum Gases". Diploma thesis. Hamburg: Universität Hamburg, 2010 (cit. on pp. 5, 21).

[132] Hans Keßler. "Setting up a blue laser system as light source for a Ytterbium 2D-MOT". Diploma thesis. Hamburg: Universität Hamburg, 2011 (cit. on pp. 5, 9, 11).

[133] Jan-Henrik Carstens. "Stabilization of a Clock Laser for High Precision Spectroscopy on Ultracold Quantum Gases". Diploma thesis. Hamburg: Universität Hamburg, 2011 (cit. on pp. 5, 21).

[134] Anna Skottke. "Aufbau spektroskopischer Komponenten zur Laserstabilisierung für ein Quantengasexperiment". Bachelor thesis. Hamburg: Universität Hamburg, 2013 (cit. on p. 5).

[135] Niels Petersen. "Aufbau und Charakterisierung eines optischen Dreiecksgitters für Ytterbium". Master thesis. Hamburg: Universität Hamburg, 2014 (cit. on pp. 5, 18).

[136] Torben Sobottke. "Design und Realisierung eines hochauflösenden Detektionssystems für Ytterbium-Quantengase". Bachelor thesis. Hamburg: Universität Hamburg, 2014 (cit. on pp. 5, 22).

[137] Karl Lukas Heinze. "Optimierung des Designs und Konstruktion eines 399nm External Cavity Diodelasers". Bachelor thesis. Hamburg: Universität Hamburg, 2016 (cit. on p. 5).

[138] Benjamin Abeln. "Design, Implementation and Characterization of a new Laser System for Mixtures of Ytterbium Quantum Gases". Master thesis. Hamburg: Universität Hamburg, 2016 (cit. on pp. 5, 9, 12, 15, 17).

[139] Anna Skottke. "Aufbau eines zustandsabhängigen Gitters für die Realisierung des 1D-Kondo-Gitter-Modells mit ultrakalten Ytterbium-Atomen". Master thesis. Hamburg: Universität Hamburg, 2016 (cit. on p. 5).

[140] Maximilian Hagenah. "Optische Resonatoren zur Frequenzstabilisierung von Lasern". Bachelor thesis. Hamburg: Universität Hamburg, 2018 (cit. on p. 5).

[141] Nejira Pintul. "Towards the Creation of Artificial Gauge Fields in Synthetic Dimensions for Fermionic Ytterbium". Bachelor thesis. Hamburg: Universität Hamburg, 2018 (cit. on pp. 5, 17).

[142] Nejira Pintul. "Ytterbium Fermi-Fermi Mixtures in Optical Lattices". Master thesis. Hamburg: Universität Hamburg, 2020 (cit. on pp. 5, 23, 84, 85).

[143] Benjamin Abeln. "In preparation". PhD thesis. Hamburg: Universität Hamburg, 2021 (cit. on pp. 5, 9, 10, 12, 15, 17, 18, 21–23, 39, 40, 59, 64, 65, 70, 71).

[144] Marcel Diem. "In preparation". PhD thesis. Hamburg: Universität Hamburg, 2021 (cit. on pp. 5, 18, 38).

[145] F.G. Kondev, M. Wang, W.J. Huang, S. Naimi, and G. Audi. "The NUBASE2020 evaluation of nuclear physics properties". In: *Chinese Physics C* 45.3 (2021), p. 030001. DOI: `10.1088/1674-1137/abddae` (cit. on p. 5).

[146] A. Kramida, Yu. Ralchenko, J. Reader, and NIST ASD Team. NIST Atomic Spectra Database (ver. 5.8), [Online]. Available: `https://physics.nist.gov/asd` [2021, April 23]. National Institute of Standards and Technology, Gaithersburg, MD. 2020 (cit. on pp. 6, 12, 17).

[147] Dipankar Das, Sachin Barthwal, Ayan Banerjee, and Vasant Natarajan. "Absolute frequency measurements in Yb with 0.08 ppb uncertainty: Isotope shifts and hyperfine structure in the $399-$nm $^1S_0 \rightarrow^1 P_1$ line". In: *Phys. Rev. A* 72 (3 2005), p. 032506. DOI: `10.1103/PhysRevA.72.032506` (cit. on p. 6).

[148] Kanhaiya Pandey, Alok K. Singh, P. V. Kiran Kumar, M. V. Suryanarayana, and Vasant Natarajan. "Isotope shifts and hyperfine structure in the 555.8-nm $^1S_0 \rightarrow {}^3P_1$ line of Yb". In: *Phys. Rev. A* 80 (2 2009), p. 022518. DOI: `10.1103/PhysRevA.80.022518` (cit. on p. 6).

[149] N. D. Lemke, A. D. Ludlow, Z. W. Barber, T. M. Fortier, S. A. Diddams, Y. Jiang, S. R. Jefferts, T. P. Heavner, T. E. Parker, and C. W. Oates. "Spin-1/2 Optical Lattice Clock". In: *Phys. Rev. Lett.* 103 (6 2009), p. 063001. DOI: `10.1103/PhysRevLett.103.063001` (cit. on p. 6).

[150] C. W. Hoyt, Z. W. Barber, C. W. Oates, T. M. Fortier, S. A. Diddams, and L. Hollberg. "Observation and Absolute Frequency Measurements of the $^1S_0-^3P_0$ Optical Clock Transition in Neutral Ytterbium". In: *Phys. Rev. Lett.* 95 (8 2005), p. 083003. DOI: `10.1103/PhysRevLett.95.083003` (cit. on p. 6).

[151] C. J. Bowers, D. Budker, E. D. Commins, D. DeMille, S. J. Freedman, A.-T. Nguyen, S.-Q. Shang, and M. Zolotorev. "Experimental investigation of excited-state lifetimes in atomic ytterbium". In: *Phys. Rev. A* 53 (5 1996), pp. 3103–3109. DOI: `10.1103/PhysRevA.53.3103` (cit. on p. 6).

[152] M.A. Cazalilla, A.F. Ho, and M. Ueda. "Ultracold gases of ytterbium: ferromagnetism and Mott states in an SU(6) Fermi system". In: *New J. Phys.* 11 (2009), p. 103033. DOI: `10.1088/1367-2630/11/10/103033` (cit. on p. 7).

[153] Martin M. Boyd, Tanya Zelevinsky, Andrew D. Ludlow, Sebastian Blatt, Thomas Zanon-Willette, Seth M. Foreman, and Jun Ye. "Nuclear spin effects in optical lattice clocks". In: *Phys. Rev. A* 76 (2 2007), p. 022510. DOI: `10.1103/PhysRevA.76.022510` (cit. on p. 7).

[154]   Cheng Chin, Rudolf Grimm, Paul Julienne, and Eite Tiesinga. "Feshbach res-
        onances in ultracold gases". In: *Rev. Mod. Phys.* 82 (2 2010), pp. 1225–1286.
        DOI: `10.1103/RevModPhys.82.1225` (cit. on p. 8).

[155]   Oscar Bettermann, Nelson Darkwah Oppong, Giulio Pasqualetti, Luis Riegger,
        Immanuel Bloch, and Simon Fölling. "Clock-line photoassociation of strongly
        bound dimers in a magic-wavelength lattice". In: (2020). arXiv: `2003.10599`
        `[cond-mat.quant-gas]` (cit. on pp. 8, 43, 48, 51, 54, 55, 58, 59, 61, 73, 79,
        81–83, 87, 95).

[156]   David J. Griffiths. *Introduction to Quantum Mechanics (2nd Edition)*. Interna-
        tional Edition. Pearson Prentice Hall, 2005. ISBN: 0-13-191175-9 (cit. on pp. 8,
        70).

[157]   G. Cappellini, L. F. Livi, L. Franchi, D. Tusi, D. Benedicto Orenes, M. In-
        guscio, J. Catani, and L. Fallani. "Coherent Manipulation of Orbital Feshbach
        Molecules of Two-Electron Atoms". In: *Phys. Rev. X* 9 (1 2019), p. 011028.
        DOI: `10.1103/PhysRevX.9.011028` (cit. on pp. 8, 59, 61, 81–83, 87, 104).

[158]   Harold J. Metcalf and Peter van der Straten. *Laser Cooling and Trapping*. New
        York: Springer, 1999. ISBN: 978-0-387-98728-6. DOI: `10.1007/978-1-4612-`
        `1470-0` (cit. on pp. 9, 12, 13, 16, 26, 30, 31, 91).

[159]   *Figure made using ComponentLibrary, with small modifications. ComponentLi-
        brary by Alexander Franzen is licensed under a Creative Commons Attribution-
        NonCommercial 3.0 Unported License.* (Cit. on p. 11).

[160]   J. Stenger, S. Inouye, D. M. Stamper-Kurn, H.-J. Miesner, A. P. Chikkatur,
        and W. Ketterle. "Laser phase and frequency stabilization using an optical res-
        onator". In: *Appl. Phys. B* 31 (1983), 97–105. DOI: `10.1007/BF00702605` (cit.
        on pp. 12, 21).

[161]   T. Sleator, T. Pfau, V. Balykin, O. Carnal, and J. Mlynek. "Experimental demon-
        stration of the optical Stern-Gerlach effect". In: *Phys. Rev. Lett.* 68 (13 1992),
        pp. 1996–1999. DOI: `10.1103/PhysRevLett.68.1996` (cit. on pp. 12, 17).

[162]   R. Grimm, M. Weidemüller, and Y. B. Ovchinnikov. "Optical dipole traps for
        neutral atoms". In: (1999). eprint: `arXiv:physics/9902072` (cond-mat.quant-
        gas) (cit. on pp. 13, 15).

[163]   L. Riegger, N. Darkwah Oppong, M. Höfer, D. R. Fernandes, I. Bloch, and
        S. Fölling. "Localized Magnetic Moments with Tunable Spin Exchange in a
        Gas of Ultracold Fermions". In: *Phys. Rev. Lett.* 120 (14 2018), p. 143601. DOI:
        `10.1103/PhysRevLett.120.143601` (cit. on pp. 18, 43, 59).

[164] Z. W. Barber, J. E. Stalnaker, N. D. Lemke, N. Poli, C. W. Oates, T. M. Fortier, S. A. Diddams, L. Hollberg, C. W. Hoyt, A. V. Taichenachev, and V. I. Yudin. "Optical Lattice Induced Light Shifts in an Yb Atomic Clock". In: *Phys. Rev. Lett.* 100 (10 2008), p. 103002. DOI: `10.1103/PhysRevLett.100.103002` (cit. on p. 18).

[165] C Becker, P Soltan-Panahi, J Kronjäger, S Dörscher, K Bongs, and K Sengstock. "Ultracold quantum gases in triangular optical lattices". In: *New Journal of Physics* 12.6 (2010), p. 065025. DOI: `10.1088/1367-2630/12/6/065025` (cit. on p. 18).

[166] Christoph Becker. "Multi component Bose-Einstein Condensates". PhD thesis. Hamburg: Universität Hamburg, 2008 (cit. on pp. 18, 112).

[167] J. Heinze, S. Götze, J. S. Krauser, B. Hundt, N. Fläschner, D.-S. Lühmann, C. Becker, and K. Sengstock. "Multiband Spectroscopy of Ultracold Fermions: Observation of Reduced Tunneling in Attractive Bose-Fermi Mixtures". In: *Phys. Rev. Lett.* 107 (13 2011), p. 135303. DOI: `10.1103/PhysRevLett.107.135303` (cit. on pp. 19, 35).

[168] Long-Sheng Ma, Peter Jungner, Jun Ye, and John L. Hall. "Delivering the same optical frequency at two places: accurate cancellation of phase noise introduced by an optical fiber or other time-varying path". In: *Opt. Lett.* 19.21 (1994), pp. 1777–1779. DOI: `10.1364/OL.19.001777` (cit. on p. 21).

[169] D. A. Steck. *Quantum and Atom Optics*. available online at http://steck.us/teaching (revision 0.13.4, 24 September 2020) (cit. on pp. 26, 31).

[170] Ch. Lisdat, J. S. R. Vellore Winfred, T. Middelmann, F. Riehle, and U. Sterr. "Collisional Losses, Decoherence, and Frequency Shifts in Optical Lattice Clocks with Bosons". In: *Phys. Rev. Lett.* 103 (9 2009), p. 090801. DOI: `10.1103/PhysRevLett.103.090801` (cit. on p. 31).

[171] Lars Hilbig. "Künstliche Eichfelder und Synthetische Dimensionen". Master thesis. Hamburg: Universität Hamburg, 2019 (cit. on p. 38).

[172] Francesco Scazza. "Probing SU(N)-symmetric orbital interactions with ytterbium Fermi gases in optical lattices". PhD thesis. München: LMU München, 2015 (cit. on p. 40).

[173] Koki Ono, Yoshiki Amano, Toshiya Higomoto, Yugo Saito, and Yoshiro Takahashi. "Observation of spin-exchange dynamics between itinerant and localized [171]Yb atoms". In: *Phys. Rev. A* 103 (4 2021), p. L041303. DOI: `10.1103/PhysRevA.103.L041303` (cit. on pp. 43, 59).

[174]   Zbigniew Idziaszek and Paul S. Julienne. "Universal Rate Constants for Re-
        active Collisions of Ultracold Molecules". In: *Phys. Rev. Lett.* 104 (11 2010),
        p. 113202. DOI: `10.1103/PhysRevLett.104.113202` (cit. on pp. 61, 62, 80,
        81, 86).

[175]   R Bouganne, M Bosch Aguilera, A Dareau, E Soave, J Beugnon, and F Gerbier.
        "Clock spectroscopy of interacting bosons in deep optical lattices". In: *New
        Journal of Physics* 19.11 (2017), p. 113006. DOI: `10.1088/1367-2630/`
        `aa8c45` (cit. on pp. 61, 81, 82, 87).

[176]   L Franchi, L F Livi, G Cappellini, G Binella, M Inguscio, J Catani, and L Fal-
        lani. "State-dependent interactions in ultracold ^{174}Yb probed by optical clock
        spectroscopy". In: *New Journal of Physics* 19.10 (2017), p. 103037. DOI: `10.`
        `1088/1367-2630/aa8fb4` (cit. on pp. 61, 81, 82, 87).

[177]   Goulven Quéméner and Paul S. Julienne. "Ultracold Molecules under Con-
        trol!" In: *Chemical Reviews* 112.9 (2012). PMID: 22921011, pp. 4949–5011.
        DOI: `10.1021/cr300092g`. eprint: `https://doi.org/10.1021/cr300092g`
        (cit. on pp. 62, 80).

[178]   S. G. Porsev, M. S. Safronova, A. Derevianko, and Charles W. Clark. "Long-
        range interaction coefficients for ytterbium dimers". In: *Phys. Rev. A* 89 (1
        2014), p. 012711. DOI: `10.1103/PhysRevA.89.012711` (cit. on pp. 80, 82,
        87).

[179]   Paweł Tecmer, Katharina Boguslawski, Mateusz Borkowski, Piotr S. Żuchowski,
        and Dariusz Kędziera. "Modeling the electronic structures of the ground and
        excited states of the ytterbium atom and the ytterbium dimer: A modern quan-
        tum chemistry perspective". In: *International Journal of Quantum Chemistry*
        119.18 (2019), e25983. DOI: `https://doi.org/10.1002/qua.25983`.
        eprint: `https://onlinelibrary.wiley.com/doi/pdf/10.1002/qua.`
        `25983` (cit. on pp. 82, 87).

[180]   A Goban, R B Hutson, G E Marti, S L Campbell, M A Perlin, P S Julienne,
        J P D'Incao, A M Rey, and J Ye. "Emergence of multi-body interactions in a
        fermionic lattice clock". In: *Nature* 563 (2018), pp. 369–373. DOI: `10.1038/`
        `s41586-018-0661-6` (cit. on pp. 83, 85–87).

[181]   R. Jördens, N. Strohmaier, K. Günter, H. Moritz, and T. Esslinger. "A Mott in-
        sulator of fermionic atoms in an optical lattice". In: *Nature* 455 (2008), 204–207.
        DOI: `10.1038/nature07244` (cit. on p. 84).

[182] Joschka Wolf, Markus Deiß, Artjom Krükow, Eberhard Tiemann, Brandon P. Ruzic, Yujun Wang, José P. D'Incao, Paul S. Julienne, and Johannes Hecker Denschlag. "State-to-state chemistry for three-body recombination in an ultracold rubidium gas". In: *Science* 358.6365 (2017), pp. 921–924. ISSN: 0036-8075. DOI: `10.1126/science.aan8721`. eprint: `https://science.sciencemag.org/content/358/6365/921.full.pdf` (cit. on p. 86).

[183] Ali Sanayei and Ludwig Mathey. "Three-body bound states of an atom in a Fermi mixture". In: (2020). arXiv: `2007.13511v2 [cond-mat.quant-gas]` (cit. on p. 87).

[184] E. M. Purcell and R. V. Pound. "A Nuclear Spin System at Negative Temperature". In: *Phys. Rev.* 81 (2 1951), pp. 279–280. DOI: `10.1103/PhysRev.81.279` (cit. on pp. 90, 99).

[185] Norman F. Ramsey. "Thermodynamics and Statistical Mechanics at Negative Absolute Temperatures". In: *Phys. Rev.* 103 (1 1956), pp. 20–28. DOI: `10.1103/PhysRev.103.20` (cit. on pp. 90, 99).

[186] M. Greiner, O. Mandel, T. Esslinger, T. W. Hänsch, and I. Bloch. "Quantum phase transition from a superfluid to a Mott insulator in a gas of ultracold atoms". In: *Nature* 415 (2002), pp. 39–44. DOI: `10.1038/415039a` (cit. on p. 90).

[187] Nikolay V Vitanov, Thomas Halfmann, Bruce W Shore, and Klaas Bergmann. "Laser-Induced Population Transfer by Adiabatic Passage Techniques". In: *Annu. Rev. Phys. Chem* 52 (2001), pp. 763–809. ISSN: 0066-426X. DOI: `10.1146/annurev.physchem.52.1.763` (cit. on pp. 91, 93).

[188] G. Lindblad. "On the generators of quantum dynamical semigroups". In: *Communications in Mathematical Physics* 48.2 (1976), pp. 119–130. ISSN: 00103616. DOI: `10.1007/BF01608499`. arXiv: `arXiv:1402.7287v1` (cit. on p. 94).

[189] Vittorio Gorini, Andrzej Kossakowski, and E. C. G. Sudarshan. "Completely positive dynamical semigroups of N-level systems". In: *Journal of Mathematical Physics* 17.5 (1976), pp. 821–825. DOI: `10.1063/1.522979`. eprint: `https://aip.scitation.org/doi/pdf/10.1063/1.522979` (cit. on p. 94).

[190] Bernd Lücke, Jan Peise, Giuseppe Vitagliano, Jan Arlt, Luis Santos, Géza Tóth, and Carsten Klempt. "Detecting multiparticle entanglement of Dicke states". In: *Physical Review Letters* 112.15 (2014), pp. 1–5. ISSN: 10797114. DOI: `10.1103/PhysRevLett.112.155304`. arXiv: `1403.4542` (cit. on pp. 97, 108).

[191]   Iagoba Apellaniz, Bernd Lücke, Jan Peise, Carsten Klempt, and Géza Tóth. "Detecting metrologically useful entanglement in the vicinity of Dicke states". In: *New Journal of Physics* 17.8 (2015). ISSN: 13672630. DOI: 10.1088/1367-2630/17/8/083027. arXiv: 1412.3426 (cit. on pp. 97, 108).

[192]   Elmar Haller, Mattias Gustavsson, Manfred J. Mark, Johann G. Danzl, Russell Hart, Guido Pupillo, and Hanns-Christoph Nägerl. "Realization of an Excited, Strongly Correlated Quantum Gas Phase". In: *Science* 325.5945 (2009), pp. 1224–1227. ISSN: 0036-8075. DOI: 10.1126/science.1175850. eprint: https://science.sciencemag.org/content/325/5945/1224.full.pdf (cit. on p. 104).

[193]   P. B. Blakie, A. Bezett, and P. Buonsante. "Degenerate Fermi gas in a combined harmonic-lattice potential". In: *Phys. Rev. A* 75 (6 2007), p. 063609. DOI: 10.1103/PhysRevA.75.063609 (cit. on p. 104).

[194]   Masahito Ueda. *Private communication*. 2020 (cit. on p. 105).

[195]   Ryuta Yamamoto, Jun Kobayashi, Takuma Kuno, Kohei Kato, and Yoshiro Takahashi. "An ytterbium quantum gas microscope with narrow-line laser cooling". In: *New Journal of Physics* 18.2 (2016), p. 023016. DOI: 10.1088/1367-2630/18/2/023016 (cit. on p. 108).

[196]   Ryuta Yamamoto, Jun Kobayashi, Kohei Kato, Takuma Kuno, Yuto Sakura, and Yoshiro Takahashi. "Site-resolved imaging of single atoms with a Faraday quantum gas microscope". In: *Phys. Rev. A* 96 (3 2017), p. 033610. DOI: 10.1103/PhysRevA.96.033610 (cit. on p. 108).

[197]   J. Struck, C. Ölschläger, R. Le Targat, P. Soltan-Panahi, A. Eckardt, M. Lewenstein, P. Windpassinger, and K. Sengstock. "Quantum Simulation of Frustrated Classical Magnetism in Triangular Optical Lattices". In: *Science* 333.6045 (2011), pp. 996–999. ISSN: 0036-8075. DOI: 10.1126/science.1207239. eprint: https://science.sciencemag.org/content/333/6045/996.full.pdf (cit. on p. 108).

[198]   Valentin Kaspar, Christoph Becker, and Koen Sponselee. *Private communication*. 2019 (cit. on p. 108).

[199]   Simon Hooker and Colin Webb. *Laser Physics*. Oxford University Press, 2010. ISBN: 978-0-19-850692-8 (cit. on p. 112).

Acknowledgements

Running a quantum-gas laboratory can hardly be done alone, let alone one with twelve laser systems. Therefore, this work would have been impossible without the continuous collaboration and help of others. Though it is hard to thank everyone individually without writing a few dozen pages, I will here thank the people who have helped the most.

First of all, I would like to thank Klaus Sengstock, without whom none of this would have been possible. I am very grateful for having gotten the opportunity to work in your research group and I am glad that I ended up in the ytterbium experiment. One of the aspects I appreciated the most were the many opportunities for exchange and discussion within the large research group, the SFB, the Excellence Cluster and with the many invited scientists. As the speaker of SFB925 and CUI/AiM, this is in large part thanks to you. Furthermore, I would like to thank you for allowing me to organise YAO2019 with the rest of the committee and for your valuable advice in the preparation.

I would like to greatly thank Christoph Becker for his supervision over the years. Right from the start you have made me feel part of the team, which helped making the move from the Netherlands smooth. I appreciate that you took so much time to talk about physics and experimental details, and I always enjoyed interpreting measurements together. In this way, I learned a lot directly, but also indirectly through your motivation. Furthermore, thank you very much for the feedback during the writing of this work. And last but not least, I will also fondly look back on talking about non-physics topics, such as German culture, 90's techno and the combination of the two.

Most of the daily work in the lab was done together with Benjamin Abeln and Marcel Diem. I really enjoyed working together with you both. Benni, when I started I was very happy you joined soon after, because with your experience in the Yb lab, you helped me greatly in understanding the functionalities of the complex lab. Working together was productive and enjoyable, especially in the last few months in the lab. I

also enjoyed seeing you play in your band and organising YAO2019 together. Marcel, thank you for the pleasant time in the lab, and for the interesting discussions. I enjoyed working together in the lab, and discussing about physics. I also liked playing billiard in Eimsbüttel together, and I am looking forward to the next one.

Over the years, the team changed a lot, but Bodhaditya Santra was the only other person in the lab when I arrived. Bodha, I would like to you thank you for your patience and friendliness, and I enjoyed working together. Thanks to André Kochanke and Thomas Ponath for introducing me to the lab just before leaving, and thanks to the previous generations of people who built up the lab before I arrived. Furthermore, thanks to our students Max Hagenah, Lars Hilbig, Donika Imeri, Fabian Gropp and Timo Eikelmann, it was a pleasure working together. Thanks to Nejira Pintul, I enjoyed working together on repumper schemes and doublon calculations in specific, and thanks for helping me with the German version of the abstract. Thanks to Tobias Petersen: though you just joined our team, I am looking forward to working together in the future.

My gratitude also goes to the whole Sengstock research group for the interesting and helpful discussions, for borrowing lab equipment and help in the lab. In specific, I would like to thank Christof Weitenberg and Juliette Simonet for the many useful discussions, Ortwin Hellmig for invaluable help in the lab on various topics (though often fibre-related, obviously), and Philipp Wessels-Staarmann for the discussions and help with Matlab in the beginning. Thanks also goes to all our student assistants for the various useful projects they did. I would like to thank Ralf Lühr, Reinhard Mielck and Dieter Barlösius for their technical support, and Janina Neubert, Ellen Gloy, Nadja Wardenburg and Loreen Tornier for their help in the administrative aspects of the large research group.

Of the research group, I would especially like to thank Tobias Klafka, Alexander Ilin, Tobias Kroker and Benni (again) for the joy of organising YAO2019 together. Though a lot of the organisation was fairly involved, I am very happy with how the conference went and it was a great pleasure to do this with you all. Organising the conference would not have been possible without the help of Irmgard Flick and Sylke Strien, for which I am very grateful.

I would like to thank our theory colleagues in the Centre for Optical Quantum Technologies, especially Ludwig Mathey and Lukas Freystatzky, for the interesting discussions and for working together on the dissipation paper. Thanks to Peter Schmelcher, Simos Mistakidis and George Bougas for stimulating discussions on Fermi-Fermi mixtures and molecular physics. Furthermore, I would like to thank the other research groups of the Institute for Laser Physics and the Centre for Optical Quantum Technologies, and from the SFB925 for the many interesting discussions. Of the countless people I met, I would like to thank Marlon Nuske, Ali Sanayei and Ilias Seifie in specific,

but I also appreciated the many other stimulating conversations, which enlivened the workplace. I would also like to thank the referees Ludwig Mathey, Peter Schmelcher, Markus Drescher, Henning Moritz and Klaus Sengstock for the (upcoming) defence. Additionally, thanks to Henning Moritz for being my second supervisor and for the useful discussions. Finally, I would like to thank the SFB925 for the financing of my PhD.

I would also like to thank the many people I met at conferences over the years for the interesting discussions. In specific, I would like to thank Valentin Kaspar for the interesting discussions on the dissipative Fermi-Hubbard model in a 2D triangular lattice, and thanks to the rest of the group at ICFO for their hospitality and the interesting discussions. I would like to thank the visiting scientists, in specific Masahito Ueda for the illuminating discussion on the 1D dissipative Fermi-Hubbard model. Furthermore, thanks to Peter van der Straten for welcoming me back to Utrecht occasionally, and thanks for your suggestions between my Master's and PhD.

Though of course your help was less direct, though no less profound, I would like to thank the people at the 'Volkssterrenwacht Philippus Lansbergen' (People's Observatory Philuppus Lansbergen) in my hometown Middelburg, the Netherlands. You have motivated me to learn about astronomy and observation of the sky, back when I was about ten to fourteen years old, for which I am very grateful. Especially the contagious energy of Rijk-Jan Koppejan and motivation of Tjerk Westerterp were instrumental in inspiring my scientific curiosity during this formative period of my life.

Finally, I would also like to thank my friends in Hamburg, the Netherlands and elsewhere for so many good experiences and conversations. I would like to thank my parents Ina & Peter for their continued support and for giving me every opportunity to develop myself, even if that meant moving abroad. It might sound like a cliché, but without you none of this would have been possible, and I am very grateful for it. Thanks to my sisters Marjolijn & Hanne for your support and showing your interest in my activities. Thanks to you four for making it possible to see each other regularly (if there is no pandemic on-going), despite the large physical distance. I am glad the emotional distance always remained small. And last but not least, thanks to Natalia for your invaluable support. Thank you for your encouragement, the countless interesting and enlightening conversations, and for showing me experiences that were new to me.

Eidesstattliche Erklärung

Hiermit versichere ich an Eides statt, die vorliegende Dissertationsschrift selbst verfasst und keine anderen als die angegebenen Hilfsmittel und Quellen benutzt zu haben. Die eingereichte schriftliche Fassung entspricht der auf dem elektronischen Speichermedium. Die Dissertation wurde in der vorgelegten oder einer ähnlichen Form nicht schon einmal in einem früheren Promotionsverfahren angenommen oder als ungenügend beurteilt. Es sind keine Vorveröffentlichungen aus dieser Dissertation hervorgegangen.

Unterschrift: _____

Datum: _____